Institute of Geophysics
Polish Academy of Sciences

PUBLICATIONS
OF THE INSTITUTE OF GEOPHYSICS
POLISH ACADEMY OF SCIENCES

Geophysical Data Bases, Processing and Instrumentation

444 (D-78)

MONOGRAPHIC VOLUME

Sensitivity of the GEM Model to Different Descriptions of City Surface Parameters over Warsaw

Anahita SATTARI

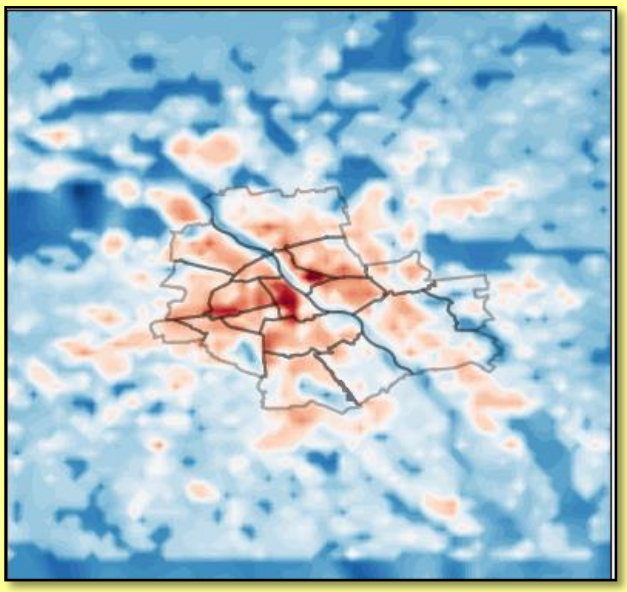

Warsaw 2023 (Issue 1)

INSTITUTE OF GEOPHYSICS
POLISH ACADEMY OF SCIENCES

PUBLICATIONS
OF THE INSTITUTE OF GEOPHYSICS
POLISH ACADEMY OF SCIENCES

Geophysical Data Bases, Processing and Instrumentation

444 (D-78)

MONOGRAPHIC VOLUME

Sensitivity of the GEM Model to Different Descriptions of City Surface Parameters over Warsaw

Anahita SATTARI

Warsaw 2023

ISBN 978-83-66254-16-9 eISSN-2299-8020
DOI: 10.25171/InstGeoph_PAS_Publs-2023-001

Figure on the front cover by Anahita Sattari

Editorial Office
Instytut Geofizyki Polskiej Akademii Nauk
ul. Księcia Janusza 64, 01-452 Warszawa

To my twin sister Niyousha

CONTENTS

Editorial note

The present publication is a revised version of the Author's PhD thesis defended at the Institute of Geophysics, Polish Academy of Sciences, under supervision of Prof. Jacek W. Kamiński.

Acknowledgments

My first and sincere appreciation goes to my supervisor, Prof Jacek W. Kamiński, for his incredible supervision, guidance, and encouragement. I am grateful for his trust in me and his constructive feedback and kind support during my PhD.

I greatly appreciate Dr. Eng. Joanna Strużewska for her great knowledge, excellent guidance, and valuable comments. Also, I am grateful to Prof. Lech Łobocki for believing in me in the first place and making this journey possible for me.

Many thanks are also for Grzegorz Jeleniewicz, Marcin Kawka, Magdalena Kossakowska, and Lech Gawuc for their kindness and constant support. Starting this thesis would not have been possible without their help.

I am grateful to my best friend and partner, Wojciech Gajek, for constantly listening to me rant and talk things out and holding me up in every moment of my despair.

Finally, I would like to thank my precious sister, mother, and brother for always being there for me and telling me that I could do it even when I did not feel that way. I am also grateful to my father for his loving support.

List of symbols

H	Height of the building	[m]
W	Width of the building	[m]
Q^*	Net radiation	[Wm^{-2}]
Q_H	Sensible heat flux	[Wm^{-2}]
Q_E	Latent heat flux	[Wm^{-2}]
Q_F	Anthropogenic heat flux	[Wm^{-2}]
ΔQ_s	Net heat storage	[Wm^{-2}]
ΔQ_A	Net energy	[Wm^{-2}]
T	Temperature	[°C]
TKE	Turbulent kinetic energy	[m^2s^{-2}]

List of abbreviations

ABL	Atmospheric Boundary Layer
BEM	Building Environment Model
CLC	CORINE Land Cover
CMC	Canadian Meteorological Centre
GEM	Global Environmental Multiscale
HIRLAM	HIgh Resolution Limited Area Model
IBL	Internal Boundary Layer
ISL	Inertial Sublayer
LAM	Limited Area Model
LLJ	Low Level Jet
ML	Mixed Layer
ML-UCM	Multi-layer Urban Canopy Model
NBL	Nocturnal Boundary Layer
RSL	Roughness Sublayer
SBL	Surface Boundary Layer
SEB	Surface Energy Balance
SL	Surface Layer
SL-UCM	Single-layer Urban Canopy Model
SVF	Sky View Factor
TEB	Town Energy Balance
UBL	Urban Boundary Layer
UCL	Urban Canopy Layer
UCM	Urban Canopy Model
UHI	Urban Heat Island
USEB	Urban Surface Energy Balance
WRF	Weather Research and Forecasting

Abstract

Over half of the world's population lives in urban areas, even though urban agglomerations cover only 0.05% of the Earth's surface. Urbanisation significantly modifies the surface level's moisture, radiation balance, thermal stability, and aerodynamic properties. The physical processes in the urban surface layer directly influence the atmosphere above and, specifically, the atmospheric boundary layer. Thus, understanding and modelling these processes are necessary for studying the urban meteorology.

The primary objective of the presented research was to assess the impact of the urban land cover on the development of the atmospheric boundary layer over Warsaw. To carry out the objective, a high-resolution version of the Global Multiscale Environmental model was used to examine its ability to reproduce the diurnal cycle of the meteorological parameters, including the thermal and turbulent structure of the atmosphere. The Town Energy Balance (TEB) parameterisation was used to represent urban effects on modelled meteorological parameters at the final nesting level with a horizontal resolution of 1 km over Warsaw. Mid-high buildings, sparse buildings, industrial areas, roads and parking spaces, and a mix of built and nature are the urban cover categories used in the TEB parameterisation. Four one-day cases representing different meteorological conditions and seasons were selected for modelling.

The model was run with and without the TEB parameterisation in the first step. The boundary layer profiles for temperature, specific humidity, potential temperature, and turbulent kinetic energy to the height of 3000 m and temperature cross-sections over Warsaw were studied for two "NO-TEB" and "TEB" scenarios.

In the second step, sensitivity analysis was performed by comparing three scenarios with different descriptions of land uses and land covers for urban areas:

1. City scenario using the TEB classification;
2. High building only scenario where the city is covered with impervious high buildings land cover;
3. Vegetation only for which city is replaced by the surrounding natural covers.

The differences in temperature, specific humidity, and turbulent kinetic energy were studied for these scenarios. Sensitivity analysis showed that the differences are significant for the winter case between the high building and vegetation scenarios and are smaller for the summer case. However, in all three scenarios, the temperature and turbulent kinetic energy are the lowest for the vegetation scenario and the highest for the high buildings scenario.

In the last step, temperature error measures were calculated for six stations in Warsaw for selected cases. The comparison of observed and modelled temperature shows that the temperature predicted with the TEB parameterisation was more accurate in terms of statistical error measures on January 29, April 24. However, on June 6 and July 23, the difference between the two scenarios was not high.

WRAŻLIWOŚĆ MODELU GEM NA RÓŻNE OPISY PARAMETRÓW POWIERZCHNI MIASTA NAD WARSZAWĄ

Streszczenie

Urbanizacja znacząco modyfikuje właściwości powierzchni terenu, wpływając na cykl dobowy i zmienność pionową elementów meteorologicznych w granicznej warstwie atmosfery. Ze względu na liczbę mieszkanców miast obejmującą ponad połowę ludności świata, zrozumienie i modelowanie tych procesów jest niezbędne do wsparcia zarządzania funkcjonowania miast i planowania przestrzennego.

Celem pracy jest ocena wpływu pokrycia terenu na kształtowanie się warstwy granicznej atmosfery nad Warszawą. W pracy wykorzystano model meteorologiczny – Global Environmental Multiscale model zagnieżdżony nad Warszawą z rozdzielczością poziomą 1 km, w połączeniu z parametryzacją Town Energy Balance. Jako okres symulacji wybrano cztery jednodniowe okresy reprezentujące różne warunki meteorologiczne i pory roku. W pierwszym etapie analizowano profile temperatury, wilgotności właściwej, temperatury potencjalnej i energii kinetycznej turbulencji do wysokości 3000 m oraz przekroje temperatury nad Warszawą dla dwóch konfiguracji modelu, z parametryzacją TEB i bez parametryzacji miasta.

W drugim etapie przeprowadzono analizę wrażliwości modelu, porównując trzy scenariusze z różnymi opisami użytkowania i pokrycia terenu dla obszarów miejskich:

1. Warunki rzeczywiste (jak w etapie pierwszym);
2. Cała powierzchnia zabudowana miasta opisana jako budynki wysokie;
3. Cała powierzchnia miasta opisana jako tereny naturalne.

Analiza wrażliwości wykazała, że różnice w temperaturze, wilgotności właściwej i energii kinetycznej turbulencji są bardziej znaczące dla przypadku zimowego, niż dla przypadku letniego. We wszystkich trzech scenariuszach temperatura i energia kinetyczna turbulencji są najniższe w scenariuszu z roślinnością i najwyższe w scenariuszu z wysokimi budynkami.

W ostatnim kroku obliczono miary błędu temperatury dla sześciu stacji w Warszawie dla wybranych przypadków. Z porównania temperatury obserwowanej i modelowanej wynika, że temperatura prognozowana z parametryzacją TEB pozwoliła uzyskać niższe miary błędu statystycznego dla scenariuszy zimowych i wiosennych. Natomiast w okresie letnim różnica między tymi dwoma scenariuszami nie była duża.

1. INTRODUCTION

The primary objective of the presented research was to assess the impact of the urban land cover on the development of the atmospheric boundary layer over Warsaw. The Global Environmental Multiscale model (GEM) (Côté et al. 1998) coupled with the Town Energy Budget (TEB) (Masson 2000) was used to carry out high-resolution short-term meteorological forecasts.

The sensitivity of the boundary layer development to changes of radiative properties of the urban surface was studied by comparing the modelling results without and with the TEB parameterisation. Also, the ability of the GEM model to reproduce the diurnal cycle of meteorological parameters over Warsaw was examined with three different land use/land covers datasets. The changes in radiative properties of urban surfaces are the results of urbanisation.

1.1 Urbanisation

Urbanisation is a process that involves a complex set of socio-economic, cultural, and technological drivers. The result of urbanisation is an increase in the proportion of the population that lives in towns and cities.

Today, 55% of the world's population resides in urban areas. In 1950, 30% of the world's population was urban, and by 2050, 68% of the world's population is projected to be urban. The UN (2018) report estimated that the urban population increased from 751 million in 1950 to 4.2 billion in 2018.

Urbanisation in Poland after the Second World War had a very dynamic period. Poland was transformed from rural to urban in the last 50 years (Szymańska and Matczak 2002). About 60% of the Polish population lives in the cities (Majewska et al. 2020).

Urbanisation causes drastic changes to the natural environment. Urban areas reveal the most evident signs of inadvertent climate modification, including transforming the radiative, solar, moisture and aerodynamic characteristics and modifying the natural solar and hydrological balances (Oke 1988).

According to the Fourth Assessment Report of the Intergovernmental Panel on Climate Change (IPCC), the changes in temperature, precipitation and extreme events in urban areas can have a rigorous negative influence on human health like an increase in illnesses and deaths (Confalonieri et al. 2007).

Human activities cause an increase in temperature and other meteorological changes in the urban systems. Urban agglomerations are the main sources of carbon dioxide emissions from industrial, transportation, and domestic consumption of fossil fuels, especially in high-income countries (Grimmond 2007).

The higher temperature in the urban areas can be exacerbated by heatwave events, which causes morbidity and mortality. The health effects of air pollution are another major concern in the cities. Different diseases can occur depending on different pollutants, such as respiratory and cardiovascular illnesses and allergies. Using a large amount of energy for domestic and industrial needs, particularly in low and middle-income countries deteriorates air quality to a great extent (Harlan and Ruddell 2011). Urban climatology relates to studying the climate effect of urban areas and applying the knowledge acquired for better planning and design of cities.

The environment is modified substantially by the urban areas in almost every aspect. The modifications are caused by alterations of surface cover, geometry, and texture and also by anthropogenic heat and water vapour emissions (Mills 2014).

Urban energy balance and climate models are valuable tools for studying the interaction between the urban environment and the atmosphere (Salim et al. 2022). Numerical models have a broad range of applications for studying urban boundary layer, air pollution, and heat and wind comfort levels (Erell 2008).

Applying numerical models at city scales is possible because of advances in computer processing speed, new algorithms, micrometeorological processes parameterisation, and remotely sensed urban data (Masson 2000).

1.2 The study area – Warsaw

Warsaw, the capital city of Poland and Mazovia Region, is located on the Vistula River in east-central Poland. It currently covers an area of 517 km^2 and has a population of 1.7 million. The "World urbanisation prospects" (UN 2018) estimated a 0.49% annual population growth. Warsaw has 32.9% of the population of the entire Mazowieckie Voivodship. These estimates represent the Urban Agglomeration of Warsaw, which typically includes the population of Warsaw proper and adjacent suburban areas. The population density is approximately 3.372 per square kilometre[1].

The surface-atmosphere heat balance is significantly modified by underground ruins that change the texture and heat capacity of the city surface in Warsaw. Bricks and concrete from unexcavated foundations and basements are under the streets and courtyards.

After World War II, a centrally planned heating system was introduced to heat apartment buildings. It is the most extensive district heating system in Europe. The central heating system is much more energy-efficient than thousands of individual boilers. However, it can directly impact the anthropogenic heat flux causing warmer street surfaces in the winter.

1.3 An outline of chapters

The thesis is comprised of five chapters following the Introduction:

- Chapter 2: Literature review and background;
- Chapter 3: Data and methods;
- Chapter 4: Results and discussion;
- Chapter 5: Conclusions and future work.

Chapter 2 provides a theoretical background and literature review of previous studies on urban canopy models, emphasising the town energy balance model. Tools and methods used in the study are described in Chapter 3.

Results obtained from the modelling are presented in Chapter 4. Conclusions and future work plans are presented in Chapter 5.

2. LITERATURE REVIEW AND BACKGROUND

Climate is generally described from standard measurements of meteorological parameters such as surface pressure, temperature, humidity, and wind velocity. However, the conditions change rapidly in the air layer above the ground, where plants, animals, and humans live. The standard measurements cannot specify the climate of these environments, and therefore there is a need for special observations, which is the domain of microclimatology. Microclimatology studies the climate near the ground, and it is usually defined vertically in terms of canopy height (Barry and Blanken 2016). The urban climate is an example of unintended climate modification initiated by human activities. The urbanisation process causes radical changes in a region's surface and atmospheric properties (Oke 1988). It was stated for the first time by Luke Howard, FRS (Fellow of the Royal Society), in "The Climate of London" in 1833 that the city's structure and composition affect local climate by impacting wind, humidity, and temperature distribution which are different between the urban environment and the rural areas (Georgiadis 2017). Today, many studies address urban climates and how they affect the well-being of the resident

[1]https://worldpopulationreview.com; World population review, 2021, last access on 30/09/2020

population. However, how the urbanisation and climate change will interact in the future is uncertain (Georgiadis 2017).

This chapter explores the theory of urban atmosphere and reviews studies done on urban climate.

2.1 Urban surface

Cities consist of a high fraction of impervious surfaces, which modify both surface energy and water balances, affecting the atmospheric boundary layer (ABL) and the weather processes (Oke and Cleugh 1987).

An urban system has a nearly unlimited number of climatically active surfaces. Each of these surfaces has different radiative, thermal, moisture, and aerodynamic properties (Oke et al. 2017). An urban surface consists of urban canyons closed off by buildings on both sides. Aspect ratio (H/W), the canyon's axis orientation, and the sky view factor (SVF) are three main descriptors of the urban canyons which have a significant influence on the microclimate (Erell et al. 2012).

2.1.1 Urban canyon

The airflow and radiation exchange in the urban canopy is affected by the dimensions and spatial arrangement of urban structures (Oke et al. 2017). Building walls and the elements lying between buildings define the urban canyon (UC) (Arnfield 2003). The aspect ratio is the building's height (H) to the street's width (W) ratio, which is an important parameter that controls the impact of urban geometry on external temperature increase and building energy demand (Jihad and Tahiri 2016).

2.1.2 Sky View Factor

The Sky View Factor (SVF) is an important parameter describing urban geometry and building density (Oke and Cleugh 1987). Also, it plays an important role in forming urban climatology and its spatial variations (Oke 1973). It is defined as the fraction of the radiative flux leaving the surface at the point that reaches the atmosphere above the urban canopy, i.e., the "sky" (Johnson and Watson 1984). It is a dimensionless parameter between zero and one (Wei et al. 2016). A decreased SVF causes an increase in the net heat storage within buildings and increases urban heat island (UHI) (Dirksen et al. 2019).

2.2 Local climate zones

The first climate-based classification of the city was done by Chandler (Oke 2009), the first heat island researcher. He divided London into four local regions based on their climate, physiography, and built form. Later, Oke (2004) introduced a generic city zones classification using the schemes from Auer's urban-rural classification proposed for the city of St. Louis, Missouri (Auer 1978), and Ellefsen's "urban terrain zones" (Ellefsen 1991) for ten US cities to develop a better deployment of meteorological instruments in urban areas. Based on the Oke (2004) scheme, the city was divided into seven homogeneous regions called urban climate zones (UCZ). Chandler, Auer, and Ellefsen's classifications have limitations, including: i) using a full set of climate properties for defining the classes; ii) having more limited use in more diverse economic settings since they are all inclined to the form and function of modern, developed cities; and iii) their class names and definitions change broadly with a place. Thereby, they cannot provide systems with the means of comparison (Stewart and Oke 2012).

Stewart and Oke (2012) defined local climate zones, LCZs, as regions of uniform surface cover, structure, material, and human activity that span hundreds of meters to several kilometres

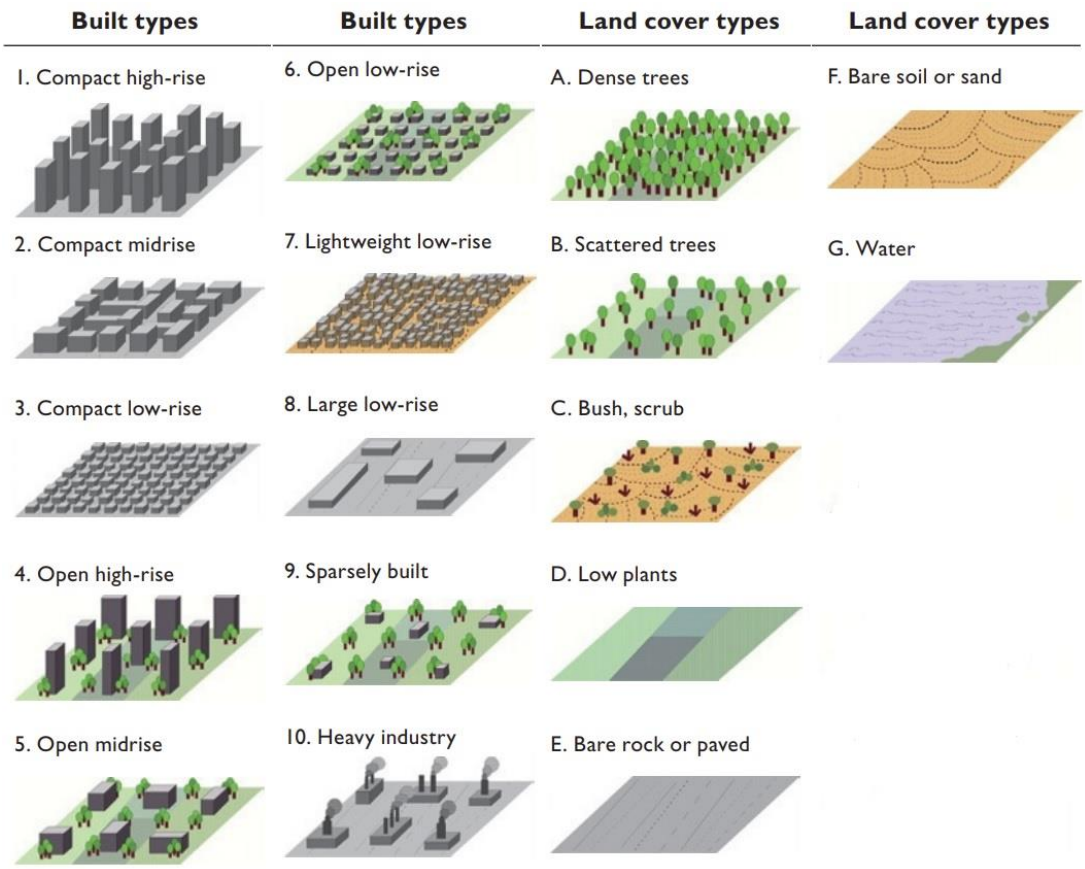

Fig. 1. Local climate zones (Stewart and Oke 2012).

in a horizontal scale. They developed an LCZ system to indicate the insufficiency of urban-rural description in urban heat island studies. This system consists of 17 zones at the local scale; 15 LCZs are defined by surface structure, and 2 by the construction materials and anthropogenic heat emissions. Figure 1 represents the local climate zones presented by Stewart and Oke (2012), where 1-9 zones correspond to Oke (2004) urban climate zones.

2.3 Atmospheric boundary layer

The atmospheric boundary layer is part of the troposphere that is directly influenced by the presence of the Earth's surface and responds to surface forcing with a timescale of about an hour or less (Stull 1988). The surface strongly impacts the wind, temperatures, and humidity within this layer (Hartmann 2015). A typical depth of the boundary layer is about 1 km, but it varies between 20 m and several kilometres (Hartmann 2015). Turbulence generated by frictional drag as the air moves across the rough surface defines the boundary layer (Oke 2002). The high frequency of turbulence near the ground makes the boundary layer distinct from the rest of the atmosphere (Stull 1988).

The structure of the boundary layer changes broadly, depending on the meteorological conditions and as a result of the surface heating or cooling (Hartmann 2015). As the surface is heated during the daytime, the upward transfer of heat to the cooler atmosphere generates strong thermal mixing (convection) and extends the boundary layer's depth to about 1 to 2 km. During the night, due to rapid surface cooling, there is a downward transfer of heat, which suppresses the mixing, and boundary depth decreases to less than 100 m (Oke 2002).

Three major components of the boundary layer structure are the mixed layer (convective BL), the residual layer, and the stable boundary layer (Stull 1988). The daytime convective

layer is the mixed layer (Oke 2002). The residual layer forms half an hour before the sunset when the turbulence decays in the formerly well-mixed layer. During the night, the bottom part of the residual layer is transformed to the stable boundary layer by its contact with the ground (Stull 1988).

2.3.1 Urban boundary layer

Urbanisation has changed the physical and chemical properties at the surface-atmosphere interface by replacing natural surfaces with artificial urban elements. The urban climate was created as a distinctive local climatic type due to changes in the meteorological properties of the atmosphere above the urban surfaces (Chandler 1976).

The urban boundary layer (UBL) is the part of the atmosphere in which people live and is one of the most complex and least-understood microclimates (Barlow 2014). An internal boundary layer starting at the upwind rural-urban border extends upward until it fills the whole atmospheric BL and creates the urban BL (Oke et al. 2017). The urban boundary layer is more complex than the rural and idealised one. It is non-homogeneous and non-stationary (Taha and Bornstein 1999).

2.3.1.1 The difference between the urban and rural boundary layers

The mixed layer over the urban areas can be deeper than over the rural areas due to the higher low-level convergence resulting in more cloud condensation nuclei. Higher frequency of thunderstorms and enhanced precipitation immediately downwind the city (Changnon 1981). Moreover, the presence of large buildings increases surface drag and turbulence and decreases the mean wind speed (Oke 1982).

A mixed layer in the urban areas can continue throughout the night because of the large heat capacity of buildings and streets and the heat released from transportation. The early evening shallow surface BLs in the rural areas are not observed in the city.

Later, during the night, while there is a deeper rural stable layer than the height of buildings, a shallow layer of air in the urban area can remain well mixed, but it is capped by the stable layer (Godowitch et al. 1985). The depth of the nocturnal UBL is much less than in the daytime, depending on the strength of the heat island and roughness effects (Oke et al. 2017). Sensible heat flux at night drives a nocturnal mixed layer consisting of a shallow convective or near-neutral turbulence layer (Barlow 2014). Furthermore, the highest temperature difference be-

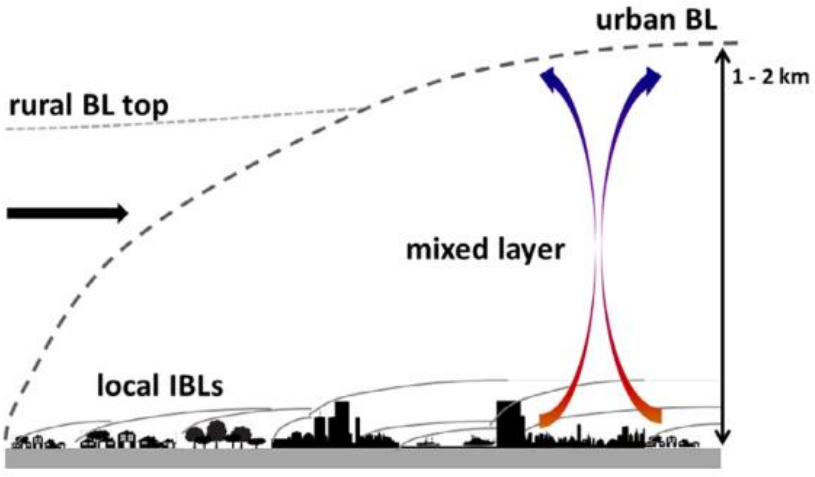

Fig. 2. Schematic diagram of the daytime convective urban boundary layer with wind flowing left to right. Dashed lines indicate rural and urban boundary layers, solid lines indicate local internal boundary layers (Barlow 2014).

tween urban and rural areas are usually observed at night. The heat from the city is enough to maintain a shallow convective mixed layer at night, even though a stable BL has developed over the neighbouring rural area (Stull 1988).

The surface layer, which occupies almost 10% of the BL, consists of the roughness sublayer (RSL) and the inertial sublayer (ISL).

An urban roughness sublayer (RSL) is defined as a depth of 2 to 5 times the mean building height. Atmospheric flow is highly spatially dependent within this layer, and the mean flow can be dominated by turbulence. Turbulence characteristics of the flow within RSL are different from the flow in the inertial sub-layer (ISL) above. Within ISL, the turbulence is homogeneous, and fluxes change slightly with height (Barlow 2014). Some of the UBL characteristics are shown schematically in Fig. 2.

As shown in Fig. 2, the internal boundary layer (IBL) forms at the interface between the smoother rural and rougher urban surfaces (Barlow 2014).

2.3.1.2 The urban canopy layer

The portion of the boundary layer between the rooftops and the ground is known as the urban canopy layer (Oke and Cleugh 1987). Its characteristics are dominated by the energy and mass exchange between individual surface facets and the canyon (Oke 1976). The urban canopy layer climate results from complex exchanges between surfaces and UBL and UCL (Mills 1997). The top of UCL is defined as the height of the urban elements – buildings or trees. Distinctly different processes and phenomena occur near the roof-level compared with those within the canopy (Oke et al. 2017). The volume of air within UCL consists of exterior and interior parts (Mills 1997). The exterior is the air in pedestrian and managed spaces, and the interior is the living space within buildings, often controlled by space heating or cooling systems (Oke et al. 2017).

2.4 Surface energy balance

Knowledge of the surface energy balance is fundamental to understanding the boundary layer meteorology and the climatology of any site. In conjunction with the synoptic wind, it provides the energetic driving forces for the vertical fluxes of heat, mass, and momentum exchange. Thus, it becomes essential to understand such features as the thermodynamic behaviour of air and surface temperature and humidity, the dynamics of local airflow and boundary layer depth, and indirectly, the concentration of atmospheric pollutants (Oke 1988). The surface energy balance (SEB) equation can be presented in the following form:

$$Q^* = Q_H + Q_E + Q_G \, . \tag{1}$$

The partitioning of net radiation (Q^*) into the turbulent exchanges of sensible (Q_H) and latent (Q_E) heat with the atmosphere and the conductive exchange of sensible heat (Q_G) (Mills 2014).

There are four physical characteristics of urban areas which change the SEB. The micrometeorological processes take place between a surface during the day and the night in comparison to the rural areas, including (Hidalgo et al. 2008):

1. the scarcity of vegetation and the wide-scale use of impervious materials for buildings and pavements,
2. the ability of building materials to store and release a large amount of heat within a few hours,
3. the three-dimensional geometry of the urban surface (the “urban canyon” shape of streets),
4. the release of heat by human activities (traffic, space heating, space cooling, industry).

The urban surface energy balance (USEB) for the urban canopy (Arnfield 2003) is given by:

$$Q^* + Q_F = Q_H + Q_E + \Delta Q_s + \Delta Q_A \,, \tag{2}$$

where the new terms are: Q_F — heat released inside the canopy due to human activities associated with living, work, and travel and due to combustion of fuels as a heat source for the city (called anthropogenic heat flux), ΔQ_s – the net heat storage change by all the fabric of the city including its construction materials, trees, ground, and air contained in the canopy, and ΔQ_A – the net energy added to or subtracted from, the canopy by advection through any sides of the canopy.

The magnitude of Q_F in a city depends on its per capita energy use and population density. The largest Q_F values are found in densely inhabited cities with cold climates or cities with significant cooling needs. The value of Q_F for a typical temperate latitude is in the range of 15–50 Wm^{-2} (Oke et al. 2017).

2.5 Urban heat island

The most striking characteristic of the urban microclimate is the urban heat island (UHI). The UHI effect is widely recognised as a heat accumulation phenomenon, the most apparent characteristic of urban climate caused by urban construction and human activities (Yang et al. 2016). This phenomenon is generally experienced by an observer travelling between a city centre and its less urbanised surroundings (Hidalgo et al. 2008). Howard's study of the climate in London identified the urban heat island effect by comparing temperature records taken outside London (the "rural" temperature) with those collected by the Royal Society in the centre of London (Howard 1833).

Howard concluded that the mean temperature of the climate in the rural part is lower than in the more densely built-up parts of the metropolis, which is the effect of the population and fires, and it must be proportionately taken into account in the suburban parts.

The UHI effect causes the temperature to be warmer in the city centre than in the surrounding areas (Fig. 3; Hidalgo et al. 2008). The average land surface temperature difference between urban and rural areas reaches up to 12°C during the early night but is lower than during the daytime (Kłysik and Fortuniak 1999). The main reason is the urban-rural temperature contrast in the nocturnal cooling processes. These processes are forced by outgoing long-wave radiation because of the built-in urban structures. The urban structures absorb most of the incident radiation, store it, and release it as thermal radiation during the night (Oke 1997).

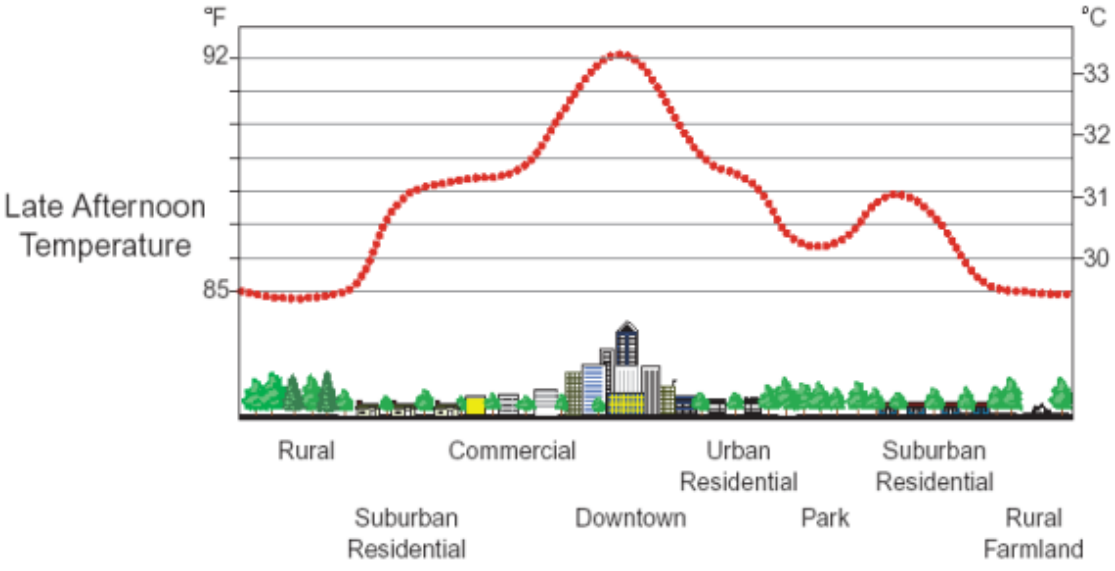

Fig. 3. Urban heat island profile (Kim 2009).

The time-varying characteristics of UHI generally follow a daily cycle, increasing during the late afternoon or early evening and reaching a maximum at night. Its intensity decreases after dawn and generally reaches a minimum during the morning hours (Hidalgo et al. 2008). Seasonal cycles also affect the frequency of UHI occurrence. UHI may be less frequent or weaker during rainy, cloudy, or windy seasons, while the opposite is true for conditions with a clear sky (Hidalgo et al. 2008). Based on Howard's investigations, processes responsible for UHI are multiple reflections, anthropogenic heating, lack of evaporation, and retardation of airflow (Mills 2008).

2.6 Urban canopy models

Urban canopy models (UCMs) represent urban areas for more accurate estimation of air temperature, wind speed, relative humidity, precipitation, surface temperature, and shortwave and long-wave radiation (Jandaghian et al. 2018).

Several UCMs were developed to simulate the surface energy transport and the flow dynamics in the lower urban atmosphere. The reduced computational cost of UCM (compared to full flow-resolving models), while preserving the essential physics, allows for the coupling of land surface models to mesoscale meteorological models (Wang 2011).

The main components required for urban climate impact simulation are physical processes controlling energy and water fluxes and urban morphology and urban materials' characterisation regarding aerodynamic, radiative, and heat transfer properties (Oleson et al. 2008).

Mesoscale meteorological models can be coupled with three types of urban canopy models: slab, single layer, and multi-layer to calculate heat and moisture fluxes from the surfaces to the atmosphere (Jandaghian and Berardi 2020).

The slab UCM (SB-UCM) is a one-dimensional model that considers buildings as increased roughness elements of urban areas (Jandaghian and Berardi 2020). Slab models represent the urban form as a flat horizontal surface with appropriate "bulk" radiative, aerodynamic, and thermal characteristics (Grimmond et al. 2010). Therefore, it assumes that buildings and roads have the same temperature and implicitly treats the surface layer's building height and coverage ratio (Garuma 2018). The SB-UCM disregards the variability of surface morphology among neighbourhoods (Jandaghian and Berardi 2020). The SB-UCM approach has the advantage of simplicity and reduced computational cost and parameter requirements (Grimmond et al. 2010). The slab model aims to calculate the effects of an urban canopy layer and provide energy and momentum fluxes to the atmosphere (Garuma 2018).

The Single-Layer Urban Canopy Models, SL-UCMs (Fig. 4), are based on simplified urban geometry but reasonably close to actual urban surfaces. The single-layer of the UCM (SL-UCM) was developed to represent urban geometry by considering street canyons and walls, roofs, and roads. An SL-UCM considers a single orientation of the two-dimensional approximation of streets (Jandaghian and Berardi 2020). This approach allows for more realistic representations of radiative trapping and turbulent exchange (Grimmond et al. 2010). Kusaka and Kimura (2004) developed a single layer urban canopy model that includes street canyons that are parameterised to represent the urban geometry, shadowing from buildings and reflection of radiation, the canyon orientation, and the diurnal change of the solar azimuth angle. The artificial surface consists of eight canyons with a different orientation, the multi-layer heat equation for the roof, wall, and road interior temperatures. Moreover, snow and water are usually treated in separate energy budgets (Garuma 2018).

The first and the simplest single-layer UCM is the Town Energy Balance (TEB) model developed by Masson (2000). Kusaka and Kimura (2004) also incorporated a single-layer urban canopy model into a simple two-dimensional atmospheric model to describe the fundamental impact of the urban canopy model but with an explicit treatment of canyon orientation. Lee and

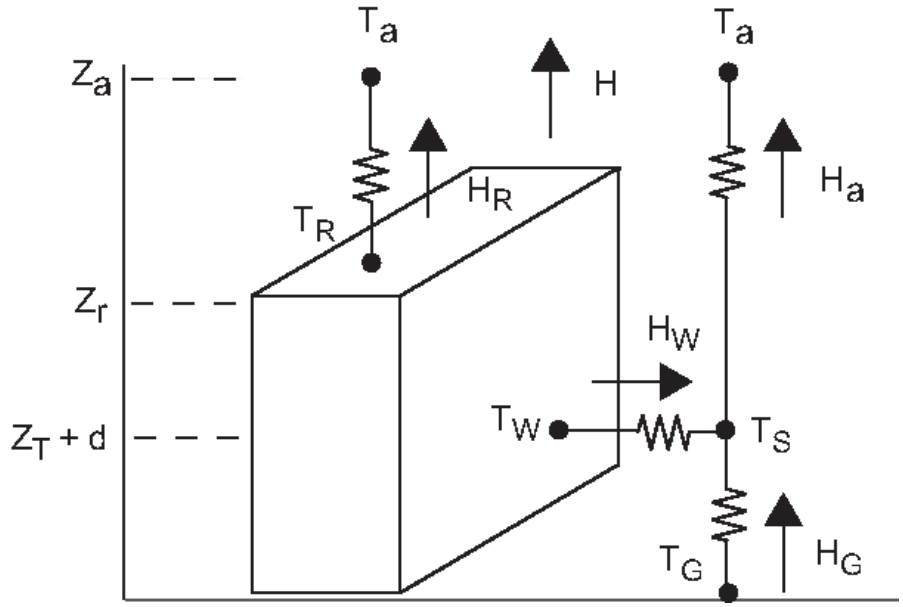

Fig. 4. Schematic of the single-layer urban canopy model. T_a is the air temperature, T_W is the building wall temperature, T_G is the road temperature, and T_S is the temperature defined at $Z_T + d$. H is the sensible heat exchange at the reference height. H_a is the sensible heat exchange from the canyon space to the atmosphere. Similarly, H_W is that from wall to the canyon space, and H_R that from the roof to the atmosphere (Kusaka and Kimura 2004).

Park (2008) added vegetation inside the street canyon. According to them, urban geometry comprises simple homogeneous buildings characterised by the canyon aspect ratio and the canyon vegetation characterized by the leaf aspect ratio and leaf area density profile. The multi-layer urban canopy model divides the canopy into many sub-layers down to the road surface. Therefore, it better represents the atmosphere in the urban canyon than both SL-UCM and slab models (Garuma 2018). ML-UCM computes the conservation equation for turbulence kinetic energy (TKE) and potential temperature to estimate heat emissions from the canopy by considering the drag force, diffusion factor, and radiation properties. The effects of shadowing, radiation trapping, and reflections are estimated for various building heights (Jandaghian and Berardi 2020).

The SL-UCM developed by Kusaka et al. (2001) and Kusaka and Kimura (2004) have been coupled into mesoscale atmospheric models such as Weather Research and Forecasting, WRF model by Chen et al. (2004) and Miao et al. (2009). The WRF/SL-UCM system has been applied in different cities such as Beijing (Miao and Chen 2008; Tewari et al. 2010; Miao et al. 2009), Guangzhou-Hong Kong (Wang et al. 2009), Houston (Chen et al. 2004; Jiang et al. 2008), New York City (Holt and Pullen 2007), Taipei (Lin et al. 2008). These studies evaluated the performance of the model against surface observations, atmospheric soundings, wind profile data, and precipitation data. The ML-UCM developed by Martilli et al. (2002), called Building Effect Parameterisation (BEP), allows for direct interaction with the PBL, recognises the three-dimensional nature of urban surfaces, and captures the vertical distributions of heat, moisture, and momentum throughout the whole urban canopy layer.

2.6.1 The town energy balance (TEB) model

Masson's Town Energy Balance (TEB) model simulates turbulent fluxes, net radiation, surface temperatures, and the partitioning between the turbulent and storage heat fluxes over urban areas (Masson et al. 2002).

The coupling of the TEB model with a mesoscale atmospheric model allows for the transfer of surface turbulent energy and moisture fluxes into the atmospheric model (Masson 2000).

TEB incorporates canyon geometry, with three typical surfaces: roof, wall, and road to reproduce the effects produced by buildings. A specific energy balance is computed for each of these three surfaces[2]. This approach is relatively simple, but it still allows most of the physical effects associated with the urban energy balance to be reproduced (Masson et al. 2002).

The fluxes should be computed for each land type by an appropriate scheme and then averaged in the atmospheric model grid, weighted by land type. For example, partitions should be: (i) sea; (ii) inland water; (iii) natural and cultivated terrestrial surface; and (iv) towns. The following fluxes are calculated: latent and sensible heat fluxes, upward radiative fluxes, and momentum fluxes (Masson 2000).

The original city representation in the TEB model is the following:

1. Buildings have the same height and width (in the model mesh), with the roof level at the surface level of the atmospheric model;
2. Buildings are located along identical roads, the length of which is considered far greater than their width; the space contained between two facing buildings is defined as a canyon;
3. Any road orientation is possible, and all exist with the same probability. This hypothesis allows the computation of averaged forcing for road and wall surfaces. In other words, when the canyon orientation appears in a formula (concerning the sun or the wind direction), it is averaged over 360 degrees. In this way, no discretisation is performed on the orientation.

Because of the presence of surface temperatures in the TEB scheme, the saturation specific humidity, and thus the turbulent latent heat flux, can be computed more easily. Both roofs and roads intercept the liquid precipitation, and there is runoff from roofs and roads to the drainage system. A certain amount of water can cover roads and roofs. These surfaces are impervious. Then, treating the fraction of the surface covered by water is more judicious than defining relative humidity. This part is saturated (fractional water pools), while the other part is assumed to be dry. Water evaporates when the air humidity is unsaturated until all water has disappeared from the impervious surface (Masson 2000). Two significant heat sources from the artificial cover towards the atmosphere based on the TEB approach are roofs and street canyons. The two flux contributions are averaged relative to their horizontal areas. This represents the mixing in the urban roughness sub-layer. In suburban environments, the averaging of the sensible and latent heat fluxes from the green-space artificial parts are supposed to parameterise the roughness sub-layer effects (Masson 2000).

2.7 Sensitivity analysis for urban climate simulations

The urban climate simulation includes parameterisations for microphysics, cumulus clouds, planetary boundary layer, radiation, land surface, as well as the urban canopy. The sensitivity analysis of meteorological parameters to different parameterisations allows researchers to select the most accurate model for urban climate simulations (Jandaghian et al. 2018). Mesoscale models with urban canopy parameterisations are used to study urban boundary layer processes.

Different studies show that such parameterisations are sensitive to the urban canopy parameters that define the urban morphology (Salamanca et al. 2011). For instance, Sharma et al. (2014) used four urban surface parameterisations to test the sensitivity of different complexities on urban parameterisation. The first scheme represented zero-order effects of urban surface, which performed the worst due to its weakness of not resolving key urban features. The second

[2]https://www.umr-cnrm.fr/spip.php?article199&lang=fr, last access on 16/02/2022

scheme was a 2-D street canyon, the third scheme, the multi-layer Building Environment Parameterisations (BEP), and the fourth scheme coupled BEP with multi-layer Building Environment Model (BEM) scheme.

Sharma et al. (2017) evaluated the simulation of summertime high temperatures and the sensitivity of these simulated phenomena to all the available urban parameterisation schemes employed in the urban-Weather Research and Forecasting (uWRF) model. Their results showed that including sub-grid scale variability of land-use and initialising models with well-defined land surface data can yield improved simulations of near-surface temperatures and wind speed.

Salamanca et al. (2011) used four urban canopy schemes, with different degrees of complexity, with the Weather Research and Forecasting (WRF) model to simulate the planetary boundary layer over the city of Houston, Texas (USA), for two days in August 2000. They concluded that if the purpose of the simulation requires only an estimate of the 2-m temperature, a simple bulk scheme is sufficient. Still, suppose the purpose of the simulation is to evaluate an urban heat island mitigation strategy or evaluate the energy consumption due to air conditioning at a city scale, it is necessary to use a complex urban canopy scheme and a detailed urban canopy parameter (Salamanca et al. 2011).

Daniel et al. (2019) carried out a sensitivity study over France. In their study, three different descriptions of land use and urban modelling were compared, including explicit description of cities with specific urban parameterisation (CITY), impervious urban covers as a rock (ROCK) and replacement of the cities by natural covers (VEG), corresponding to explicit modelling of cities with the urban canopy model TEB. It was shown that cities could influence their surrounding at a regional scale. By comparison with the VEG experiment, the French largest cities all induce a warming effect for near-surface temperature. Moreover, the intensity and spatial extent of the city's influence were more significant when using a detailed urban canopy model than for the ROCK experiment.

A single-layer urban canopy model offline and the surface energy balance data were used to evaluate the capability of the model to simulate the urban surface energy balance in Nanjing, China. The sensitivity analysis showed that the SL-UCM simulation is more sensitive to the roof and wall parameters than the road parameters. Based on the sensitivity analysis, a set of parameters was given for Nanjing suitable for winter simulations (Zhao et al. 2014).

Baklanov et al. (2008) performed a sensitivity analysis of the urban effects (urban albedo and roughness, anthropogenic heat flux, heat island, and urban aerosols on meteorology and air pollution with an urban-scale version of HIRLAM (HIgh Resolution Limited Area Model) NWP model. They also carried out the sensitivity tests of the offline versus online coupling of MetM and ACT models in Enviro-HIRLAM. Preliminary tests showed that the online integration of MetMs and ACTMs with consideration of the feedback of air pollution on meteorological processes and urban climate is a promising way to develop future environmental forecasting systems (Baklanov et al. 2008).

Sensitivity tests were carried out using a single-column version of the ALADIN-HIRLAM numerical weather prediction system. A set up with the HLRADIA simple broadband radiation scheme was used to study the impact of aerosol distribution and optical properties on radiative transfer, using climatological and real-time aerosol data (Rontu et al. 2020). Also, they determined that the most significant differences in radiative fluxes and heating rates were due to different aerosol loads. The larger the loads are, the more radiative fluxes and heating rates are sensitive to the aerosol inherent optical properties and the vertical distribution of the aerosol species.

3. DATA AND METHODS

This work studies the impact of different land use/land covers on the modelled urban atmospheric environment. The case study in the presented thesis is the city of Warsaw in Poland. The sensitivity study with the GEM model in a high-resolution configuration (1 km) was performed to assess the impact of the TEB urban parameterisation on a short-term meteorological forecast. Four cases representing different seasons with different weather patterns were selected.

This chapter explains the modelling tools and methods used to perform sensitivity studies and the features of selected cases concerning meteorological parameters.

3.1 The GEM Model

GEM (Global Environmental Multiscale) model is a global variable-resolution model designed to forecast weather over a broad range of scales, from the global scale down to the mesoscale (Côté et al. 1998). The GEM model was developed at the Canadian Meteorological Centre and is used for operational weather prediction in Canada (Côté et al. 1998).

There are three important motivations for modelling the atmosphere. These are to forecast the weather, address climate issues such as global change, and address air quality issues such as smog, stratospheric ozone depletion, and acid rain.

An urbanised version of the GEM mesoscale meteorological model was developed to improve the representation of surface and boundary-layer processes in the urban environment. This new system is used at grid scales between 200 m and 20 km (Lemonsu et al. 2009). The GEM model uses TEB parametrisation (Masson 2000) at these scales. The urban scheme was developed to simulate the specific physical processes in urban canopies (Lemonsu et al. 2010).

The GEM model with the TEB parameterisation was tested for Oklahoma City, Oklahoma (USA) at the resolution of 300 m for two observational periods of the Joint Urban 2003 experiment (Lemonsu et al. 2009). The results from the model showed that TEB parameterisation correctly simulates the urban microclimate, in particular the positive nighttime urban heat island. Moreover, the vertical structure of the boundary layer above the city was reasonably well simulated. Lemonsu et al. (2010) also studied TEB's performance under snowy conditions by focusing on radiation/energy exchanges and snow cover evolution using the Montreal Urban Snow Experiment (MUSE) dataset during the winter-spring transition period. The comparison of simulations with flux measurements showed that the system performs well when roads and alleys are snow covered.

3.2 Target area – the city of Warsaw

Warsaw is located in the centre of the country on the Vistula River – the largest river in Poland. Its area of almost 517 km^2 has significant differentiation of Land use/Land cover. Currently, about 248 km^2 is the built-up area (48%). A considerable part (about 57 km^2) is covered by industry, trade units, and transport systems. Forests make up about 15% of the city area. Urban parks and other recreational green areas cover 10% of the city. 12% of the city area is used as arable land for crops and pasture. The category "heterogeneous agricultural areas" includes sparsely built areas and allotment gardens — 11.3% (CORINE Land Cover 2007).

The current strategy of the city development is to build densely settled residential districts and insert new buildings into the free spaces in the city centre[3].

The city of Warsaw is located on flat terrain—the difference between the highest and lowest point is only 43 m. Western and southwestern winds prevail over the city. The main ventilation

[3]Strategic conceptions of conditions and directions of the spatial development of Warsaw witch changes, Legal act LXII/1667/2018, March 1, 2018, Council of Warsaw, 2018.

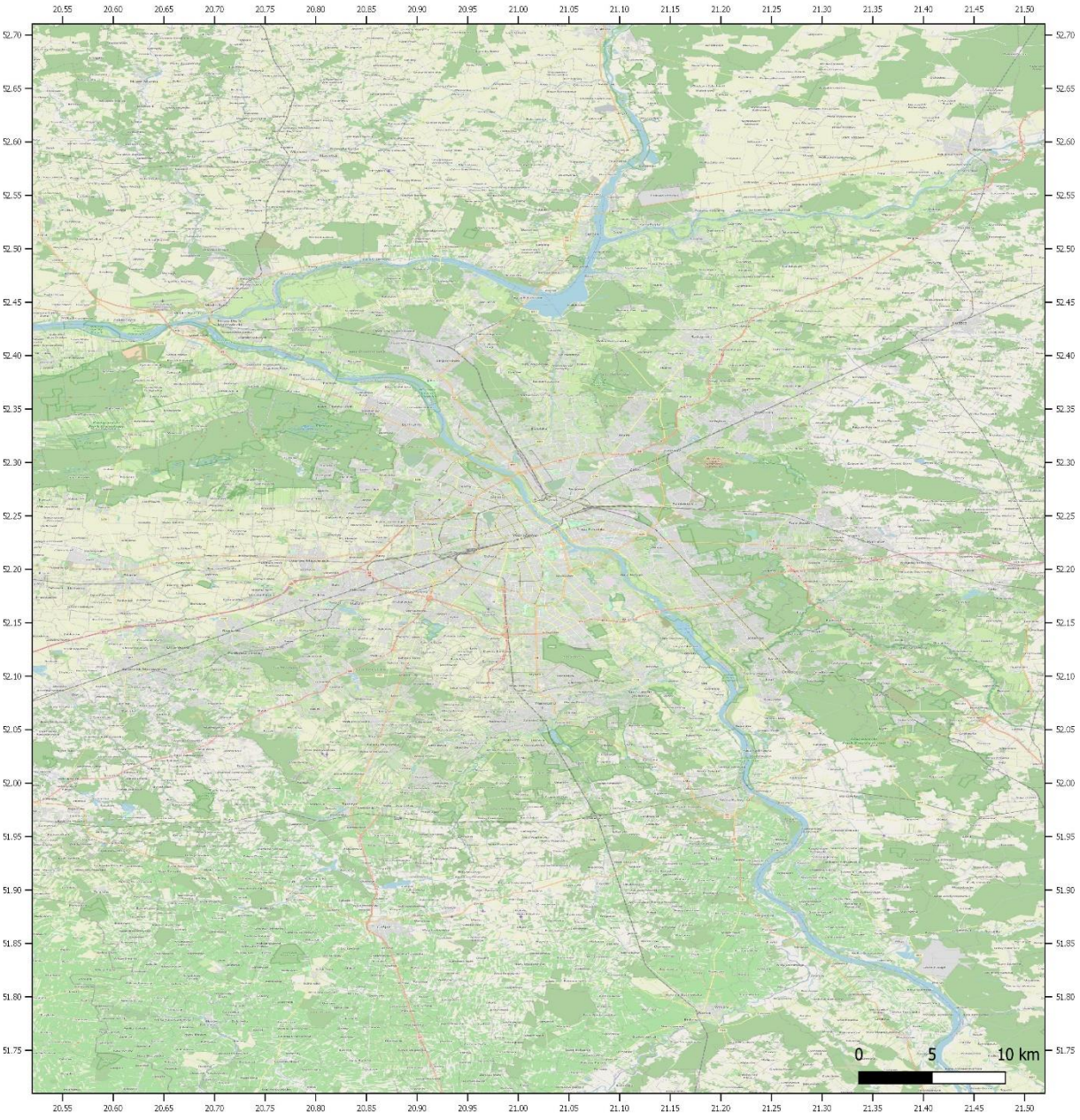

Fig. 5. The model domain obtained from https://www.openstreetmap.org.

corridor is the Vistula River Valley, which crosses the agglomeration (southeastern to northwestern direction). Figure 5 shows the map of the case study area.

3.3 CORINE Land Cover (CLC)

For the study, data for land-use from the CORINE land cover was used (https://land.copernicus.eu/European/Corine-land-cover). The first European and Polish CORINE (coordination of information on the environment) Land Cover (CLC) map was created for the reference year 1990, then subsequently for 2000, 2006, 2012, and 2018 (Hościło and Tomaszewska 2014). It consists of an inventory of land cover in 44 classes. CLC has a wide variety of applications, supporting various Community policies in the environment, agriculture, transport, spatial planning domains (land.copernicus.eu).

Three levels of CORINE land cover are presented in Fig. 6.

Fig. 6. CORINE Land Cover legend (https://www.eea.europa.eu/data-and-maps/figures/corine-land-cover-2006-by-country).

3.4 Urban modelling description and the TEB parameterisation

The 1-km global land-cover characteristics database (Loveland et al. 2000) is used in the GEM model for the land-use land-cover description. Land-cover regrouped into 26 land-use land-cover classes but with only one urban class, derived from the digital chart of the world (Lemonsu et al. 2009). The 26 vegetation types are standard GEM input presented in Table 1.

Table 1

26 vegetation types in GEM model

No.	Class	Z_0 [m]	No.	Class	Z_0 [m]
1	sea (water)	0.001	14	long grass	0.08
2	glacier	0.0003	15	crops	0.08
3	inland lake	0.001	16	rice	0.08
4	evergreen needle-leaf trees	1.5	17	sugar	0.35
5	evergreen broadleaf trees	3.5	18	corn	0.25
6	deciduous needle-leaf trees	1.0	19	cotton	0.1
7	deciduous broadleaf trees	2.0	20	irrigated crops	0.08
8	tropical broadleaf trees	3.0	21	urban	1.35
9	drought deciduous trees	0.8	22	tundra	0.01
10	evergreen broadleaf shrubs	0.05	23	swamp	0.05
11	deciduous shrubs	0.15	24	desert	0.05
12	thorn shrubs	0.15	25	mixed wood forests	1.5
13	short grass and forbs	0.02	26	mixed shrubs	0.05

TEB parameterisation represents the physical mechanisms inside the urban canopy and the exchanges between the built-up covers and the atmosphere (Lemonsu et al. 2009). TEB provides a land-use land-cover classification composed of 12 urban classes consisting of different urban landscapes (Lemonsu et al. 2009), summarised in Table 2 and some of the parameters proposed by Lemonsu et al. (2009) for the GEM model.

Table 2

Urban land-use categories in TEB – default settings for selected parameters in the GEM model

No.	TEB urban cover	Built-up fraction [0-1]	Average building height [m]	Anthropogenic heat flux [Wm^{-2}]
1	High buildings	0.95	39	30
2	Mid-high buildings	0.90	25	25
3	Low buildings	0.9	13	30
4	Very low buildings	0.85	8	30
5	Industrial areas	0.85	8	50
6	Sparse buildings	0.40	12	15
7	Roads and parking areas	0.98	5	30
8	Road borders	0.70	5	30
9	High-density suburbs	0.44	5	15
10	Mid-density suburbs	0.27	5	15
11	Low-density suburbs	0.18	8	15
12	Mix of built/nature	0.25	8	0

3.4.1 The land surface of Warsaw

The land-use data obtained from the CORINE land cover[4] were associated with corresponding categories in the TEB parameterisation using the QGIS tool. Table 3 shows Warsaw's urban land use based on the TEB classification.

In the next step, the calculated fractions of each class are shown in Fig. 7. These fractions were used as the input file for the GEM model.

Table 3

Urban land-use categories in TEB vs CORINE land cover

No.	TEB urban cover	CLC code	CLC
1	High buildings		
2	Mid-high buildings	111	Continuous urban factor
3	Low buildings		
4	Very low buildings		
5	Industrial areas	133	Industrial or commercial sites
		122	Construction sites
6	Sparse buildings	112	Discontinuous urban factor
7	Roads and parkings	121	Road and rail network and associated land
8	Road borders		
9	High-density suburbs		
10	Mid-density suburbs		
11	Low-density suburbs		
12	Mix built and nature	141	Green urban areas
		211	Non-irrigated arable land

3.5 GEM model set up

In this study, the GEM model setup is based on the limited area version of the GEM model (GEM-LAM). Limited area models are widely used in numerical weather prediction and regional climate modelling to obtain high-resolution results computationally too expensive with a global model.

The GEM model was initialised using meteorological initial conditions taken from the Canadian Meteorological Centre (CMC) global assimilation system with the resolution of ~35 km (Gauthier et al. 1999, 2007; Laroche et al. 2007). The model was run in a cascade mode. The first model was run on a global variable resolution domain with a horizontal grid spacing of ~5 km over Central Europe. The output from the regional run was used to drive the model for the presented experiments and for further cascade to 1 km. Initial and boundary conditions from the global run were used for nesting the limited area model (LAM) with ~1 km grid spacing. Nesting from the regional model was done every hour. The limited area model was run on 120 × 120 grid pints with a 15 s time step. The boundary condition (buffer zone) was set at 10 grid pints. Modelling results were analysed on the domain's inner part of 100 × 100 grid points. The model domain had 28 pressure hybrid levels in vertical, with 10 levels in the first 3 km. The model top was at 10 hPa (~30 km).

[4] https://land.copernicus.eu/pan-european/corine-land-cover", last access: 30/09/2020

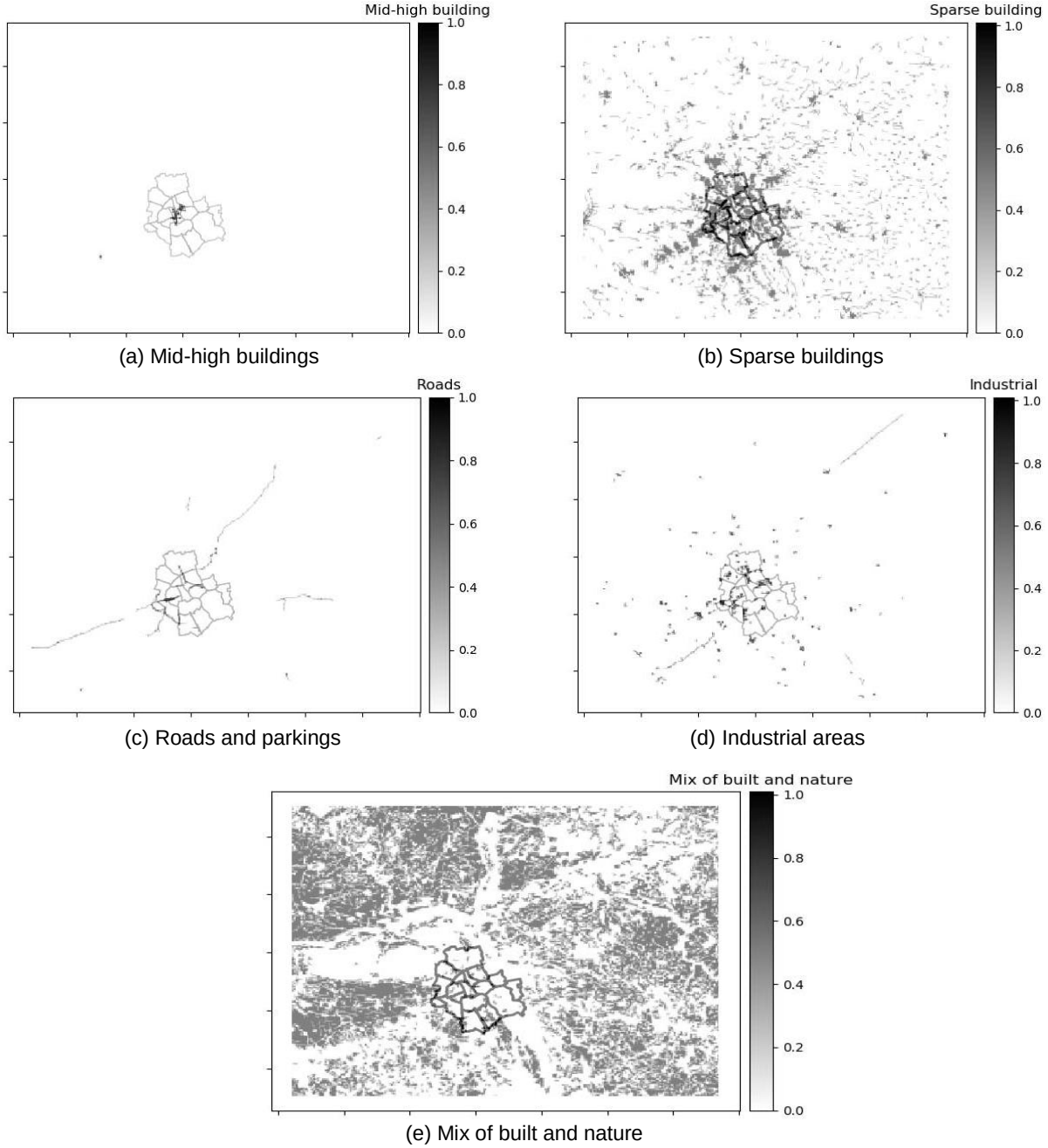

(a) Mid-high buildings (b) Sparse buildings

(c) Roads and parkings (d) Industrial areas

(e) Mix of built and nature

Fig. 7. The fractions of: a) mid-high buildings, b) sparse buildings, c) roads and parkings, d) industrial areas, and e) mix of built-up and nature areas in the TEB classification for Warsaw.

According to Fig. 7, mid-high buildings are in the centre of Warsaw, the rest of the city is covered with sparse structures, and the mix of built-up and nature areas is primarily located in the outskirt of Warsaw.

3.5.1 Modelling scenarios

Four one-day cases representing different meteorological conditions were selected. The forecast length is 24 hours (starting 06:00 UTC) with the time step of 15 s.

1. January 29, 2010; Winter case
2. April 24, 2010; Spring case

3. June 6, 2010; Late spring case
4. July 23, 2010; Summer case

Two types of simulations were performed to analyse the impact of the urban parametrisation on modelled meteorological parameters:

- A reference run without the TEB parametrisation, so it contains 26 land-use land-cover classes within the GEM model, including a single urban class (Table 2);
- The urban scenario with the TEB classification of urban land cover (Table 3).

The characteristics of the model setup and cases are summarised in Table 4. Analysis was done based on the output obtained from the average of 10 grid points from the centre of the model (centre of the city) in two directions – i.e., 20 grid points in total – which is 8% of the whole domain (excluding the absorber zone). The domain of the analysis is presented in Fig. 8.

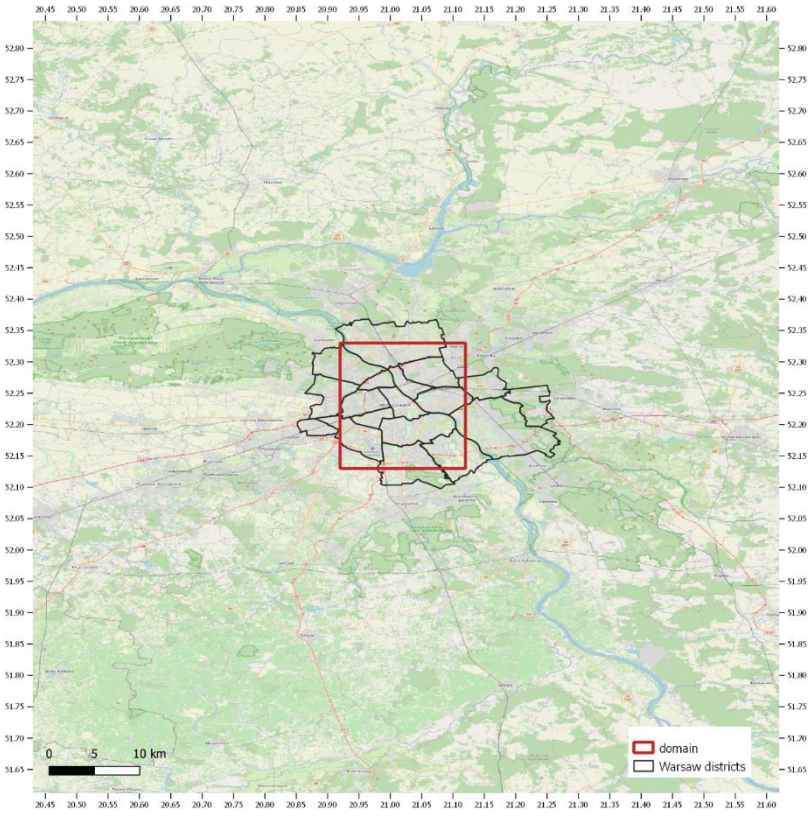

Fig. 8. Selected domain of analysis (https://www.openstreetmap.org).

Table 4

Description of the model setup and four one-day cases

No.	Cases	Resolution [km]	Grid	Initial time	Duration [h]
1	January 29, 2010	1	120 × 120	06:00 UTC	24
2	April 24, 2010	1	120 × 120	06:00 UTC	24
3	June 6, 2010	1	120 × 120	06:00 UTC	24
4	July 23, 2010	1	120 × 120	06:00 UTC	24

3.5.2 Sensitivity analysis

The TEB module (Masson 2000) was run online in an interactive mode in the GEM model. The modelling setup was used to run scenarios for sensitivity analysis for three different scenarios with different descriptions of land use and land cover for urban areas:

- City scenario using the TEB classification (TEB-CLC) (Table 3),
- High building scenario where the city is covered with impervious high buildings land cover (TEB-HB),
- Vegetation only for which city is replaced by the surrounding natural covers (TEB-VEG).

In the second scenario (TEB-HB), the sparse buildings category from the TEB urban cover was replaced by high buildings. In the third scenario (TEB-VEG), all the categories from the TEB urban cover were substituted by forest and vegetated areas as defined in TEB.

The 24-h simulations began at 06:00 UTC. A set of 12 simulations (3 urban schemes for every selected day) were performed to study the sensitivity of different meteorological parameters to three surface land covers. The urban model set-up resembles the city of Warsaw. The percentage of each urban land-use category in TEB for each scenario is presented in Table 5.

Table 5

Percentage of different TEB categories
in three TEB-CLC, TEB-HB, and TEB-VEG scenarios

TEB classifications	TEB-CLC	TEB-HB	TEB-VEG
Mid-high buildings	0.12%	10.97%	0
Sparse buildings	10.85%	0	0
Roads and parking areas	0.36%	0.36%	0
Industrial areas	1.11%	1.11%	0
Mix built and nature	43.92%	43.92%	0
Other (forests, agricultural lands, water bodies)	43.64%	43.64%	100%

3.6 Model output

The meteorological parameters, including temperature, specific humidity, precipitation rate, and turbulent kinetic energy, were calculated by the model and analysed to:

- describe the diurnal cycle of the parameters as mentioned earlier,
- reproduce some of the most important urban boundary layer features and study urban influences on the structure of the boundary layer.

The analysis was done for two setups without and with the TEB parameterisation.

3.7 Meteorological conditions

Meteorological synoptic conditions for the selected cases are presented in the following sections.

3.7.1 January 29, 2010

From January 27 to 31, Poland was under the influence of low-pressure systems with atmospheric fronts. The main low-pressure centres were located over Ukraine, the North Sea, and Scandinavia. A slightly warmer and humid polar-sea air mass was advected over Poland from the west, which brought an overcast sky with more showers and intermittent heavy snowfall.

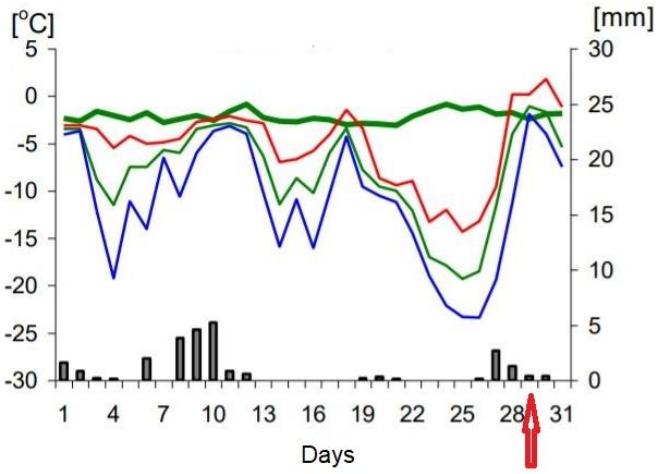

Fig. 9. Average daily and extreme air temperatures as well as a daily sum of precipitation in January 2010 in Warsaw (https://danepubliczne.imgw.pl/data/dane_ pomiarowo_obserwacyjne/Biuletyn PSHM). In this graph, the black bars show the sum of precipitation on each day of January 2010, thick green line the daily average temperature from 1971 to 2000, the thin green line the daily average temperature of January 2010, the blue line the min temperature, and red line the maximum temperature.

Figure 9 shows the average daily and extreme temperature and precipitation in January 2010.

In Warsaw, the standard deviation of the average daily temperature from 1971 to 2000 was −6°C, and during a month, the total rainfall was 25.2 mm, which is 114% of the long-term average.

3.7.1.1 April 24, 2010

April 2010 was unusually warm in Warsaw, and the southern part of the Mazovia voivodship was extremely dry.

From April 23 to 30, the cold air of Arctic origin initially advected from the north and later warm polar-maritime air from the south-west.

Figure 10 shows the average daily and extreme temperature and precipitation in April 2010. April 24 recorded the lowest minimum temperature in this month. In Warsaw, during a month,

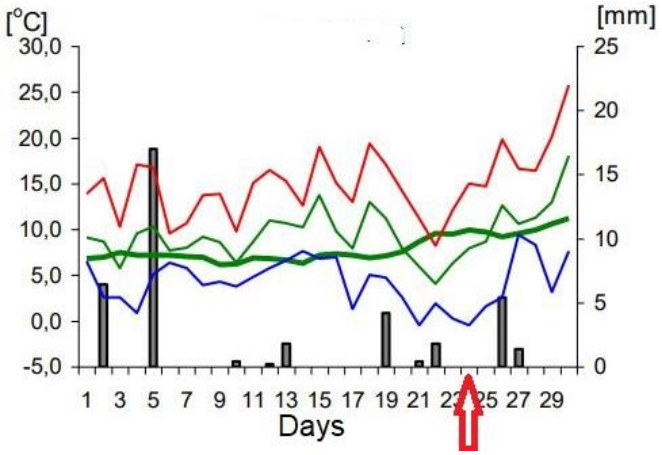

Fig. 10. Average daily and extreme air temperatures as well as a daily sum of precipitation in April 2010 in Warsaw (https://danepubliczne.imgw.pl/data/dane_pomiarowo_obserwacyjne/Biuletyn_PSHM). In this graph, the black bars show the sum of precipitation on each day of April 2010, thick green line the daily average temperature from 1971 to 2000, the thin green line the daily average temperature in April 2010, the blue line the min temperature, and the red line the maximum temperature.

the sum of rainfall was 39.0 mm, 112.6% of the long-term average, although there was no precipitation on April 24, 2010 (https://danepubliczne.imgw.pl/data/dane_pomiarowo_obserwacyjne/Biuletyn_PSHM).

3.7.1.2 June 6, 2010

On June 5 and 6, the polar-maritime air mass dominated the country. It was cloudless or overcast with almost no precipitation. The wind was weak, with periods of moderate, and it was variable with a predominance from the south.

Figure 11 shows the average daily and extreme temperature and precipitation in June 2010. In Warsaw, the average monthly temperature was 17.8°C.

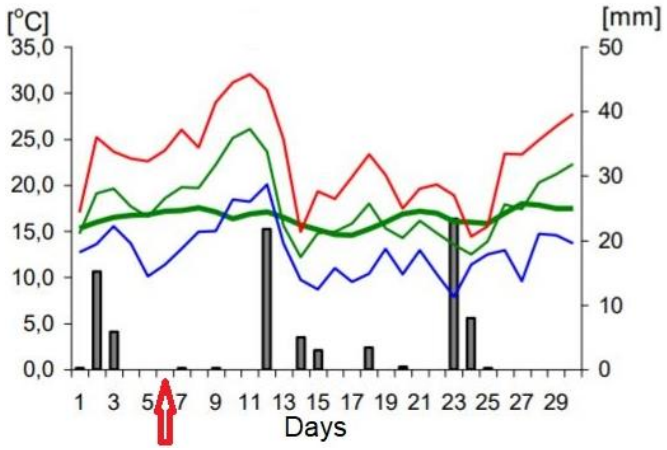

Fig. 11. Average daily and extreme air temperatures as well as a daily sum of precipitation in June 2010 in Warsaw (https://danepubliczne.imgw.pl/data/dane_pomiarowo_obserwacyjne/Biuletyn PSHM). In this graph, the black bars show the sum of precipitation on each day of June 2010, thick green line the daily average temperature from 1971 to 2000, the thin green line the daily average temperature in June 2010, the blue line the min temperature, and red line the maximum temperature.

3.7.1.3 July 23, 2010

From July 23 to 31, Poland was within a low-pressure system with atmospheric fronts. This period was the wettest period of the month. The first front moved on July 23 and 24. These

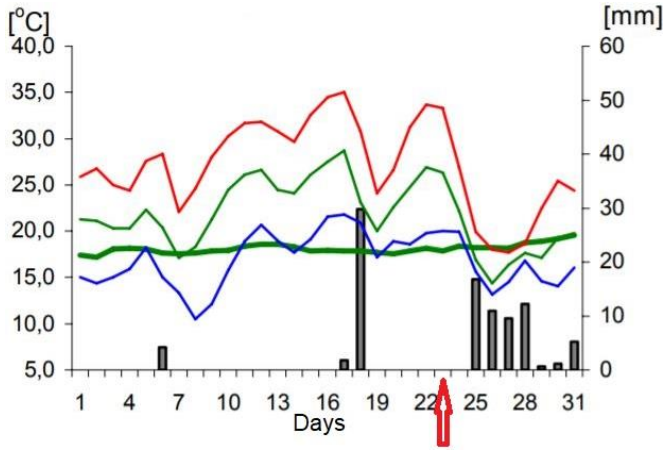

Fig. 12. Average daily and extreme air temperatures as well as a daily sum of precipitation in July 2010 in Warsaw (https://danepubliczne.imgw.pl/data/dane_pomiarowo_obserwacyjne/Biuletyn PSHM). In this graph, the black bars show the sum of precipitation on each day of July 2010, thick green line the daily average temperature from 1971 to 2000, the thin green line the daily average temperature in July 2010, the blue line the min temperature, and red line the maximum temperature.

days, the cold, polar-maritime air advected into the western districts and the hot and humid tropical air mass over the central and eastern parts. Until the end of the month, Poland remained in the polar-maritime air mass, cool in the west and warm in the east (https://danepubliczne.imgw.pl/data/dane_pomiarowo_obserwacyjne/Biuletyn_PSHM).

Figure 12 shows the average daily and extreme temperature and precipitation in July 2010. In Warsaw, the average monthly temperature was 21.9°C, which exceeds the 30-year average by 3.8°C. July 23 was recorded as one of the hottest days in July 2010.

3.8 Observational data

Road Weather Observational Network (Zarząd Oczyszczania Miasta, ZOM) has a network of 18 measurement stations located in Warsaw. The network is designed to monitor road conditions. Therefore, each station is located close to the street. Most of the sensors are mounted on lampposts (streetlights) along streets.

Measurements are made every ten minutes. The following parameters are measured at each station:

- air temperature,
- surface road temperature,
- relative air humidity,
- wind speed at 9.5 meters,
- wind direction,
- turbulent sensible heat flux calculated by profile method (using temperature and wind speed gradient).

Six stations were selected to do the statistical evaluation, including: Puławska, Jelonki, Krakowska, Radzymińska, Jerozolimskie, and Bielany stations.

These stations were chosen because they were in the domain taken for the analysis. The stations are away from tall buildings. Sensors measuring the road surface temperature are embedded in the road and located in the traffic lane's centre.

The height of the measuring sensors varies. The lowest air temperature sensor is installed at the Krakowska station. The highest wind sensor is located at the Puławska station, and the lowest is at the Krakowska station. At each station, the height of the measuring instruments is higher than the average height of the terrain obstacles. The terrain obstacles causing high average values are in the vicinity of the Puławska station, a street viaduct. Table 6 presents the thermometer height and mean height of roughness elements within 250 m from the stations.

Table 6

Observational instruments heights and mean height of roughness elements located within 250 m from the stations (Gawuc et al. 2022)

Stations	Thermometer height [m]	The average height of terrain obstacles [m]	Height of the station above sea level [m]
Jelonki	3.00	1.10	112.26
Krakowska	5.78	1.60	109.96
Puławska	3.40	3.00	104.44
Bielany	4.30	0.63	86.24
Jerozolimskie	3.40	–1.44	114.89
Radzymińska	3.20	1.28	84.56

Station locations are shown in Fig. 13. The Bielany station is located at Wybrzeże Gdyńskie street. It is a busy exit street from Warsaw. A dense forest surrounds the station. The Vistula River is at the north. The Jelonki station is located at Połczyńska street. The station's surroundings are typical single-family houses with lots of trees. The Jerozolimskie station is located on the avenue with the same name. It is a busy four-lane road. Office buildings and meadows surround the station, with individual buildings at a great distance from each other. Puławska station is located at the intersection of Pileckiego and Puławska street. It is a station surrounded by tall residential buildings, medium-high buildings, or office buildings. The Radzymińska station is located on the road with the same name. A large single-family low-rise housing area surrounds the station. Jelonki and Radzymińska stations are located in the area with low-single family houses with a large fraction of vegetation. The Bielany station is located near a dense forest (Las Bielański).

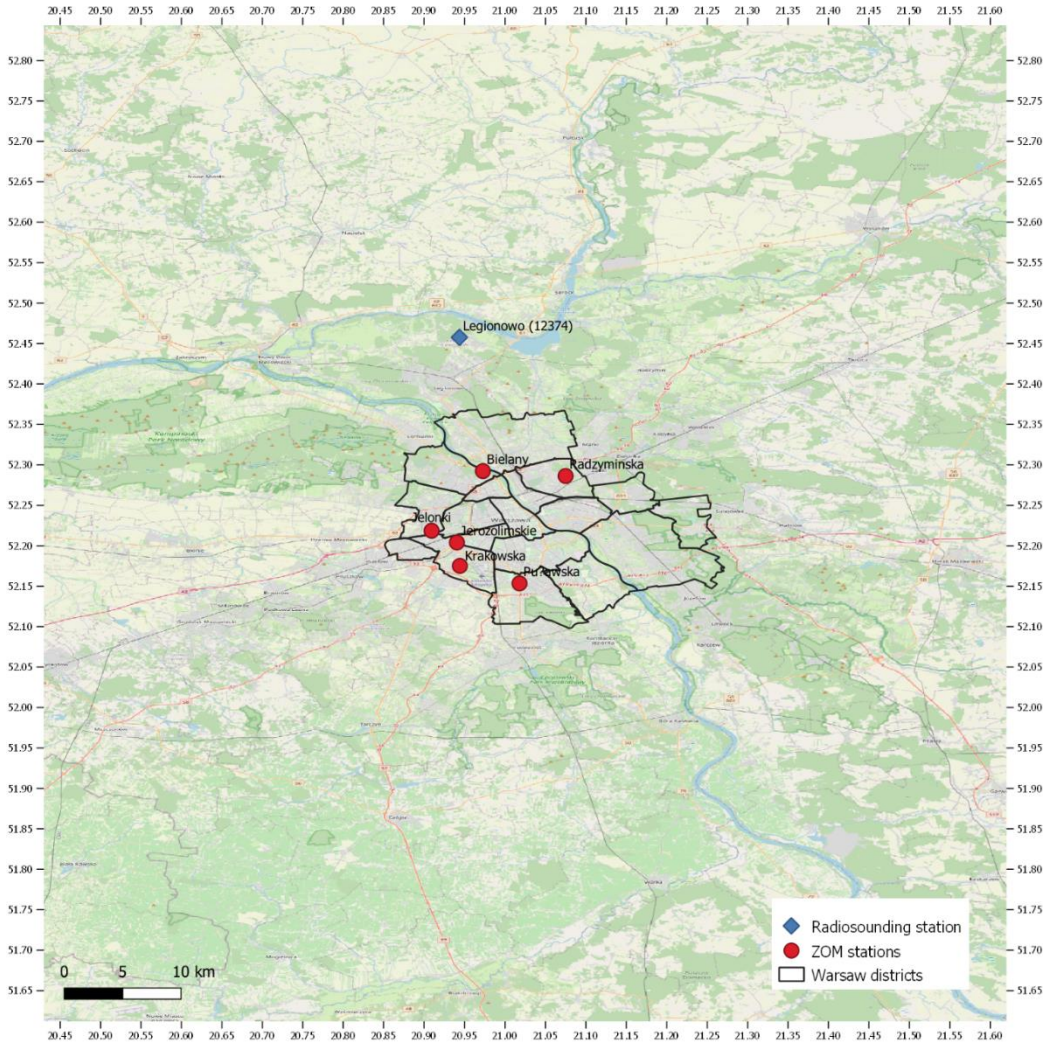

Fig. 13. The location of the ZOM stations (red points) and radiosounding station (blue point) (https://www.openstreetmap.org).

3.8.1 Vertical profiles evaluation with soundings

Vertical profiles of temperature taken from the model (NOTEB and TEB scenarios) of seven levels (~1500 m) were compared with the radiosoundings obtained from the Legionowo station (Table 7). The location of this station is presented in the map of the model domain in Fig. 13.

Table 7

Radiosounding station selected for comparison with model results

Station	No.	GMT	Latitude	Longitude
Legionowo	12374	0.12	52.40	20.96

4. RESULTS AND DISCUSSION

This study selected four one-day cases from 2010 with different weather conditions representing winter, spring, late spring, and summer. Four one-day cases presented in Table 8 give a good sample of weather patterns over Poland and specifically over the city of Warsaw for these seasons.

Table 8

The summary of main characteristics of the four one-day cases

	Winter 29 January	Spring 24 April	Late spring 6 June	Summer 23 July
Main characteristics	Moderate wind, cloudiness, cold air mass, snowfall (1 mm)	Moderate wind, clear sky, no precipitation	Weak wind, clear sky, no precipitation	The frontal passage (day-time), clear sky (night-time), no precipitation
Temperature	max = 0°C min = −2°C	max = 14°C min = 7°C	max = 23°C min = 16°C	max = 33°C min = 22°C

Results presented in this chapter are divided into three parts: The first part focuses on the boundary layer structure over Warsaw, comparing NO-TEB and TEB scenarios. The second part discusses the sensitivity analysis considering three scenarios: TEB-CLC, TEB-HB, and TEB-VEG and how the urban heat island changes with different land covers.

The last part studies the difference between the modelling results and the measured data obtained from the ZOM stations.

4.1 Boundary layer analysis

The boundary layer profiles and temperature cross-sections over Warsaw were studied for two NO-TEB and TEB scenarios based on the 26 land-use land-cover classes in the GEM model. Vertical profiles of temperature, specific humidity, potential temperature, and turbulent kinetic energy to the height of 3000 m were studied for four one-day cases. The location of the cross-sections studied in this section is shown in Fig. 14.

4.1.1 C1 – Winter case

Radiation inversions are more common during winter, when the outgoing longwave radiation exceeds the incoming solar radiation. As presented in Fig. 15, on January 29, at 07:00 UTC, the NO-TEB scenario shows an inversion at low altitudes. After the sunrise, in the morning, the inversion still can be observed. On the other hand, the TEB scenario does not show the inversion early in the morning due to the warmer surface. During the day, a weak inversion exists in the NO-TEB scenario, while there is no inversion in the TEB scenario. After sunset, a strong inversion occurs, deeper and stronger for the NO-TEB scenario. The inversion occurs after the sunset and its thickness and strength increase with time. However, the intensity of inversion for

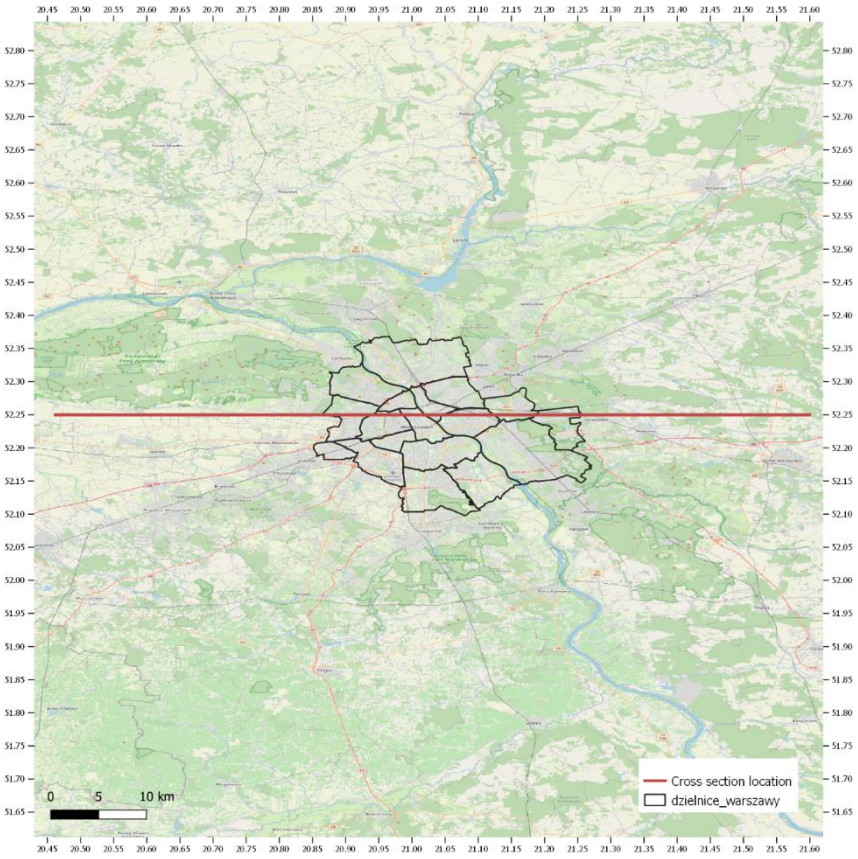

Fig. 14. The location of the cross-sections in the map (https://www.openstreetmap.org).

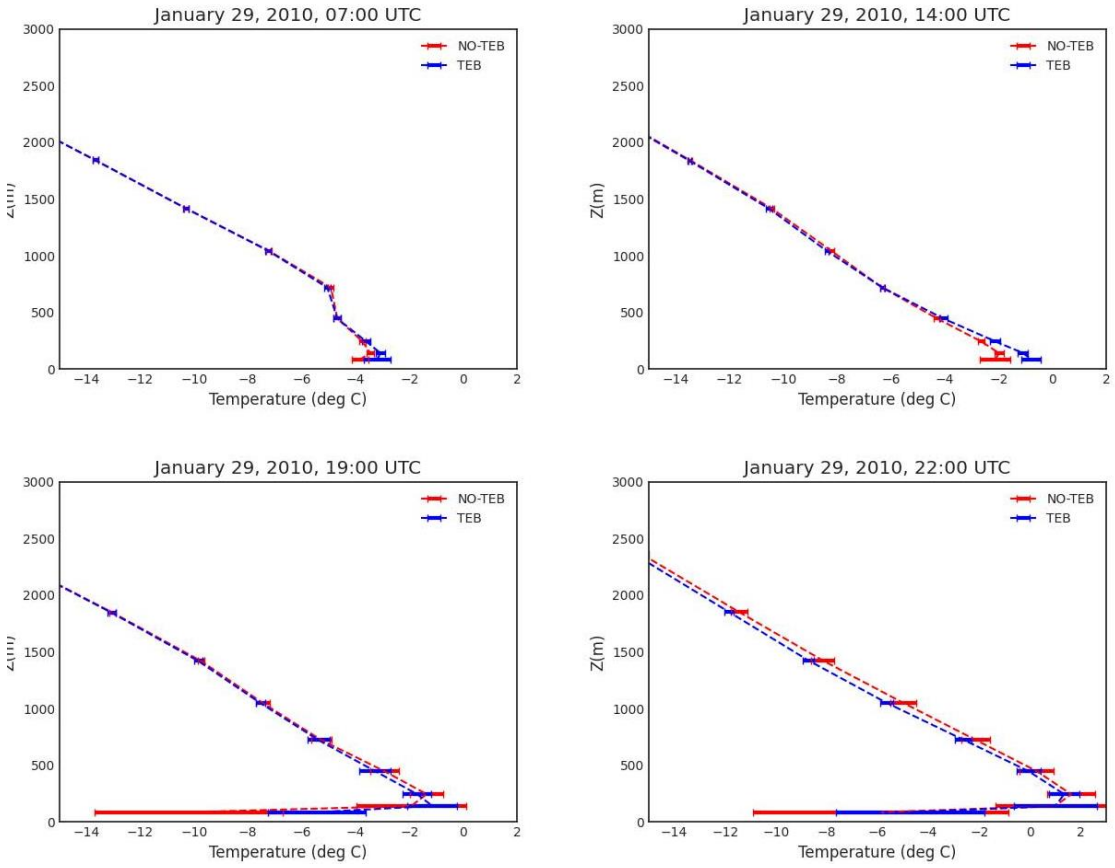

Fig. 15. Vertical profile of temperature on January 29, 2010, for NO-TEB and TEB scenarios. Error bars present the standard deviation.

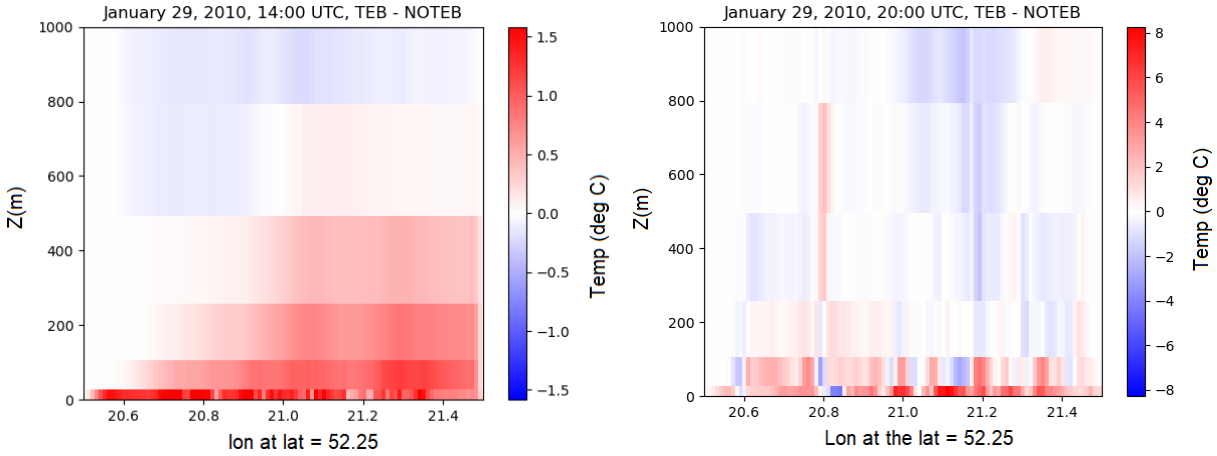

Fig. 16. Cross-section of temperature difference between TEB and NO-TEB scenario on January 29, 2010, during the day (left), and during the night (right).

the TEB scenario is weaker. The variability of the temperature has been presented in the plots with standard deviation as error bars. There is a very weak variability in the higher altitudes, and a strong variability in the lower altitudes after the sunset.

Figure 16 presents the cross-section of the temperature difference between the TEB and NO-TEB scenario on January 29, 2010. The temperature vertical cross-section shows changes of temperature spatially and gives a better understanding of the status of the boundary layer between the two scenarios. The temperature gradient during the day clearly shows that the urban area is warmer than the no urban area, and the temperature decreases with altitude. However, the atmosphere above the urban area is also warmer in the upper levels up to 500 m.

The temperature cross-section at night shows surface-based inversion in both scenarios. It can be seen that the inversion in the NO-TEB scenario is stronger than the TEB scenario, particularly in the city centre. However, the atmosphere just over the city surface is warmer than in the no urban scenario, and since there is no significant mixing at night in the stable boundary layer, the impact of the warmer surface is up to the height of ~100 m (near-surface). The anthropogenic heat flux (AHF) impact is important due to the lower absorbed solar radiation in winter. Therefore the temperature is higher in the TEB scenario than in the NO-TEB scenario, especially at night due to residential heating. There is an area with the latitude/longitude coordinates of 52.24, 20.82 with the warmer surface in the NO-TEB scenario compared to the TEB scenario. This place is an open non-irrigated land next to the Kampinoski National Park. This area in the TEB model based on the initial parameterisation is considered a “mix of built and nature” category with a zero AHF, while in NO-TEB scenario is considered to be a green area based on GEM model vegetation types. Most forests are warmer than open land in the mid-latitudes during the night. The NO-TEB scenario is warmer than the TEB scenario in this area.

The slope of the potential temperature profile directly indicates static stability (Stull 1988). Figure 17 illustrates the virtual potential temperature profile over Warsaw starting just before sunrise. At 07:00 UTC, there is a stable boundary layer in both scenarios because the potential temperature increases with height. Therefore, there is an inversion that is stronger for the NO-TEB scenario.

Due to the warmer surface in the TEB scenario (Fig. 17), convection already starts to mix warm air up throughout the stable boundary layer and then expands to the mixed layer. At 09:00 UTC, the NO-TEB scenario is still stable, and there is a persistent inversion in the near-surface layer during the day but at a lower altitude. On the other hand, in the TEB scenario, the convective mixed layer is formed at a lower altitude (~100 m), and since the potential tempera-

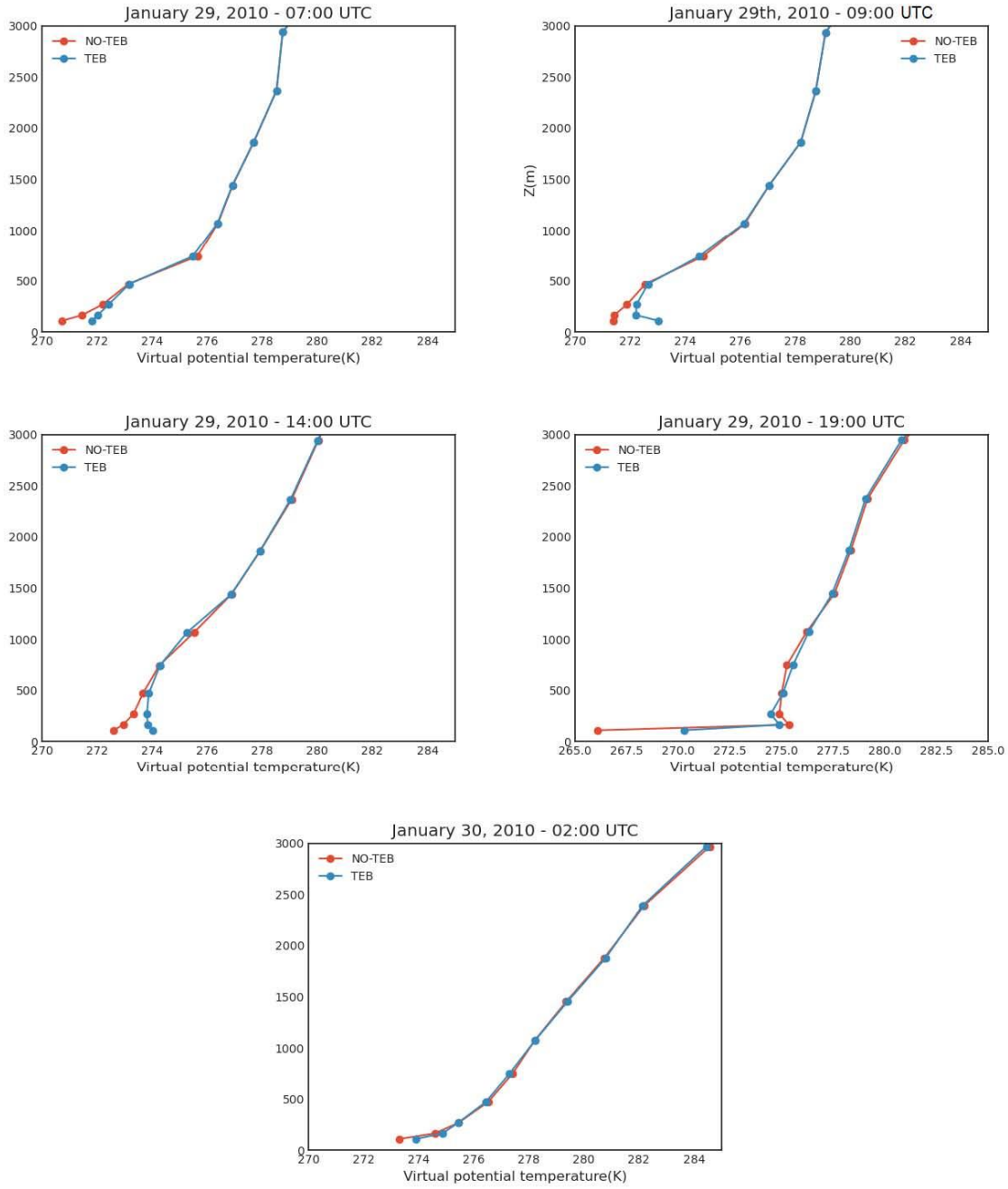

Fig. 17. Vertical profile of virtual potential temperature on January 29, 2010, for NO-TEB and TEB-scenarios.

ture decreases with height, there is an unstable boundary layer. Later after midday, surface heating causes the air near the surface to be of a higher virtual potential temperature than the air just above it, so the air is superadiabatic and, having a vertical slope of the potential temperature, the atmosphere is neutral in the TEB scenario. After the sunset, the NO-TEB scenario preserves the stable atmosphere and forms an intense inversion layer. The surface cools down after sunset in the TEB scenario, and the near-surface layer becomes stable with a temperature inversion.

The specific humidity usually decreases with height. However, there are layers where specific humidity increases with height. This means humidity inversion has taken place in these layers. The increase in specific humidity with height within inversions results in a downward moisture flux. Based on Fig. 18, there is the simultaneous occurrence of the low-level humidity

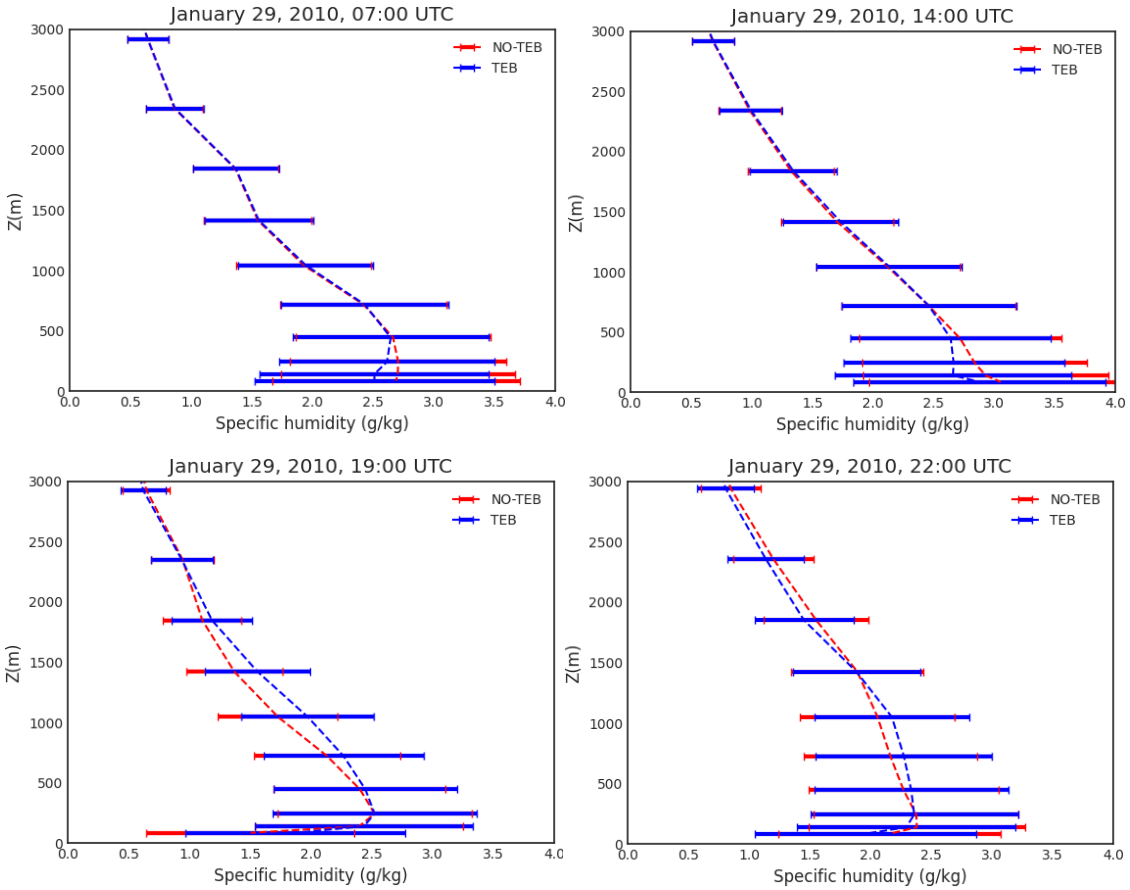

Fig. 18. Vertical profile of specific humidity on January 29, 2010, for NO-TEB and TEB scenarios. Error bars present the standard deviation.

inversion and temperature inversion at night. The simultaneous occurrence of both surface-based inversion types is extremely rare, but in Europe, it reaches a relatively high frequency at night-time in winter (Palarz and Celiński-Mysław 2020). Nygård et al. (2013) and Brunke et al. (2015) studied the humidity inversion over the polar regions and examined various vertical ranges in the troposphere. According to their findings, over the Arctic and Antarctic, almost half of the humidity inversion is accompanied by temperature inversion. In comparison, Wypych and Bochenek (2018) stated that over Europe, approximately 70% of surface-based humidity inversions occur simultaneously with a temperature inversion and can be up to 90% over Eastern Europe. Palarz and Celiński-Mysław (2020) found that one of the most frequent locations of humidity inversion development is in Eastern Europe in winter. Being in the area influenced by the extensive high-pressure systems, with large-scale subsidence and adiabatic heating of air parcels, results in temperature inversion development and enhances moisture condensation and eventually humidity inversion formation (Palarz and Celiński-Mysław 2020).

There is a shallow boundary layer after sunrise, which is mainly in the TEB scenario due to the warmer surface (Fig. 19); therefore, during the day, there is turbulence in the lower altitudes due to the thermal effects. As a result, there is a stronger turbulent kinetic energy near the surface in the TEB scenario. Another reason for higher near-surface TKE is the higher surface roughness in the urban area. As it was found by Hagen (1854) and Darcy (1857), the roughness affects pressure drop by increasing the drag force and blockage effects.

Considering the temperature cross-section in Fig. 16, the higher temperature at night in the higher levels still can be observed in the TEB scenario, which can be the reason for higher TKE at the higher levels. The higher TKE in higher altitudes in both scenarios – particularly the NO-

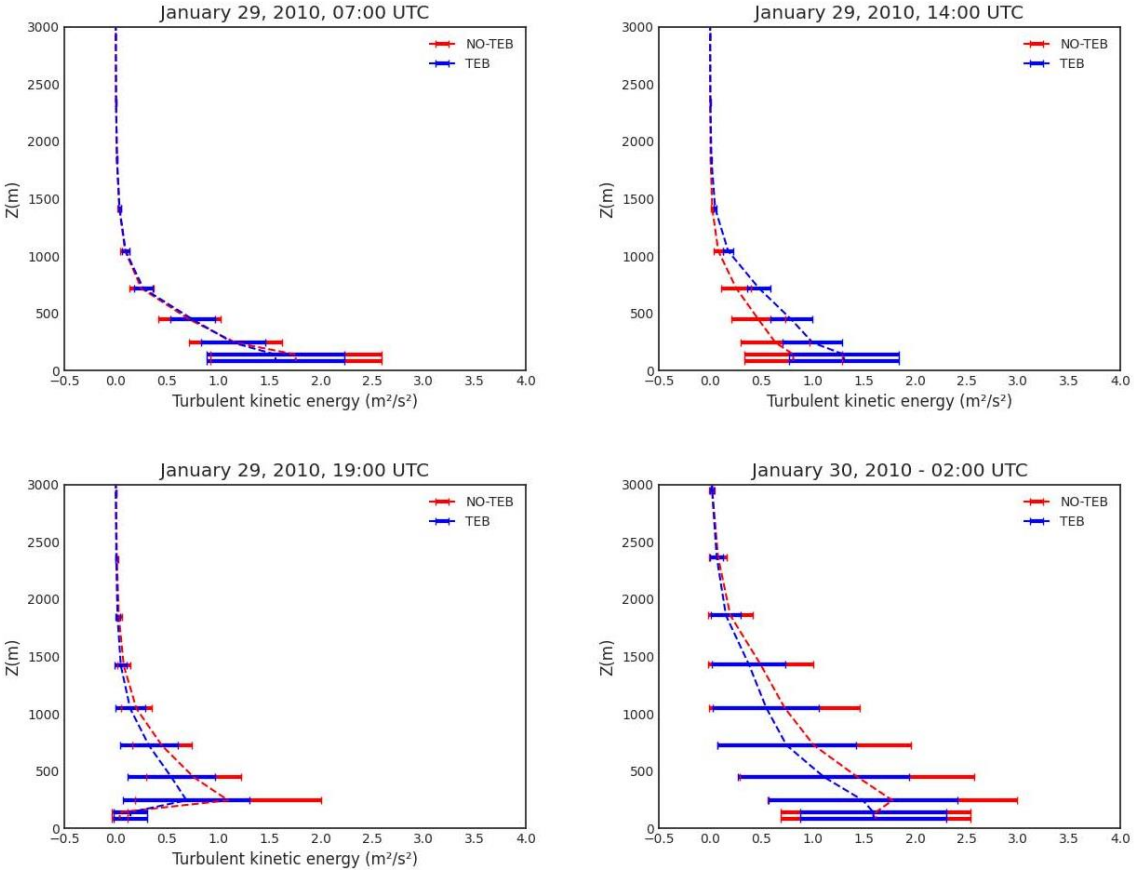

Fig. 19. Vertical profile of turbulent kinetic energy on January 29, 2010, for NO-TEB and TEB scenarios. Error bars present the standard deviation.

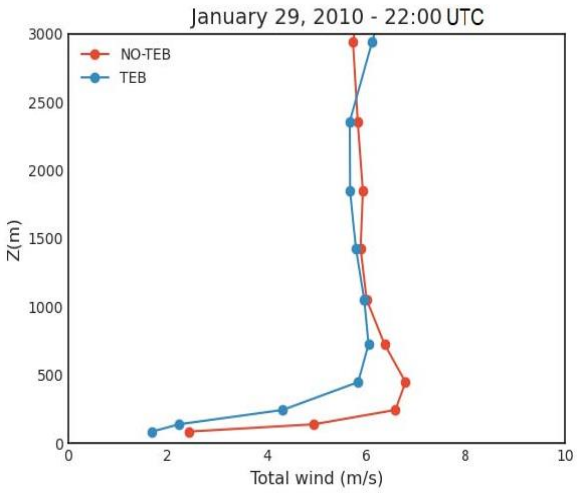

Fig. 20. Vertical profile of wind speed at night.

TEB scenario – can be associated with the wind shear (Fig. 20) with the occurrence of temperature inversion. Strong stability, especially in the NO-TEB scenario, prevents the mixing of the stable low layer with the warmer layer above. The higher value of TKE in the NO-TEB scenario can be observed at the tops of the inversion layer.

4.1.2 C2 – Spring case

Figure 21 shows the temporal changes of the vertical temperature structure near the surface for the spring case. After the sunrise (07:00 UTC), the convective activity is suppressed due to the existence of the inversion above. This happens in both scenarios but with a slightly stronger inversion in the TEB scenario. However, the inversion is very weak for both scenarios at this time of the day. So there is a shallow mixed layer with a depth of 100 m that starts to appear, and there is still a remnant of a nocturnal inversion which is very weak. There is a sharp increase in temperature, which leads to the dissipation of the inversion layer. It can be seen that at mid-day, the inversion was eliminated, and a convective mixed layer was formed. After the sunset, the surface radiation is reduced, temperature decreases sharply, surface cooling re-establishes, and radiative inversion occurs. The inversion is deeper (~200 m) and has higher strength (3°C) for the NO-TEB scenario than the TEB scenario, which is very weak. Inversion continues to exist after midnight for the NO-TEB scenario, which has even higher strength than for the TEB scenario, and the inversion continues to be very weak (1°C). Standard deviation is presented as error bars in the plots. There is a weak variability in the lower and upper altitudes during the day and night.

Figure 22 presents the cross-section of the temperature difference between the TEB and NO-TEB scenario on April 24, 2010. It can be seen that the urban surface is warmer than the no urban surface, and the temperature decreases with altitude. The atmosphere over the city area is warmer than the NO-TEB scenario, and it is warmer up to higher altitudes of more than 1000 m.

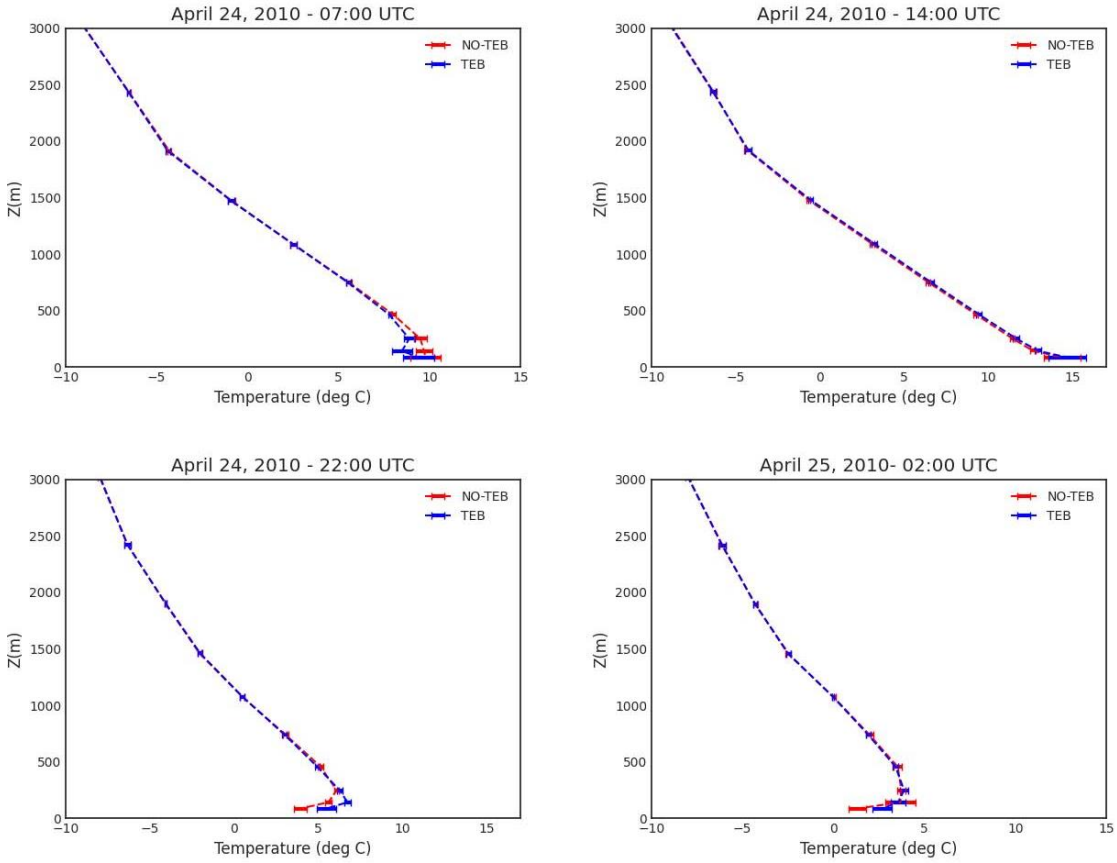

Fig. 21. Vertical profile of temperature on April 24, 2010, for NO-TEB and TEB scenarios. Error bars present the standard deviation.

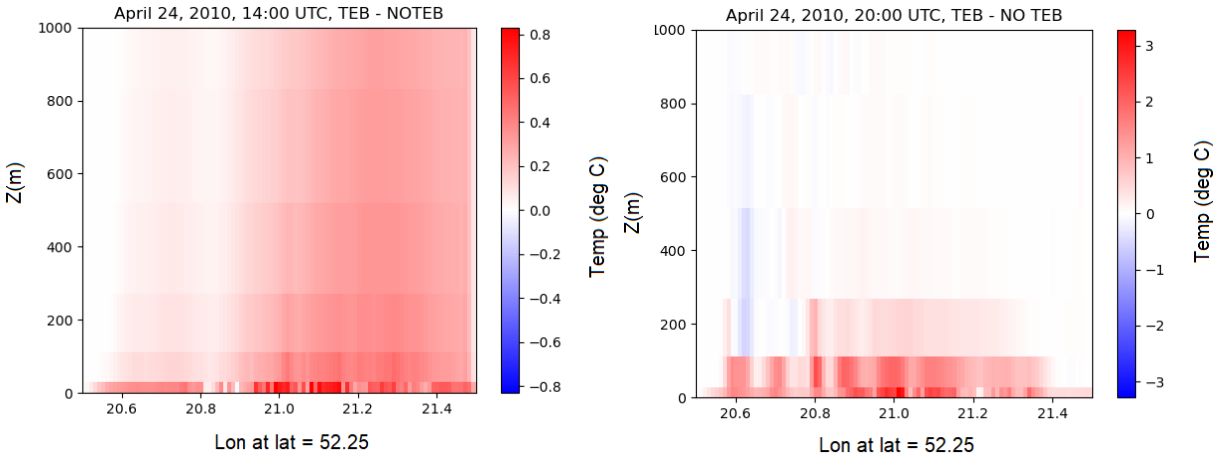

Fig. 22. Cross section of a temperature difference between TEB and NO-TEB scenario on April 24, 2010.

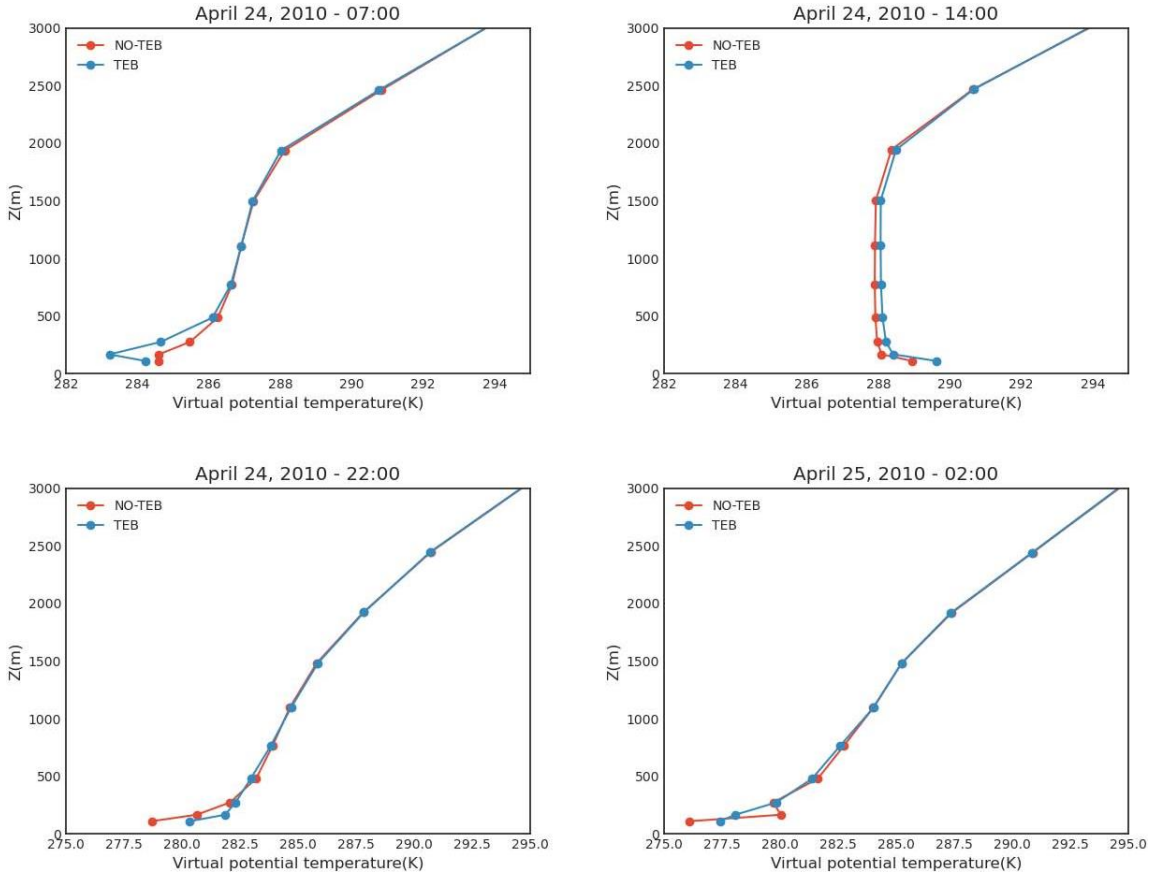

Fig. 23. Vertical profile of virtual potential temperature on April 24, 2010, for NO-TEB and TEB scenarios.

There is a significant difference in temperature between the TEB and NO-TEB scenarios at night. The temperature is significantly higher (3°C) in the urban scenario, particularly in the city centre. There is an inversion at night in both scenarios. However, it is more robust in the NO-TEB scenario than in the TEB scenario.

Figure 23 shows a stable boundary layer just after the sunrise on April 24 for the NO-TEB scenario. The warmer surface in the TEB scenario forms a shallow turbulent boundary layer at

a height of almost 100 m. However, in the NO-TEB scenario, the atmosphere is still stable. Later in the afternoon, when the residual air is entirely mixed into the growing boundary layer, surface heating causes the air near the surface to have a higher virtual temperature than the air just above it, so a temperature profile is superadiabatic. Potential temperature is uniform with height in both scenarios afternoon which shows the well mixed convective boundary layer. After sunset, the surface cools down, forming a stable boundary layer.

After sunrise, a vertical profile of specific humidity above the surface layer starts to form and gets deeper after midday (Fig. 24), which shows a very well-mixed convective layer during the day.

The cross-sections of the specific humidity show the differences in specific humidity between the NO-TEB and TEB scenarios at 14:00 and 22:00 in Fig. 25. The negative values of the TEB and NO-TEB difference indicate that the urban boundary layer is less humid in the NO-TEB scenario. The NO-TEB scenario remains more humid up to the top of the boundary layer at 14:00. At night, the NO-TEB scenario is significantly more humid than the TEB scenario near the surface and remains humid up to ~180 m. This difference is zero at higher altitudes.

On April 24, there was a sharp and rapid increase in temperature after sunrise, which is the source of turbulence. An increase in temperature before noon results in more thermals – current of air rising from the hot ground – which push the boundary layer upwards to the height of ~2500 m (Fig. 26). The increase in the thermals is due to the positive buoyancy, which is also

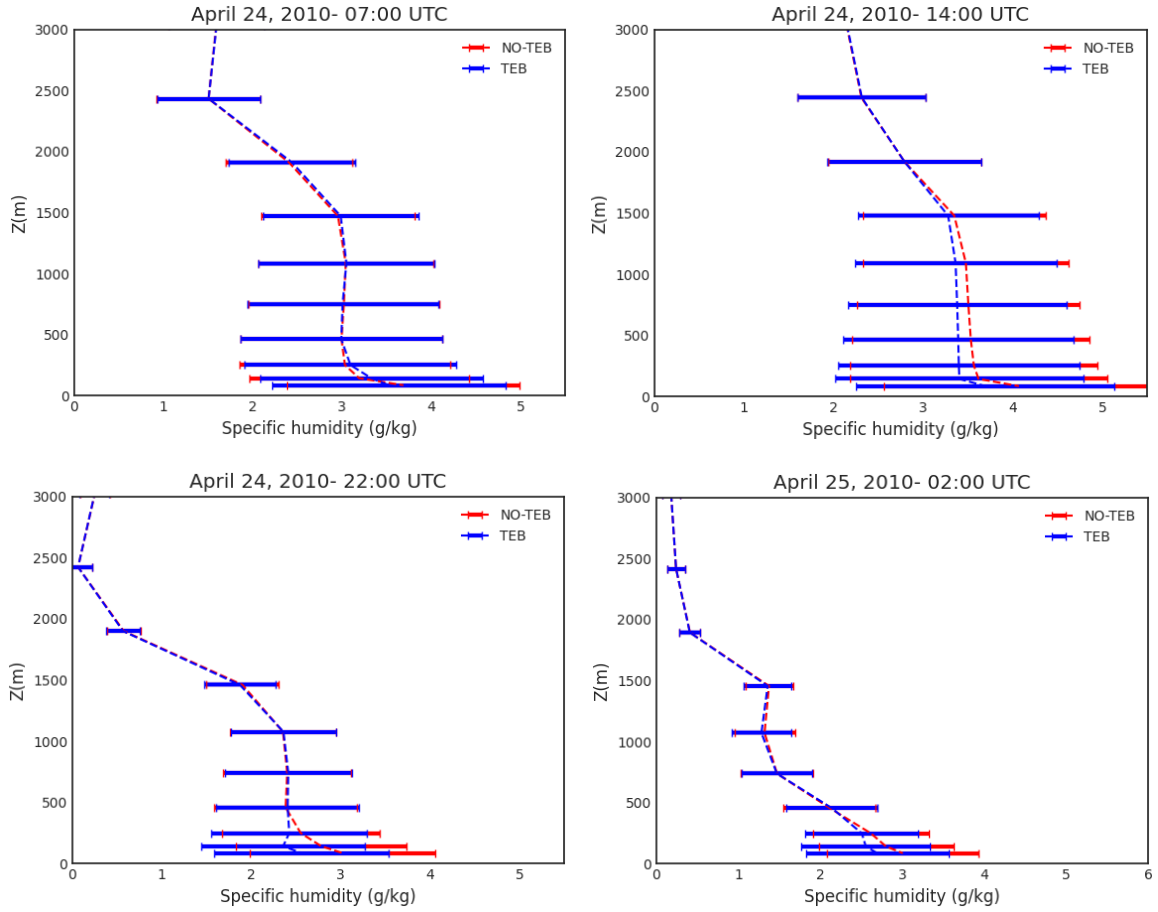

Fig. 24. Vertical profile of specific humidity on April 24, 2010, for NO-TEB and TEB scenarios. Error bars present the standard deviation.

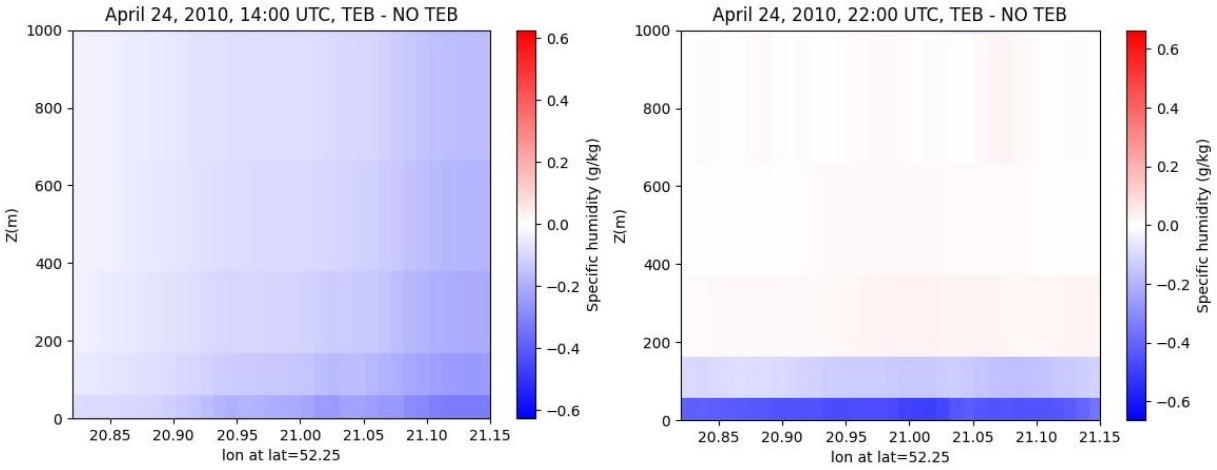

Fig. 25. Cross section of specific humidity difference between TEB and NO-TEB scenario on April 24, 2010.

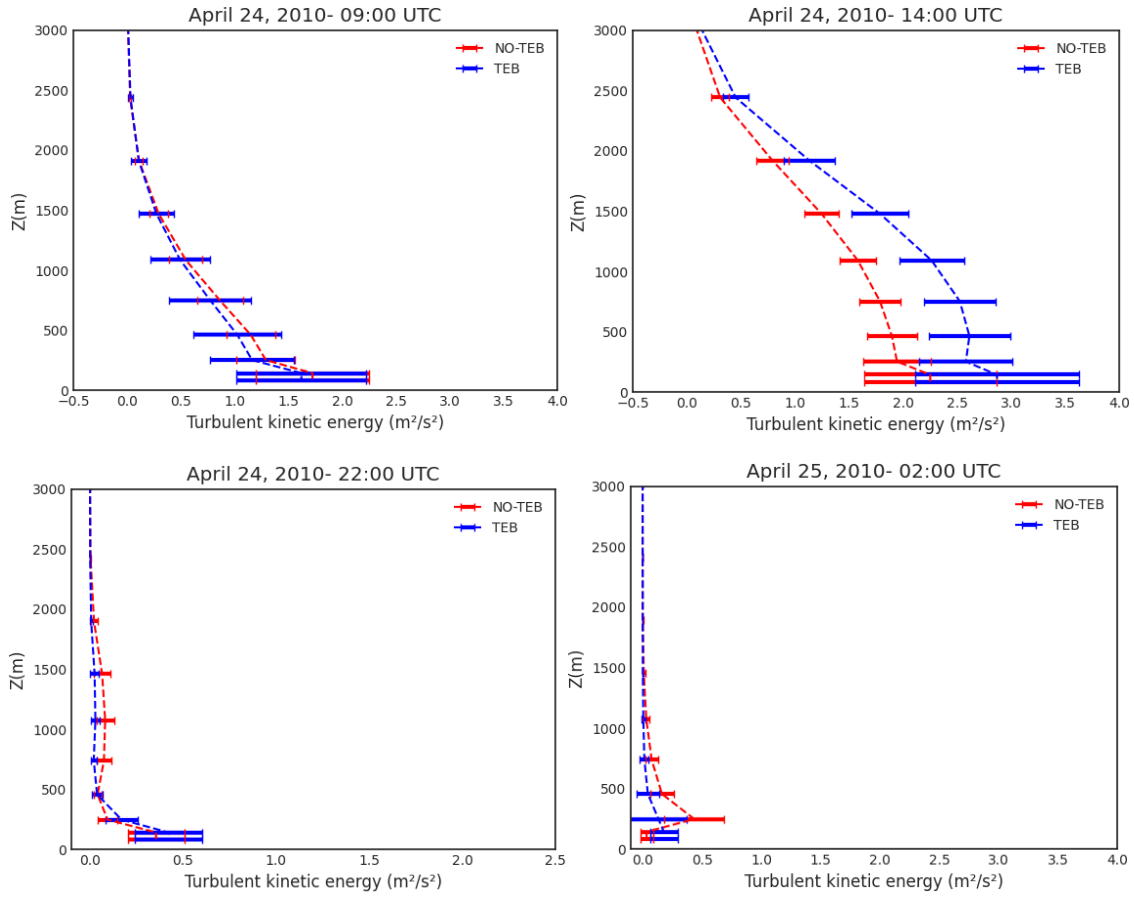

Fig. 26. Vertical profile of mean turbulent kinetic energy on April 24, 2010, for NO-TEB and TEB scenarios. Error bars present the standard deviation.

a driving force for the turbulence in BL and creates thermal kinetic energy. This energy is then transferred into different size eddies to the higher altitudes, responsible for the turbulent transport within the convective mixed layer. After sunset, the temperature drops, and the ground cools down; thus, the stability suppresses the TKE. The TKE dissipates rapidly near the surface and decreases rapidly with height. Thus, nocturnal BL is formed.

4.1.3 C3 – Late spring case

On June 6 (Fig. 27), after sunrise, the surface temperature began to rise due to the incoming solar radiation. Therefore, heat turbulence abrades the inversion layer formed at night, and the convective mixed layer is formed. During the day, both scenarios follow the same trend and the temperature decreases with height. After the sunset and at night, surface radiation declines. The temperature decreases slowly, so cooling and inversion are formed at ~100 m with high strength but low depth for the NO-TEB scenario. The inversion strength for the TEB scenario is lower due to the higher surface temperature. Error bars presented in the plots represent the standard deviation, which shows a weak variability in higher altitudes and lower altitudes during the day. There is a strong variability at night near the surface.

Figure 28 shows the cross-section of the temperature difference between the TEB and NO-TEB scenario on June 6, 2010. As in C1 and C2 cases, the urban scenario is warmer than the no urban scenario. It is warmer (1°C) over the city centre. Moreover, the temperature is higher in the TEB scenario at higher altitudes. The impact of the warmer surface is deeper because of the deep convective boundary layer. Therefore, an urban heat island is present within the urban area.

At night, the urban heat island does not fade away. The urban surface is warmer by almost 4°C in the city centre. The temperature is higher near the surface over the city centre and in higher altitudes up to the height of ~100 m (particularly over the city centre). Also, there is an inversion in both scenarios, which is stronger above the NO-TEB scenario up to the height of ~200 m. Thus, a very strong nocturnal urban heat island mainly over the centre of the city with

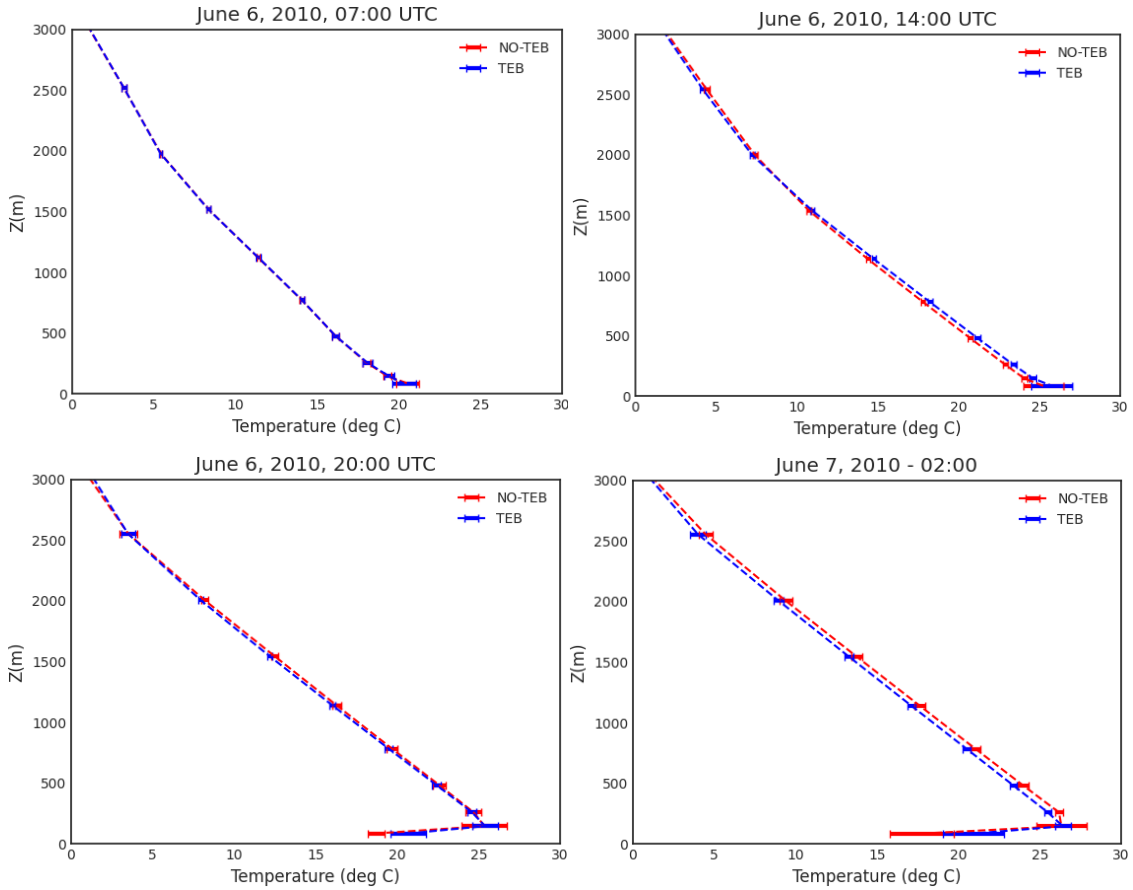

Fig. 27. Vertical profile of temperature on June 6, 2010, for NO-TEB and TEB scenarios. Error bars present the standard deviation.

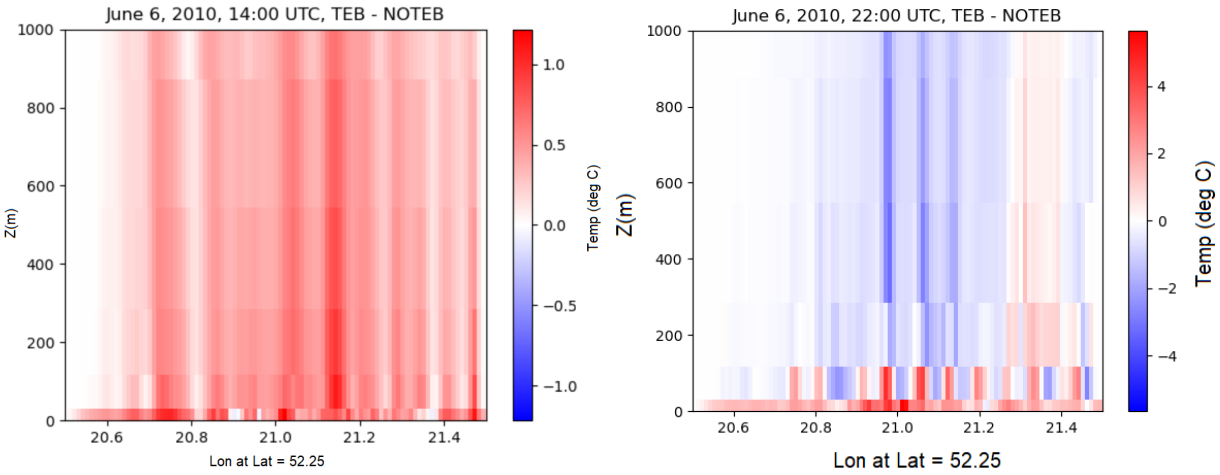

Fig. 28. Cross-section of temperature difference between TEB and NO-TEB scenario on June 6, 2010.

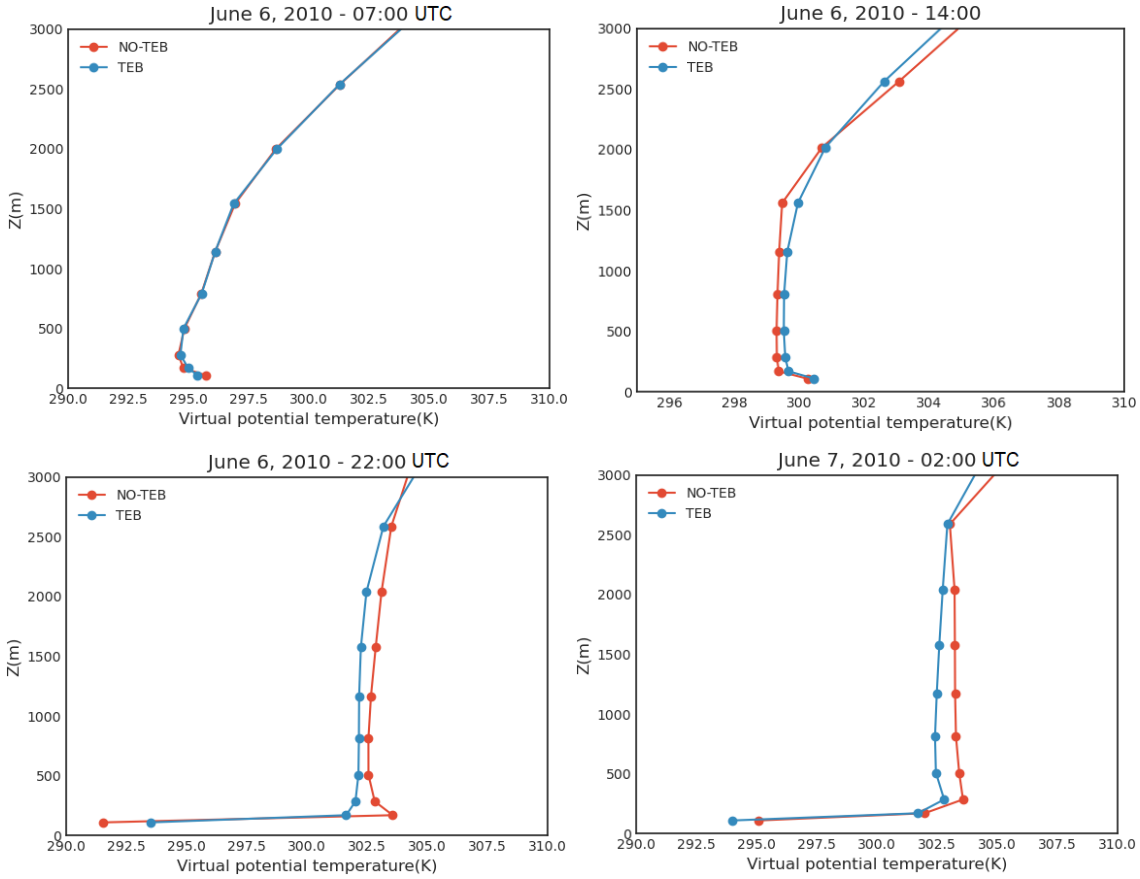

Fig. 29. Vertical profile of virtual potential temperature on June 6, 2010, for NO-TEB and TEB scenarios.

a more dense built-up area can be seen in the TEB scenario. For this reason, the inversion is weaker at night in the TEB scenario than in the NO-TEB scenario.

The morning profile (Fig. 29) is formed with a shallow mixed layer surmounted by the remnant nocturnal inversion. Continued turbulent heat convergence into the lowest atmosphere successively erodes the inversion layer until mid-morning, when it is eliminated. After that, the convectively-driven mixed layer can more readily extend up through the overlying air and creates an unstable layer which forms a uniform potential temperature with height (Fig. 29). After

the sunset, the surface radiation budget turns negative, and surface cooling re-establishes the radiation inversion in a shallow layer at the surface. A stable nocturnal boundary layer near the surface is formed, and the atmosphere stays neutral in the upper levels through the night.

Under the daytime condition, on a sunny and hot day on June 6, the atmospheric boundary layer is very efficient in vertically mixing the air. Thus, the vertical profile of the specific humidity is approximately constant with height (Fig. 30) in the well-mixed convective boundary

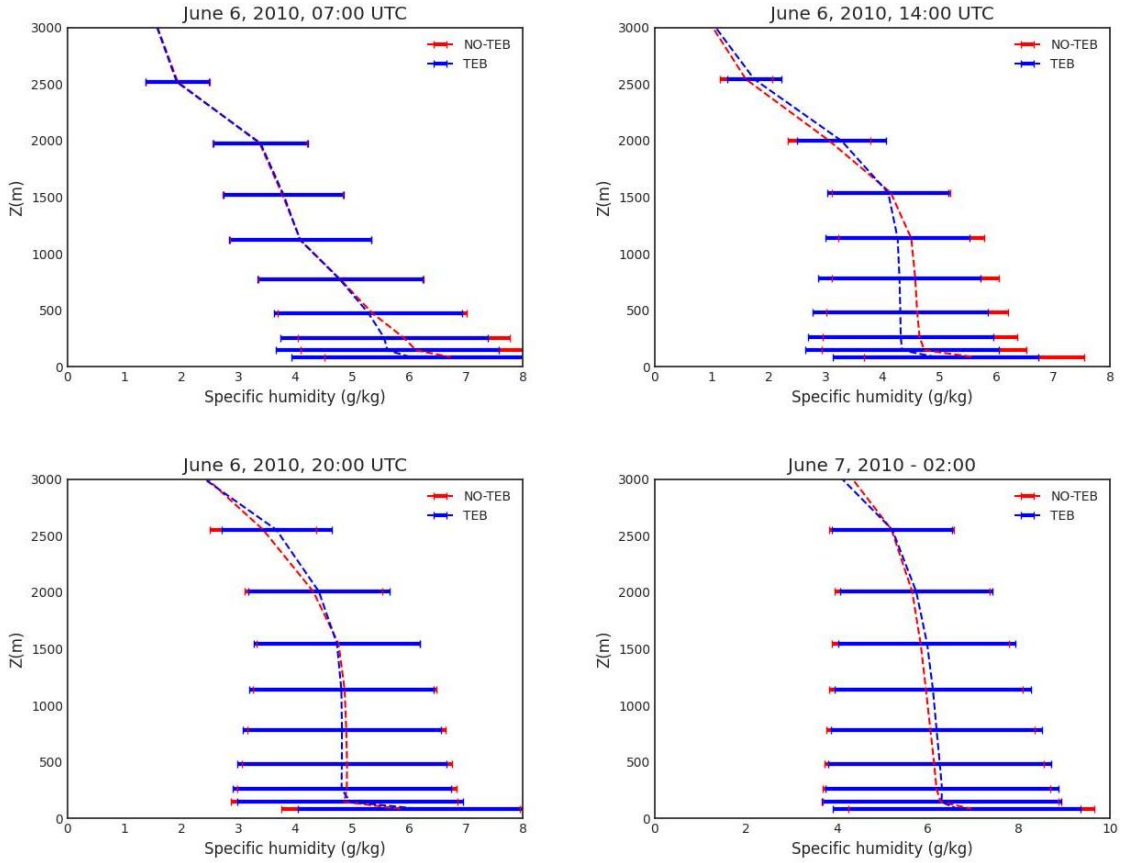

Fig. 30. Vertical profile of specific humidity on June 6, 2010, for NO-TEB and TEB scenarios. Error bars present the standard deviation.

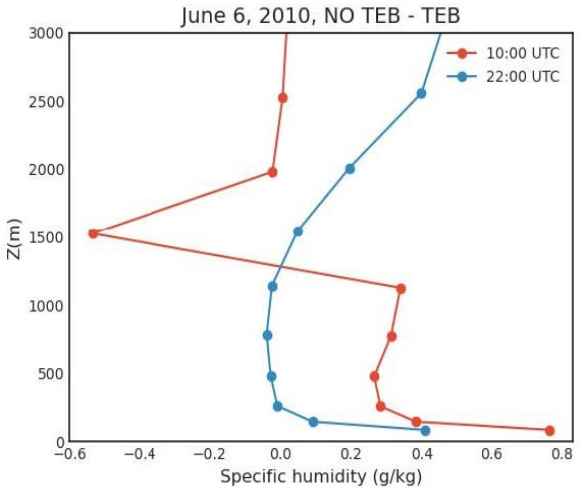

Fig. 31. Vertical profiles of specific humidity difference between the NO-TEB and TEB scenarios on June 6, 2010.

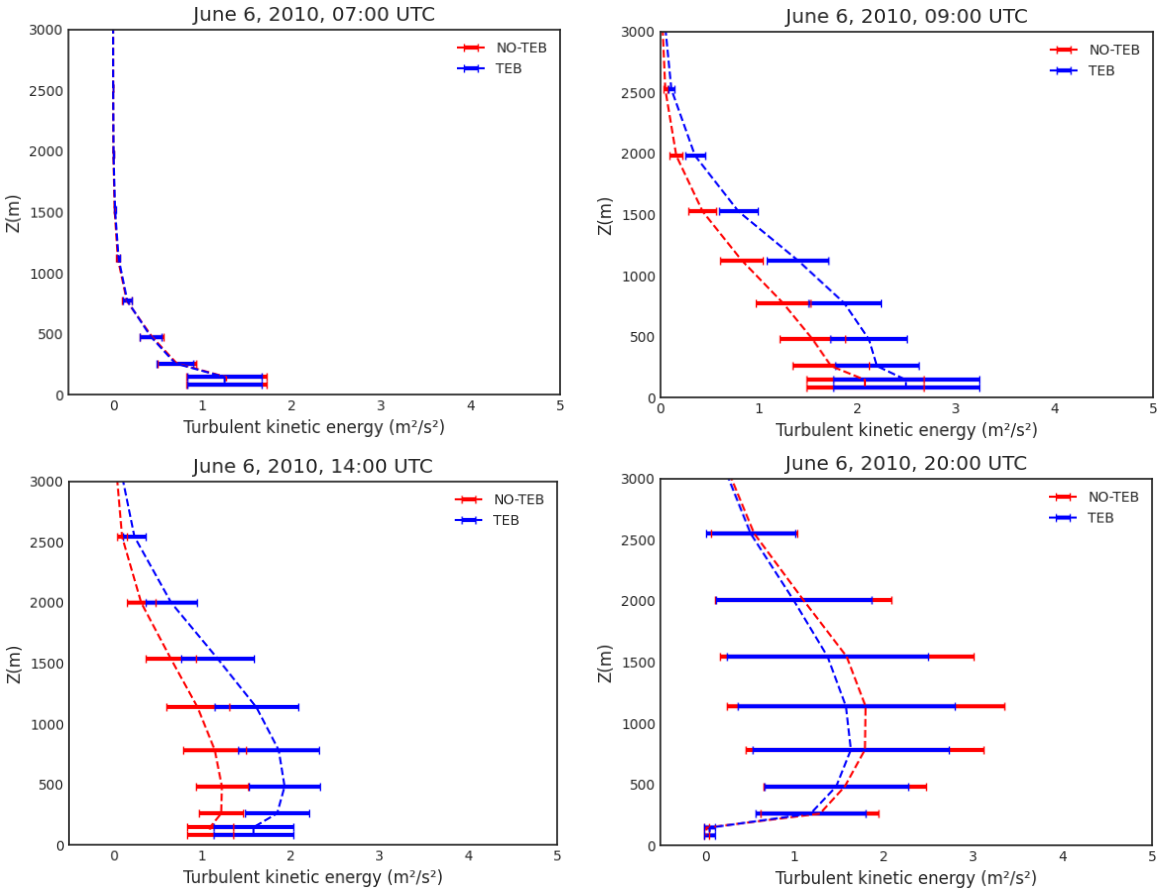

Fig. 32. Vertical profile of turbulent kinetic energy on June 6, 2010, for NO-TEB and TEB scenarios. Error bars present the standard deviation.

layer. Despite lower specific humidity for the TEB scenario near the surface, the vertical profile for both scenarios is constant with height.

The positive values of specific humidity differences in the morning and at night in Fig. 31 show that the urban atmosphere is less humid in the morning and at night. Based on the TKE profiles presented in Fig. 32, convective turbulence is generated after sunrise, under daytime conditions, with high temperature and humidity. Thermals are rising due to convection and push the convective BL upward to the height of ~2500 m for the TEB scenario. With the existence of a convective boundary layer on a sunny day, buoyancy is high near the ground and can contribute to the production of TKE over the ground. Later after sunset, since there is no sharp decrease in the temperature, the strong wind starts. This causes higher values of TKE at higher altitudes.

4.1.4 C4 – Summer case

Figure 33 illustrates the temperature profile in the boundary layer starting from early morning on July 23, 2010. As a result of warmer surfaces in the morning, caused by the absorbed solar radiation, a convective mixed layer is formed, so the temperature decreases with altitude. In the summer, days are longer than night, as in C4. Thus, the surface before the sunset is warmer than the surface after the sunrise, and no inversion occurs at night. There is a weak variability during the day and night in the boundary layer.

The cross-section of the temperature difference between TEB and NO-TEB scenario at 15:00 and 22:00 UTC, on July 23, 2010 (Fig. 34), shows that at 15:00 UTC, the temperature

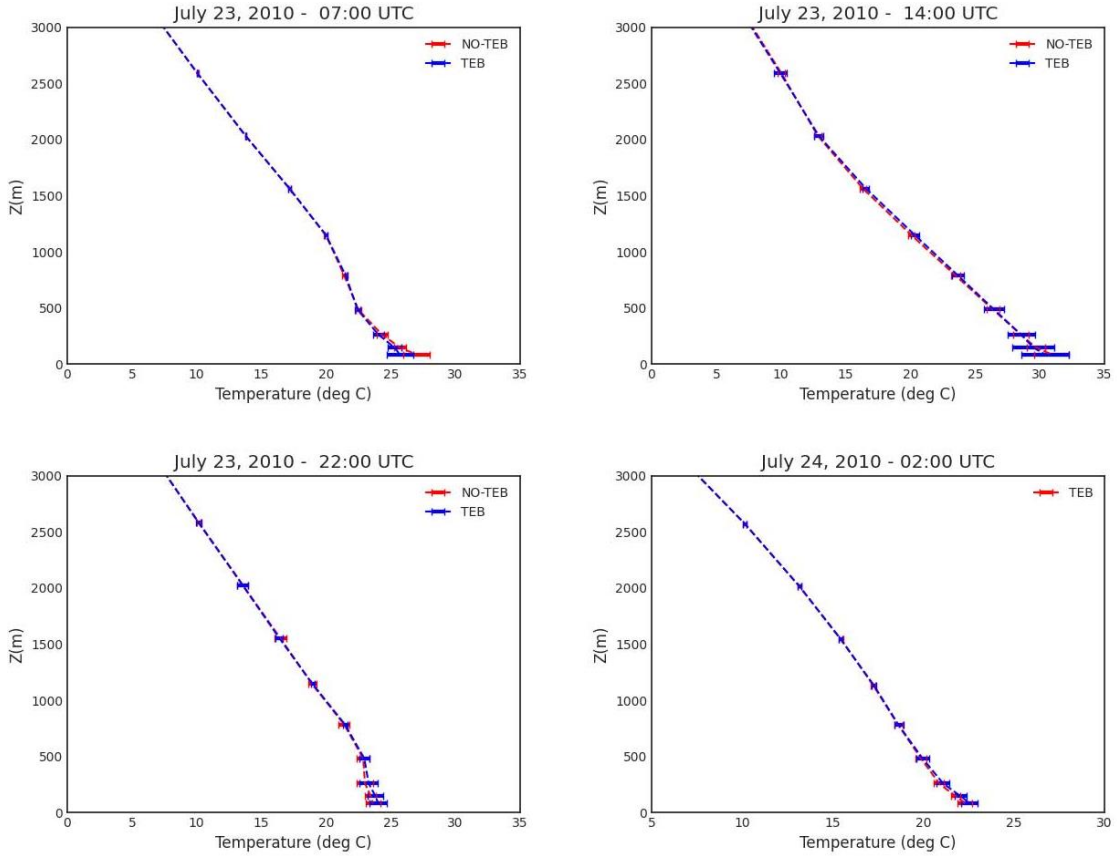

Fig. 33. Vertical profile of temperature on July 23, 2010, for NO-TEB and TEB scenarios. Error bars present the standard deviation.

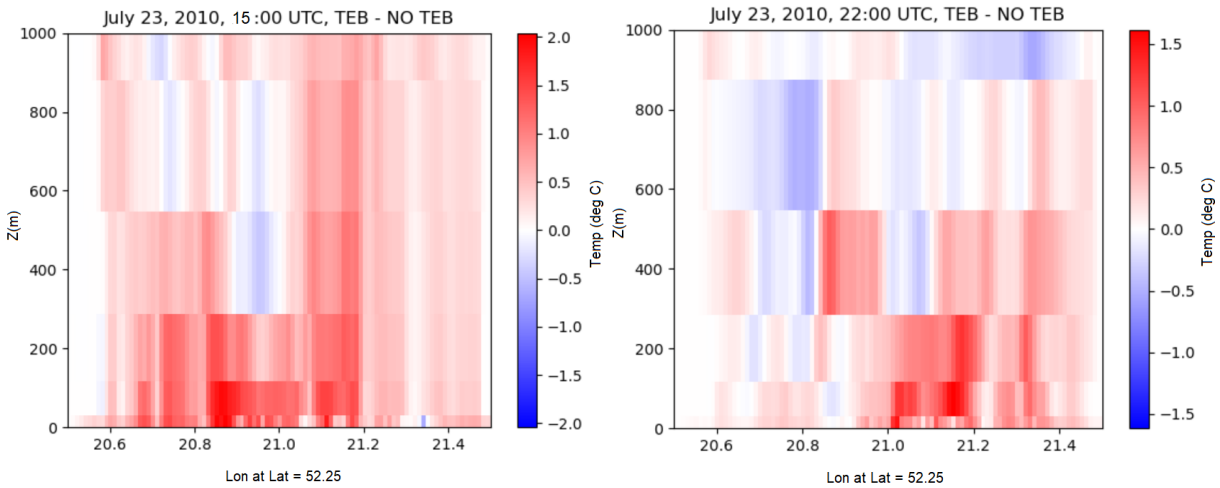

Fig. 34. Cross-section of a temperature difference between TEB and NO-TEB scenario on July 23, 2010.

over the urban surface is higher by almost 2°C than that over the no urban surface, mainly in the city centre and the analysis domain with the densely built-up area. In the TEB scenario, it stays warmer up to a height of 250 m in the boundary layer.

At night, after sunset, it can be seen that the urban heat island does not disappear. Even though the near-surface temperature difference is small, the TEB scenario is much warmer (almost 1.5°C) in higher altitudes than the NO-TEB scenario, mainly over the city centre and the area with mid-high buildings stays warmer up to a height of ~250 m.

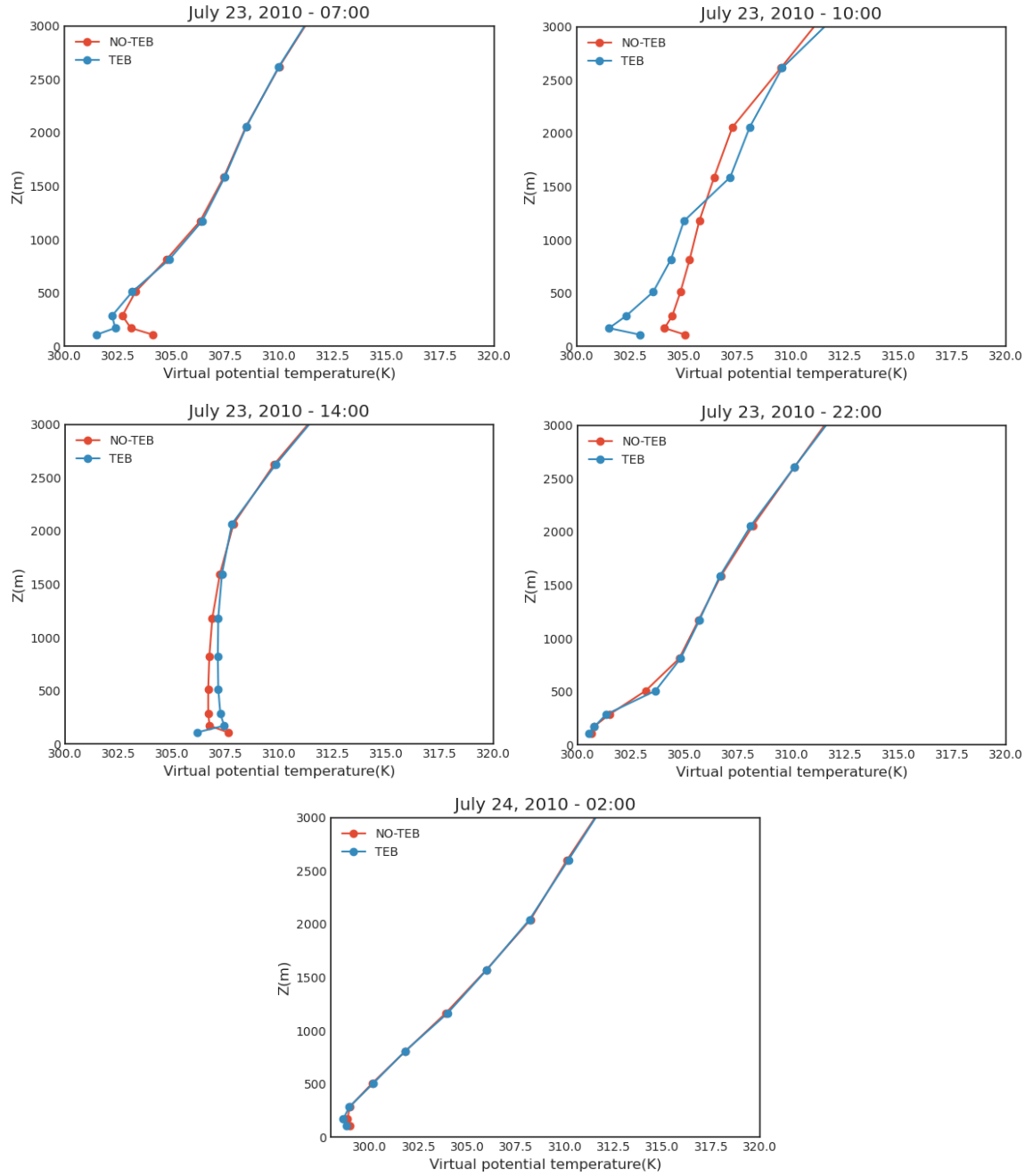

Fig. 35. Vertical profile of virtual potential temperature on July 23, 2010, for NO-TEB and TEB scenarios.

The virtual potential temperature profile shown in Fig. 35 was used to study the static stability of the BL. In the morning, the surface layer is unstable for both scenarios. This means that convective circulations, such as thermals, push the BL upwards and allow buoyant air to rise to the top of the unstable layer where the atmosphere is stable.

The instability continues to exist. In the afternoon, the stable surface layer is formed in the TEB scenario, but higher altitudes remain convective and unstable. On the other hand, the NO-TEB scenario remains unstable in the surface layer and higher altitudes. After the sunset, the boundary layer is stable.

Figure 37 shows the humidity inversion in the TEB scenario in the morning and the evening. Specific humidity is constant with height in midday, which indicates a well-mixed convective

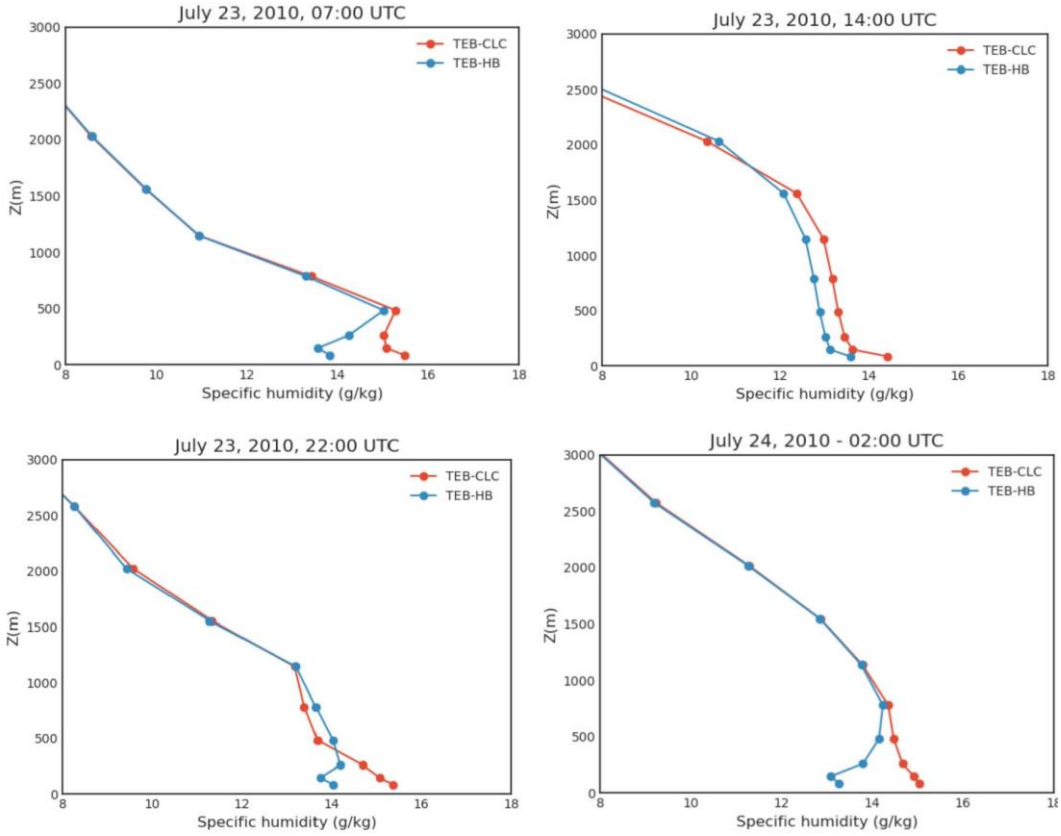

Fig. 36. Vertical profile of virtual potential temperature on July 23, 2010, for NO-TEB and TEB scenarios.

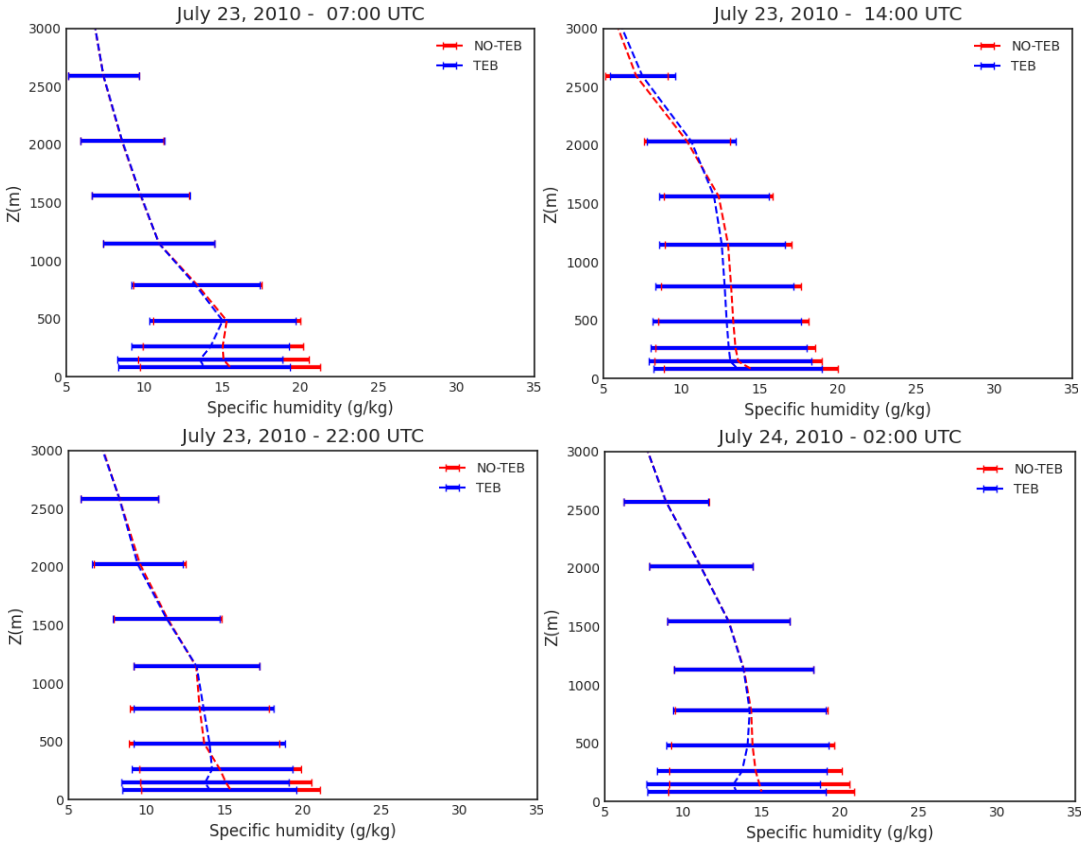

Fig. 37. Vertical profile of specific humidity on July 23, 2010, for NO-TEB and TEB scenarios. Error bars present the standard deviation.

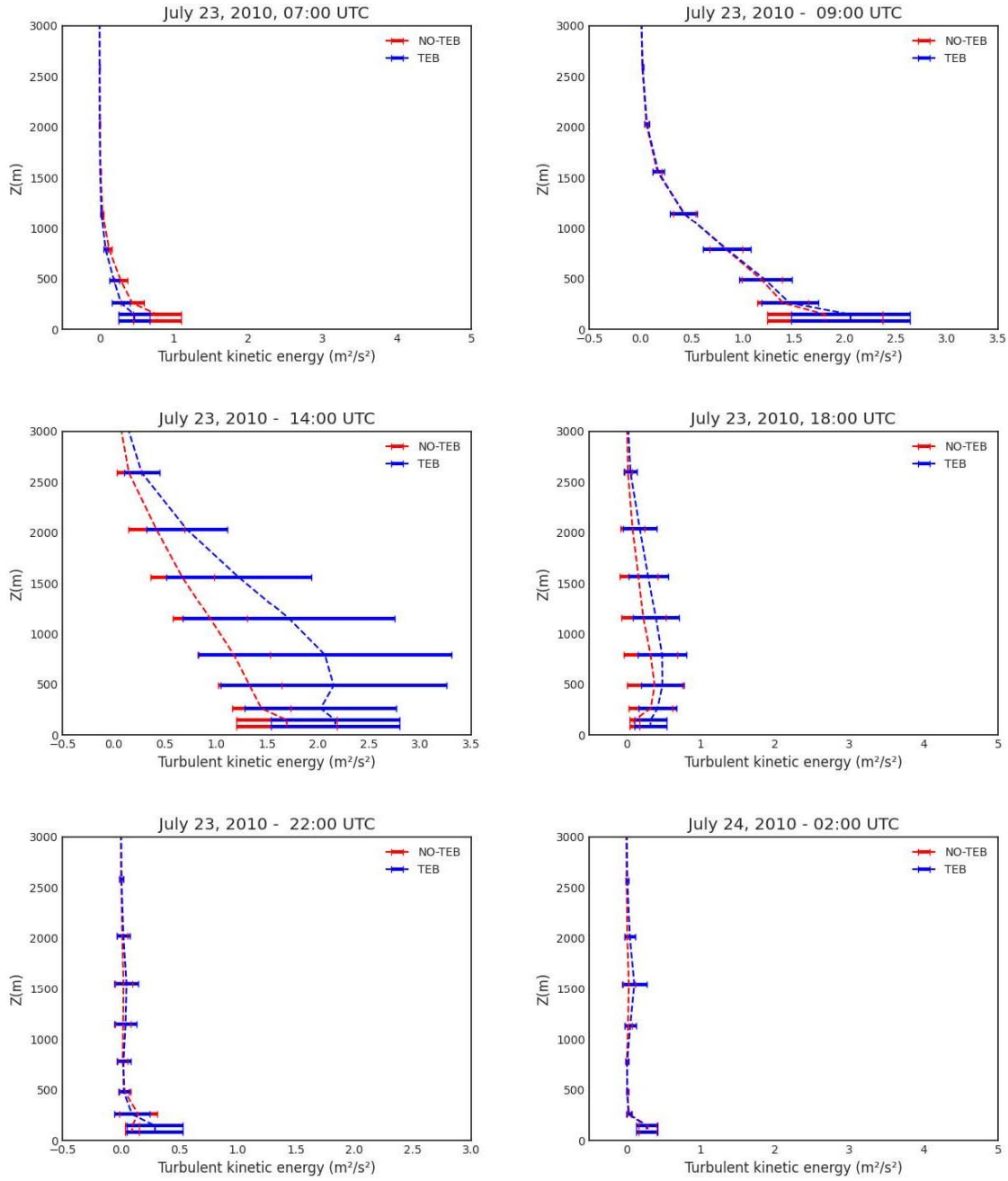

Fig. 38. Vertical profile of turbulent kinetic energy on July 23, 2010, for NO-TEB and TEB scenarios. Error bars present the standard deviation.

boundary layer, unlike the surface-based humidity inversion, which is more common in winter (Wypych and Bochenek 2018). According to Palarz and Celiński-Mysław (2020), elevated humidity inversion occurs in summer, which tends to begin at higher levels. Elevated humidity inversion can be observed in the morning and night (Fig. 36). Wypych and Bochenek (2018) discussed the correlation of the elevated humidity version in summer with a strong advection of warm and moist air masses. Thereby, the near-surface warm and humid air is mixed with the cold air above, a sudden temperature drop saturates the air, and the condensation occurs. As a result, the humidity inversion is deeper – it reaches an altitude of 800 m in the TEB scenario because of a warmer surface than in the NO-TEB scenario.

The variability of specific humidity in the boundary layer was presented with a standard deviation of values and shown as error bars in the vertical profiles (Fig. 37).

Profiles of turbulent kinetic energy on July 23 (Fig. 38) show the generation of convective turbulence after sunrise due to high temperature and humidity, which pushes BL upward and forms a deep turbulent layer till sunset. Thermal effects become increasingly dominant at higher altitudes. TKE for the TEB scenario is higher due to thermal factors of turbulence. The temperature in the TEB scenario is higher than in the NO-TEB scenario. After sunset, the surface is still warmer in the TEB scenario, which leads to a very shallow turbulent surface layer in the TEB scenario, but in the NO-TEB scenario, the TKE is suppressed, and a stable nocturnal boundary layer is formed.

4.2 Sensitivity analysis

Rapid changes of land-use/land-cover result from human activities having a profound impact on nature followed by significant consequences (Rimal et al. 2018), especially on climate (Li et al. 2018). Thus, studying the impacts of anthropogenic changes in land-use/land-cover become an important issue to be explored. According to the latest CORINE Land Cover dataset for Poland in 2018, there was a 0.1% decrease in the forest areas and a 0.1% increase in urban land cover compared to 2012. This section will present the sensitivity of meteorological parameters to the changes of urban surface and the magnitude of the anthropogenic heat flux. The variability of each parameter is shown with standard deviation as error bars on the temporal profiles.

4.2.1 Air temperature

Diurnal temperature changes for the urban area are very different from the rural area. Warming and cooling rates are generally smaller in urban regions. To detect the influence of urbanisation and built-up area, and determine the urban heat island (UHI) intensity, the temperature difference between the TEB scenario (TEB-CLC) and natural land cover scenario (TEB-VEG), as well as the difference between the city covered with mid-high buildings scenario (TEB-HB) and natural land cover scenario (TEB-VEG) was calculated. Maximum values of the temperature difference between each scenario are presented in Table 9. Considering two built-up area scenarios, TEB-CLC and TEB-HB, they have different features since the percentage of higher buildings is different in these scenarios. Therefore, the UHI intensities are studied separately.

Table 9

Maximum temperature difference
between TEB-CLC and TEB-VEG and TEB-HB and TEB-VEG

	TEB-CLC – TEB-VEG		TEB-HB – TEB-VEG	
	Day	Night	Day	Night
C1 – Winter	0.83	1.27	3.09	4.97
C2 – Spring	0.91	1.49	1.41	2.09
C3 – Late spring	1.12	1.77	2.49	3.48
C4 – Summer	0.89	0.75	1.53	1.50

Only 0.12% of the land cover of the whole study domain in the TEB-CLC scenario – which resembles the city of Warsaw's land cover – is covered with high and mid-high buildings. The buildings are primarily located in the city centre. The rest of the city is mainly covered with

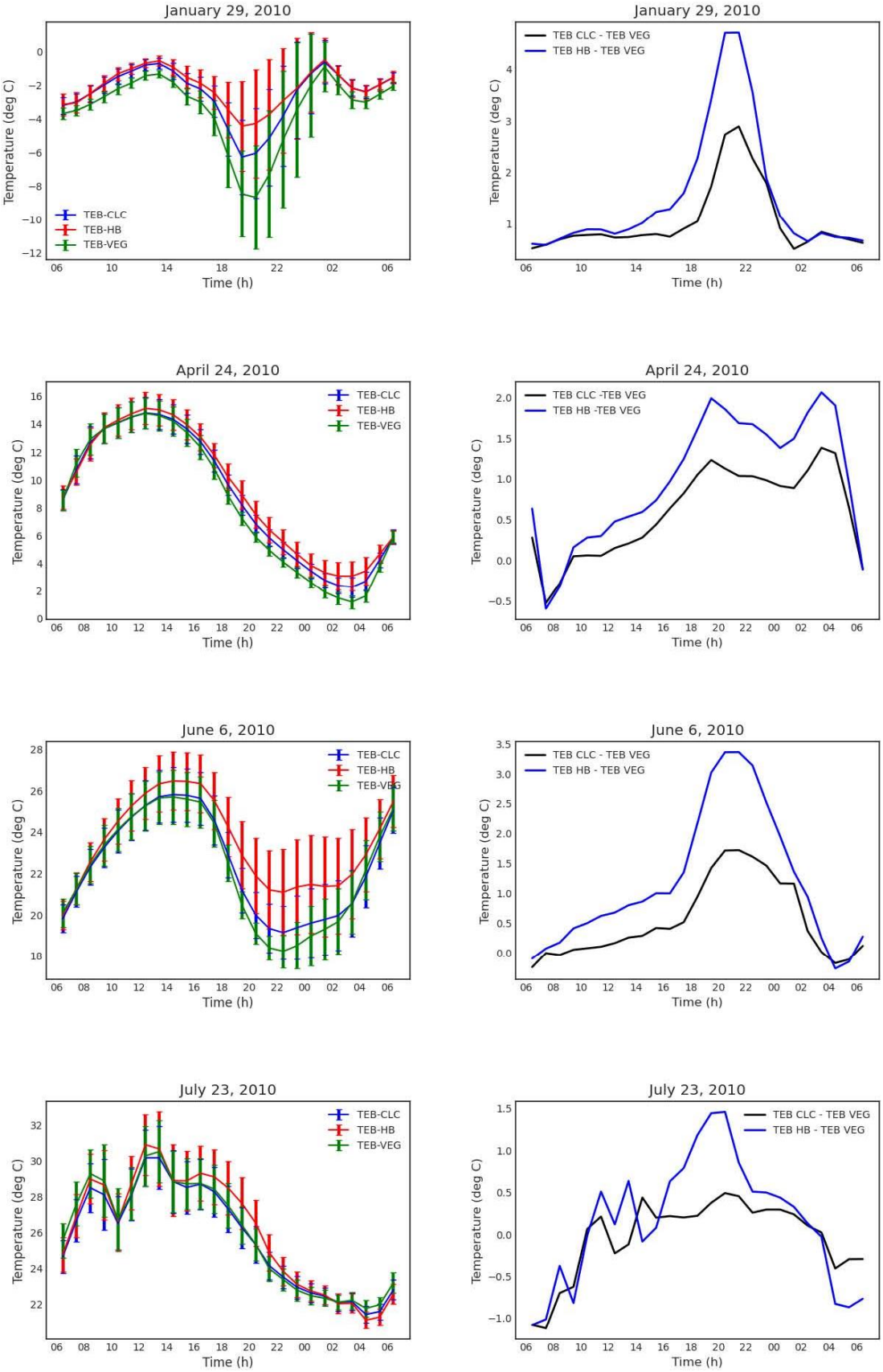

Fig. 39. Hourly average course of temperature for three sensitivity scenarios (TEB-CLC, TEB-HB, TEB-VEG) for 4 selected cases and within the calculated averaged grid in 2010 (left panels), the temperature difference between TEB-CLC and TEB-VEG, and TEB-HB and TEB-VEG (right panels).

low sparse buildings. ΔT_{max} is the highest in the late spring, and it is even higher at night for the TEB-CLC scenario. In C2 and C3 cases, Warsaw was under stable weather conditions. This means that Warsaw was under the influence of the same air mass for over 24 hours.

Therefore, the positive values of ΔT_{max} at night are due mainly to urbanisation that causes a nocturnal UHI. The results show an almost similar course of UHI intensity for C2 and C3. There is a fast growth of the thermal contrast, which starts in the late afternoon and continues approximately until midnight. The UHI remains constant throughout the rest of the night in C2.

The UHI's decay starts just after sunrise and is very rapid in the early morning. Due to faster changes of ΔT_{max} after sunrise than before sunset, the nocturnal UHI intensity is asymmetric (Fortuniak et al. 2006).

In the TEB-HB scenario, ~11% of the whole study domain is covered with high and mid-high buildings, which made ΔT_{max} stronger. There is a nocturnal UHI in C2 and C3. However, C3 with the higher temperature throughout the day shows stronger nocturnal UHI intensity than C2. Furthermore, as shown in Fig. 43, specific humidity in the city, especially over the surface covered mostly with high and mid-high buildings (TEB-HB), is lower than the natural land cover scenario (TEB-VEG) by almost 19% for C3, which yields the highest UHI intensity. It can be concluded that the UHI intensity caused by urbanisation is the greatest in the dry season.

There was considerable nocturnal UHI intensity on January 29 (Fig. 39). On January 29, the centre of Poland was under the influence of a polar air mass. High values of ΔT_{max} can amplify the UHI intensity after the advection of cold polar air due to the high thermal inertia of the town and the significant anthropogenic heat flux (Fortuniak et al. 2006). Increasing the density of the high and mid-high buildings (TEB-HB) injects more anthropogenic heat flux from the heating households and yields significantly higher nocturnal UHI intensity (4.97°C).

Low-intensity UHI takes place on July 23 (Fig. 39). ΔT_{max} is higher in the daytime in the late afternoon, and it stays constant till sunrise in the TEB-CLC scenario. In addition, there are high negative values of ΔT_{max} during the day before noon. The significant thermal differences in the daytime and strong negative differences at midday are usually formed due to passing fronts (Fortuniak et al. 2006). The centre of Poland on July 23 was under the influence of atmospheric fronts and was extremely humid due to the exposure to the humid tropical air mass. Adding more high and mid-high buildings to the urban area (TEB-HB) strengthens the UHI intensity with the maximum ΔT_{max} right after sunset. Based on Fig. 43, the city surface with a higher number of high buildings results in a significant reduction in humidity. Also, July 23 was extremely hot. Therefore, despite the low dependency of UHI intensity on urbanisation due to the atmospheric fronts, adding more built-ups to the city environment exacerbates UHI intensity, especially in the summer.

4.2.1.1 Surface temperature

There is a single temperature at the interface of every surface with a unique surface energy balance and the air, which is surface temperature. This temperature is a boundary in the temperature gradients that generate an upward sensible heat flux and similarly downward sensible heat flux (Oke et al. 2017). The temporal variability of surface temperature in the cities is much higher than the air temperature. There are large intra-urban differences in surface temperature (Oke et al. 2017). Figure 40 presents diurnal surface temperature changes for three scenarios in C1, C2, C3, and C4 cases.

As shown in Table 10, the highest surface temperature values are for the TEB-HB scenario and the lowest for the TEB-VEG. For instance, the spatial distribution of surface temperature for the spring case (C2) is shown in Fig. 41. Natural land cover has a significant impact on surface temperature. Replacing the urban surface with the green surface decreased the surface temperature by 1.1°C compared to the TEB-CLC and 1.74°C compared to TEB-HB in C2.

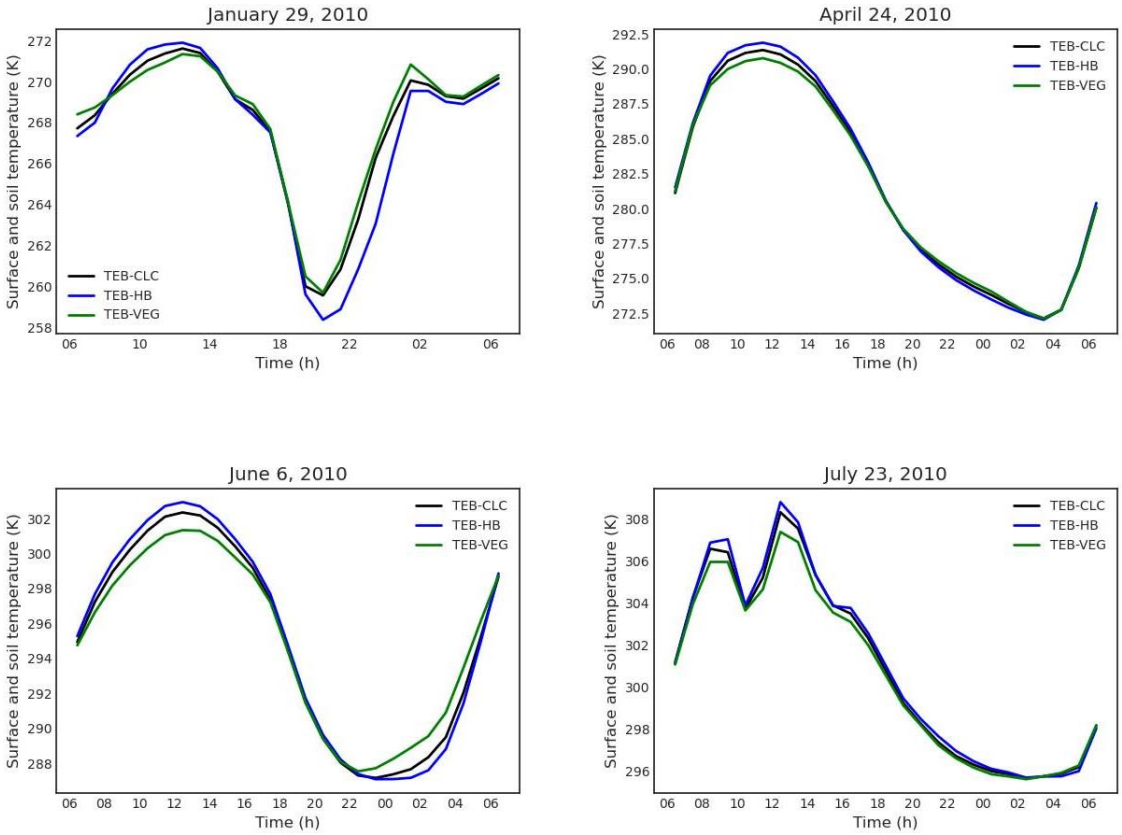

Fig. 40. Hourly average course of surface temperature for three sensitivity scenarios (TEB-CLC, TEB-HB, TEB-VEG) for four selected days in Warsaw, 2010.

Table 10

Maximum surface and soil temperature [°C] for TEB-CLC, TEB-HB, and TEB-VEG scenarios for four selected cases

	TEB-CLC	TEB-HB	TEB-VEG
C1	–1.49	–1.19	–1.69
C2	18.22	18.74	17.64
C3	29.23	29.81	28.23
C4	35.46	35.99	34.49

Figure 41 shows that surface temperature in the centre of the domain of the TEB-VEG model is much less than the TEB model with the urban land cover. The surface temperature decrease in the natural land cover scenario (TEB-VEG) is even higher for the late spring (C3) and summer (C4) cases. Figure 43 illustrates the surface temperature distribution over the domain for two TEB-HB and TEB-VEG scenarios in C3 and C4 cases. Substitution of land cover with natural cover reduces the temperature by 2.5°C in C3 and 2.3°C in C4 compared to the surface covered with mid-high buildings.

The lower surface temperature in the centre of the city for the TEB-VEG for both C3 and C4 cases is shown in Fig. 42. Almost 11% of the domain is covered with the mid-high buildings in the TEB-HB scenario and is in the centre of the domain and was replaced by the natural cover in the TEB-VEG scenario.

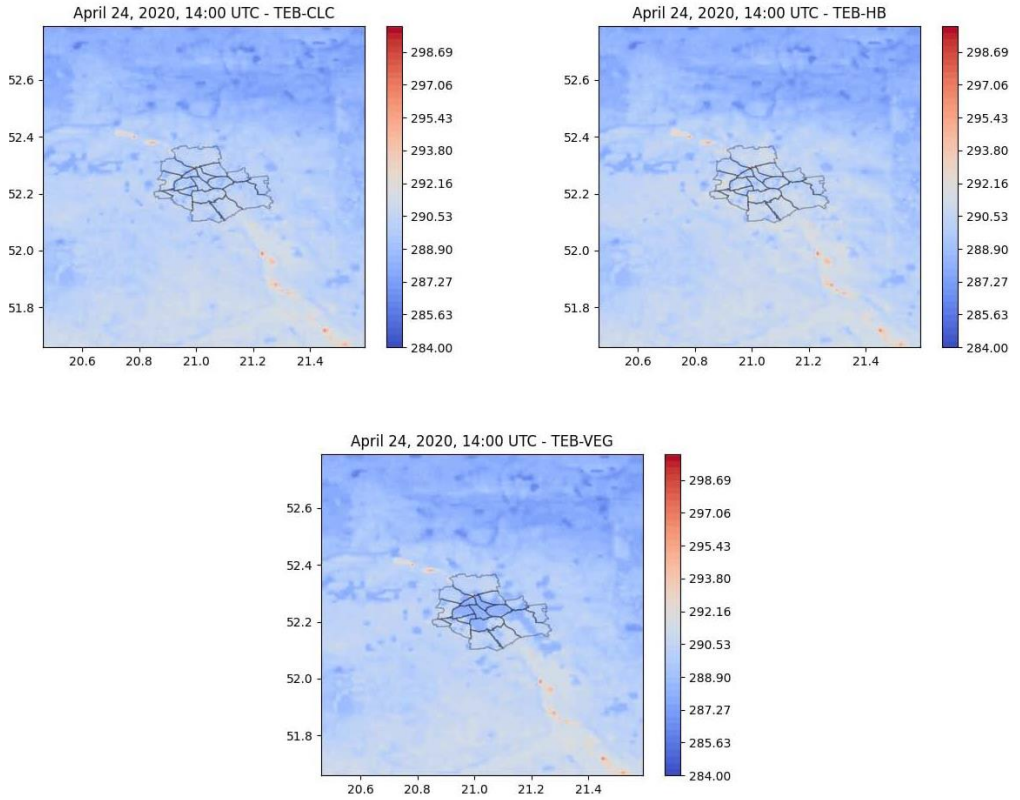

Fig. 41. Spatial distribution of surface and soil temperature for TEB-CLC, TEB-HB, and TEB-VEG on April 24, 2010, at 14:00 UTC. The contour lines in the plots present the administrative borders of Warsaw city.

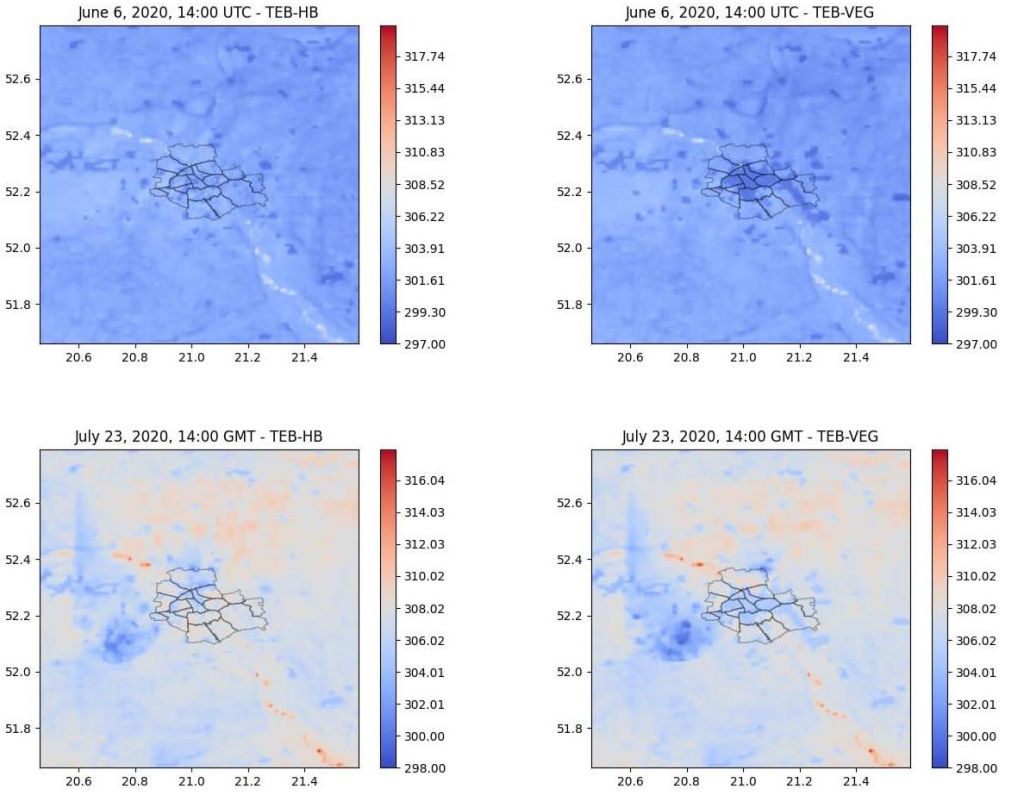

Fig. 42. Spatial distribution of surface and soil temperature TEB-HB (left panel) and TEB-VEG (right panel) in C3 and C4 at 14:00 UTC. The contour lines in the plots present the administrative borders of Warsaw city.

Dry surfaces with less evaporating water have a higher surface temperature. On the other hand, surfaces with higher water content like soils, lawns, and tree leaves have lower surface temperature during the day due to evaporative cooling and lower diurnal temperature range (Oke 1988). In addition, surfaces with lower albedo have a higher surface temperature. For instance, in C3, the albedo is lower in TEB-HB by 32% compared to TEB-VEG, which results in higher surface temperature in the scenarios with the urban surface. In the urban areas, during the daytime, the surface temperature of all surfaces is higher than the air temperature. However, the surface temperature is close to the air temperature for the vegetation. On the other hand, at night, the surface temperature of the roofs in the urban area is lower than the air temperature, but still the same for the natural covers (Oke et al. 2017).

4.2.2 Specific humidity

As a general rule, the water content of the urban atmosphere is low, especially in the daytime, due to lower evaporation rates compared to rural areas due to a mainly smaller fraction of vegetative cover in urban areas (Oke 1988). Thus, this can be observed for all selected cases, as shown in Fig. 43. At night in winter, we can see an urban moisture excess (Fig. 43). The positive values of the differences in the vertical profile of specific humidity in the morning and at night show that the urban boundary layer is more humid than the NO-TEB scenario. The reason can be the significant input of moisture from combustion sources.

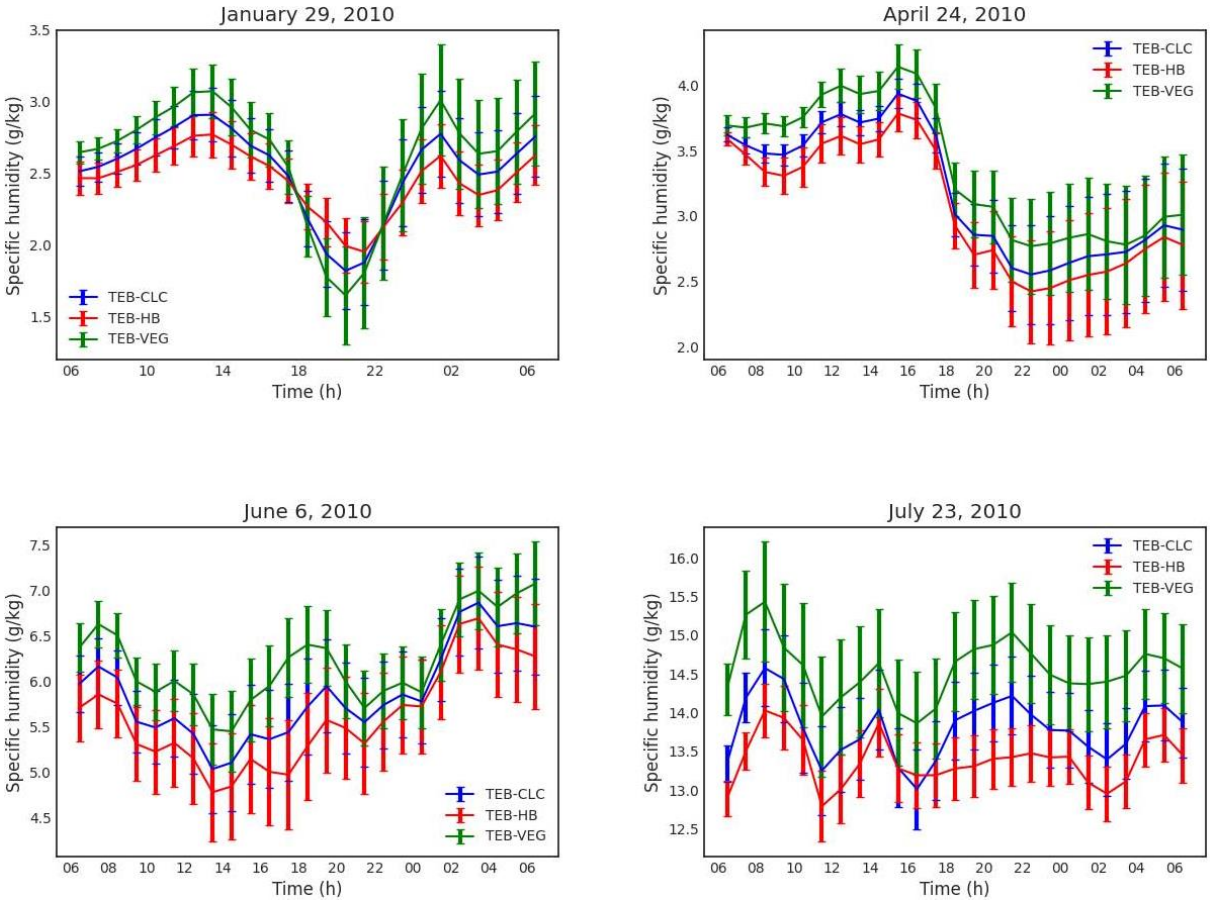

Fig. 43. Hourly average course of specific humidity for three sensitivity scenarios (TEB-CLC, TEB-HB, TEB-VEG) for four selected days in Warsaw, 2010.

84% of coal consumption is by the residential sector in Poland (Stala-Szlugaj 2016), and household heating is mainly from coal. Also, 80% of heating systems in Poland are inefficient (Stala-Szlugaj 2016). Water vapour is a large component of the flue gases released from coal-fired power and heat-cogeneration plants. The results show that the city is drier by day and moister at night in C1 (Table 11). The decrease in the specific humidity at night can be due to dew's formation, which depletes the moisture in the lowest layers, and specific humidity would decrease. Also, dewfall can contribute to moisture excess in the urban atmosphere because it removes less moisture from the lower urban atmosphere.

Table 11

Maximum specific humidity [g/kg] in winter case, January 29, for TEB-CLC, TEB-HB, and TEB-VEG scenarios

	Specific humidity at night [g/kg]	Specific humidity by day [g/kg]
TEB-CLC	1.88	2.93
TEB-HB	2.03	2.74
TEB-VEG	1.73	3.15

In the morning hours, the evapotranspiration of plant water into a moderately unstable atmosphere adds moisture to the lower layers, and the humidity increases quite sharply above the surface (Oke 2002). Unlike the fact that the humidity should increase at night, the specific humidity for the C1 case is decreasing in the late afternoon (Fig. 43). In this case, the downward transport of water vapour as dewfall can also be the reason, which means the water is removed from the lowest part of the atmosphere and causes a drop in the surface layer humidity.

For the late spring case, June 6, the specific humidity is high after sunrise, but the humidity drops during the day as the temperature rises and reaches the minimum value in the early afternoon. It results from convective activity penetrating to such heights in the boundary layer that the water vapour concentration becomes diluted by mixing with descending masses of drier air from above (Oke 2002). After sunset, surface cooling happens, and a stable boundary layer develops. As a result, the water vapour transport to the higher layers is suppressed. Therefore, moisture converges into the lowest layers, and the maximum humidity is observed. The minimum difference of specific humidity between TEB-HB and TEB-VEG scenarios, equal to –0.05, occurs at night, and the maximum difference, equal to –1.62, takes place by the day. The urban evaporation rate is weaker, and the convective mixing is higher during the daytime in the city. Thus, the specific humidity in a city is much lower than non-urban areas.

In the summer case, July 23, the maximum difference in the specific humidity between TEB-HB and TEB-VEG scenarios is –1.61 g/kg, higher at night than in the daytime, when it is –1.05 g/kg. This means the specific humidity for the urban surface covered with high buildings is by 12% lower than for the natural land cover.

The temporal variability of specific humidity (Fig. 43) is different for each scenario. Figure 44 shows the spatial distribution of specific humidity and wind for January 20 at 18:00 UTC. It can be seen that around 18:00 UTC there is an advection of dryer air to the domain, which causes the drop in the humidity.

Having the spatial distribution of specific humidity and wind for April 24 at 18:00 UTC(Fig. 45), it can be seen that around 18:00 UTC, there is a pronounced difference in humidity between two air masses which could explain the change from 17:00 UTC to 20:00 UTC (with the wind being aligned across).

There were no remarkable changes of specific humidity on July 23.

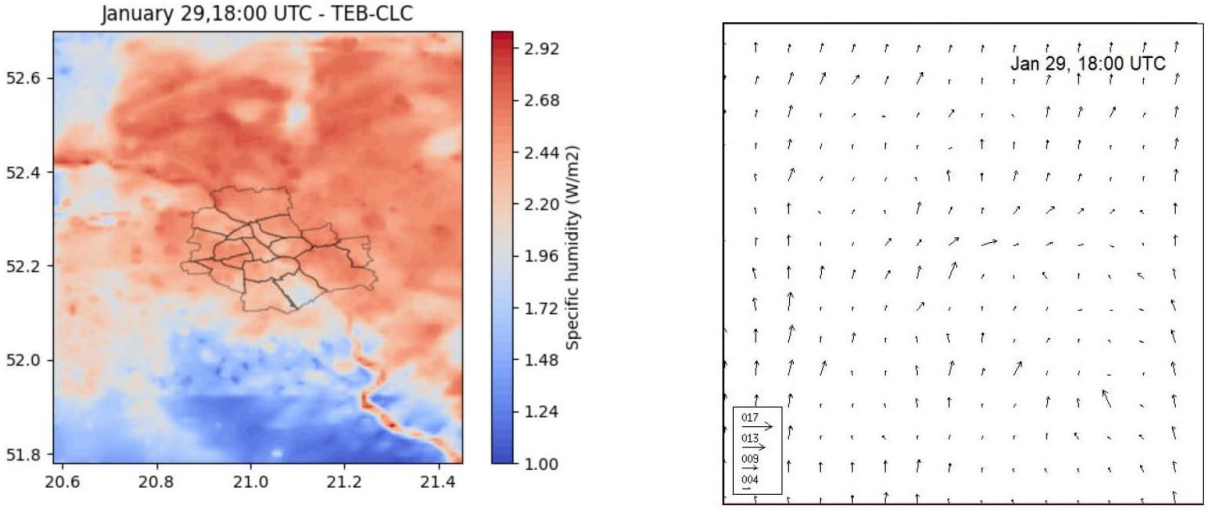

Fig. 44. Spatial distribution of specific humidity (left panel), wind speed and direction (right panel) on January 29, 2010, at 18:00 UTC. The contour lines in the plots present the administrative borders of Warsaw city.

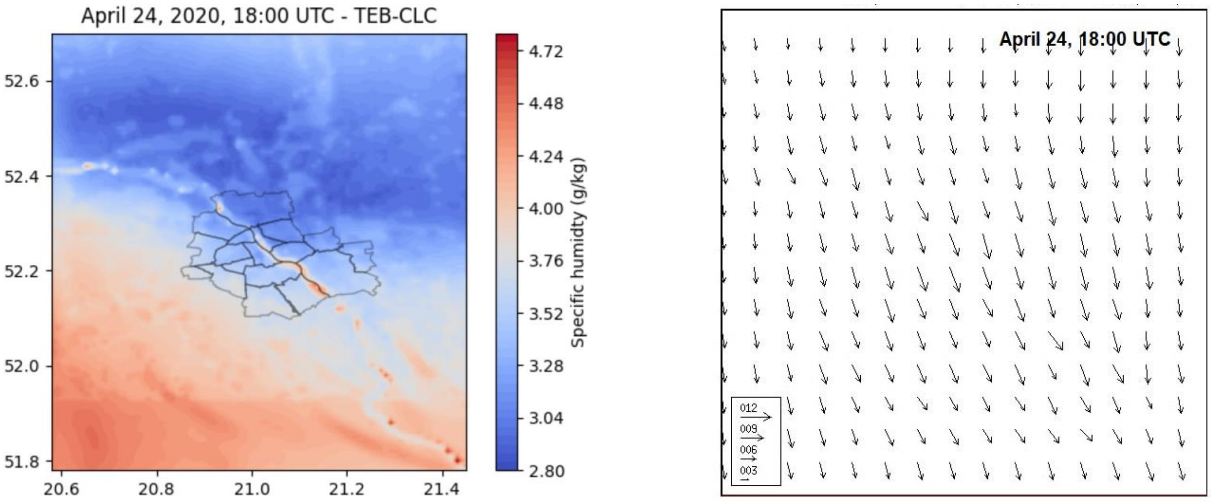

Fig. 45. Spatial distribution of specific humidity (left panel), wind speed and direction (right panel) on April 24, 2010, at 18:00 UTC. The contour lines in the plots present the administrative borders of Warsaw city.

4.2.3 Precipitation rate

While the impacts of urbanisation on temperature are well studied and understood, the effect of land cover on precipitation is still evolving. The precipitation changes are dynamic and depend on several factors, including wind and heating at the surface and in the boundary layer due to surface characteristics and aerosols above the urban surface (Liu and Niyogi 2019). Typically, to analyse urbanisation impacts on precipitation in a modelling study, the urban region is replaced by the non-urban land cover (Liu and Niyogi 2019). For instance, Shem and Shepherd (2009) examined physical processes linked to the Atlanta urban rainfall effect using the WRF model to simulate convective precipitation within URBAN and NOURBAN simulations for two summer cases. They show that the URBAN model captures the convective evolution for the cases. At the same time, the NOURBAN simulation indicates that removing the city causes distinct differences in the temporal and spatial evolution of precipitation. Niyogi et al. (2011) performed two simulations with and without the urban land cover in Indianapolis, Indiana

(USA), for examining thunderstorms. Their results show that removing the urban region caused differences in the regional convergence and convection and simulated base reflectivity, surface energy balance, and boundary layer structure.

One of the major research studies focusing on the impact of urbanisation on the temporal and spatial distribution of precipitation was performed during the Metropolitan Meteorological Experiment (METROMEX) in St. Louis (USA). This study proved that urban effects are more pronounced in warm-season months when mesoscale convective forcing is likely to be more dominant than synoptic forcing (Auer 1981).

Precipitation patterns around cities suggest enhancing precipitation downwind of the urban areas, particularly in the summer season with convective rainfall (Oke et al. 2017). Figure 46 presents the hourly average precipitation rate for three scenarios for four selected dates with different meteorological behaviour.

Model-derived temperature and UHI effect was shown in Fig. 39 for the 24-hour simulation. C3 shows a strong nocturnal UHI. Comparing sensible heat flux in the three scenarios, we can observe the highest sensible heat flux at night in the urban area with high buildings, as compared to the natural land cover on June 6 (Fig. 47). According to the literature (Oke et al. 2017), heating from an urban area can be sufficient to create an area of upward motion downwind of the city. The urban heating causes perturbations in the wind field, which leads to the horizontal convergence around the zone of upward motion downwind of the city.

The strength of the upward motion increases with the increase in the UHI intensity. The intensity of the urban heat island is the simplest and most quantitative indicator of the cities'

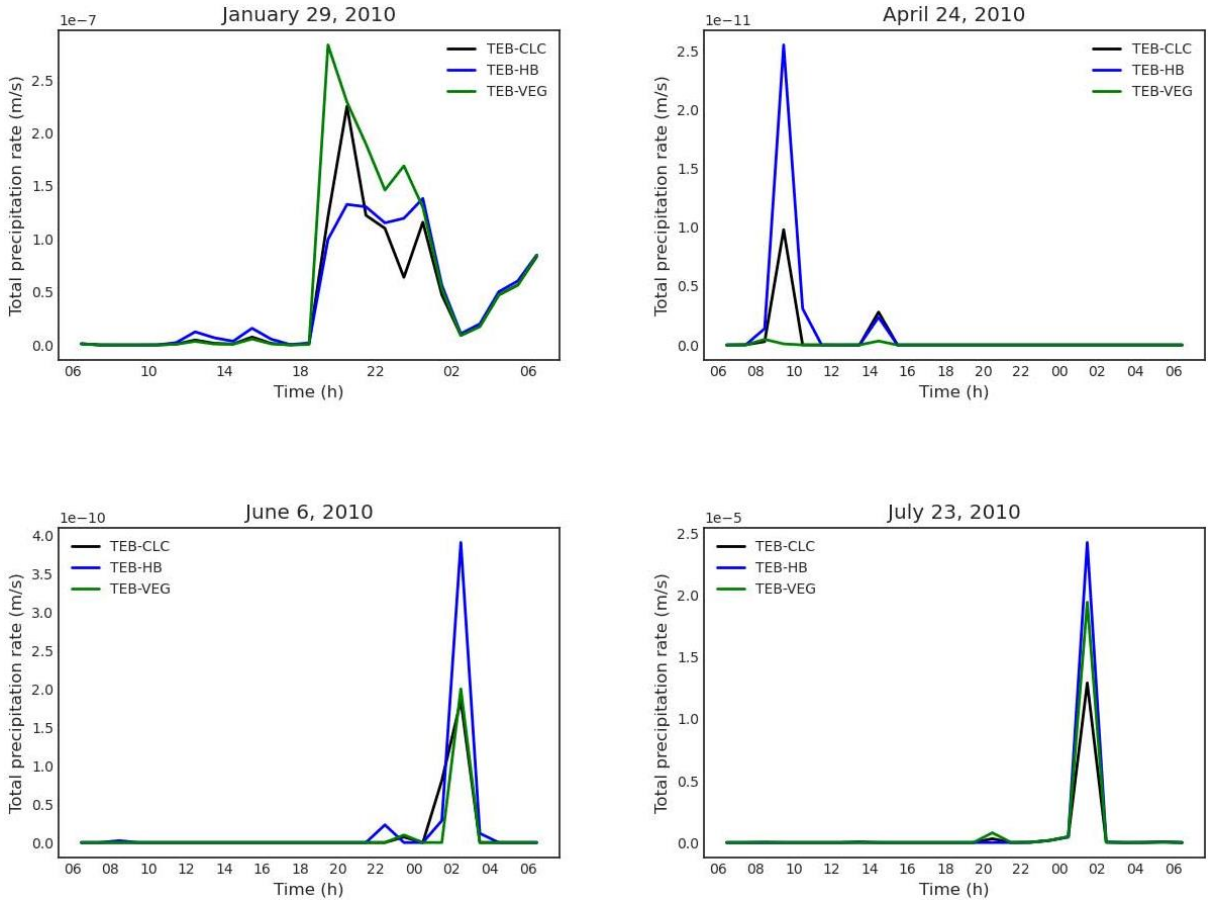

Fig. 46. Hourly average evolution of precipitation rate for three sensitivity scenarios (TEB-CLC, TEB-HB, TEB-VEG) for four selected dates in Warsaw, 2010.

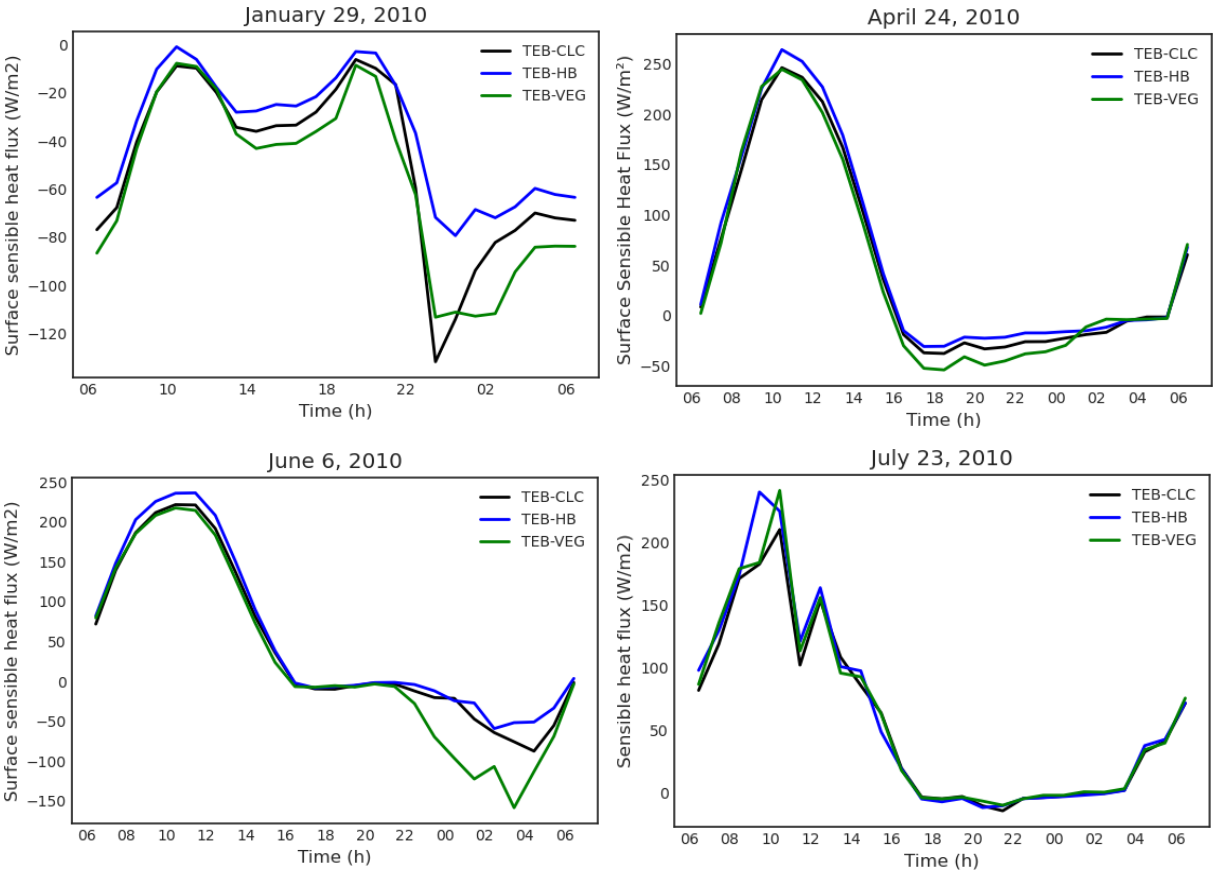

Fig. 47. Hourly average evolution of surface sensible heat flux for three sensitivity scenarios (TEB-CLC, TEB-HB, TEB-VEG) for four selected dates inWarsaw, 2010.

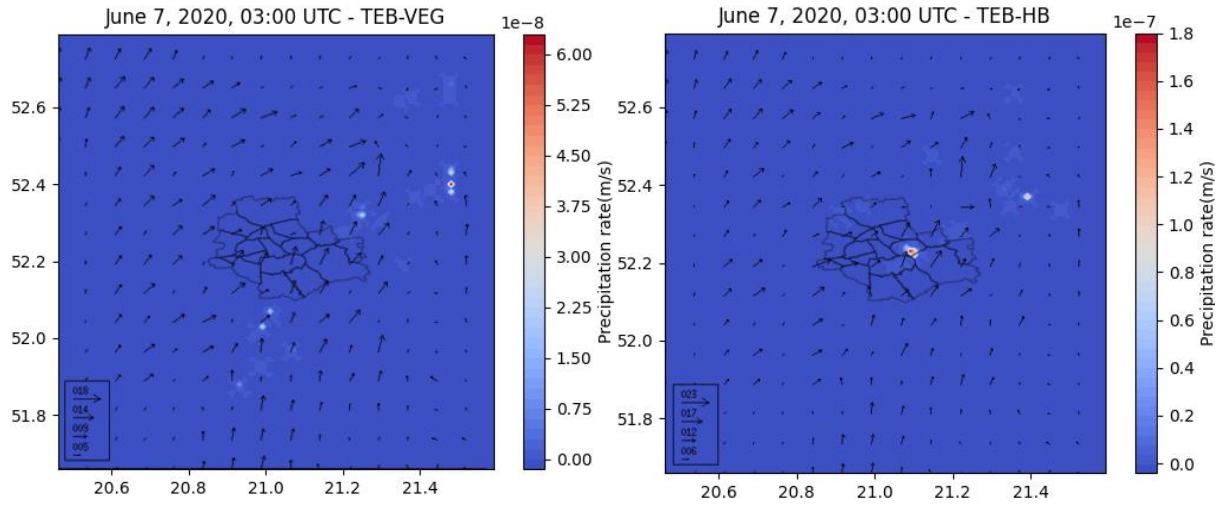

Fig. 48. Wind field over a surface and precipitation rate for the vegetated (TEB-VEG) land cover (left panel), and the urban area with high buildings (TEB-HB) (right panel) on June 7, 2010, at 03:00 UTC. The contour lines in the plots present the administrative borders of Warsaw city.

relative warming in respect to the surrounding rural environment at night time (Kim and Baik 2002) and a decrease in the synoptic-scale wind speed. For studying the impact of land use/land cover and urban heat island on the precipitation in the city, two extreme scenarios (TEB-HB and TEB-VEG) were taken into account. For this purpose, June 6 was studied, because of showing a strong nocturnal urban heat island. Based on Fig. 48, the urban heat island circulation

involves low-level convergence and upward motion, which are forcings to produce urban-induced precipitation in the late spring case. Having higher buildings cover, the urban area increases the UHI intensity (Fig. 39) and the upward motion, which results in a convective precipitation rate in the TEB-HB scenario.

Even though April 24 was a calm day and it was no precipitation day, it can be seen in Fig. 46 that covering the city with more mid-high buildings (TEB-HB) causes a small amount of precipitation in the city in the morning and in the afternoon, while in the no urban scenario (TEB-VEG), there is no precipitation. The precipitation in the urban area (TEB-HB) can be due to the higher temperature in the urban area with the mid-high buildings and higher sensible heat flux, which causes upward motion and urban-induced precipitation (Fig. 49).

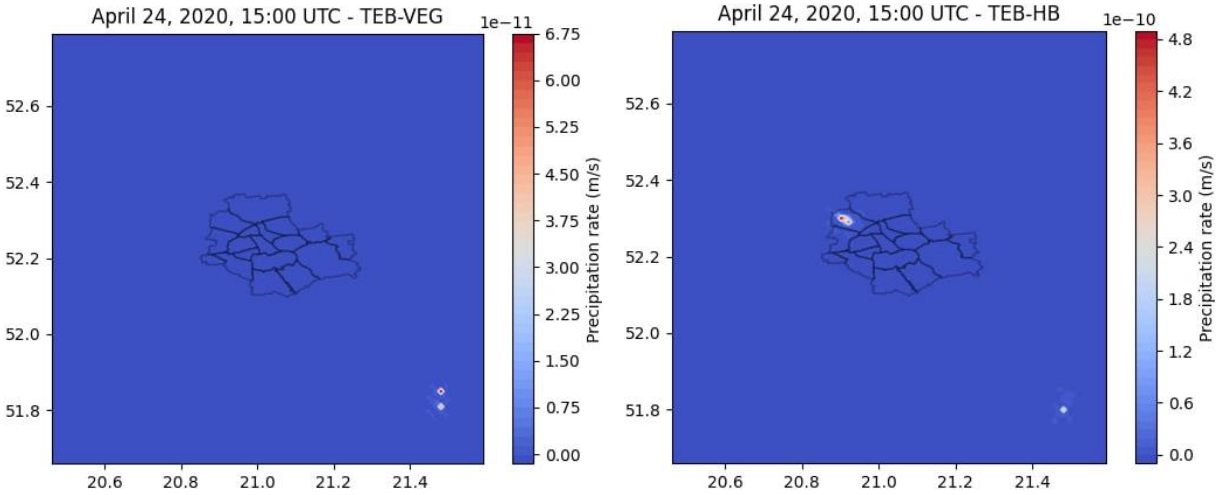

Fig. 49. Spatial distribution of precipitation rate for TEB-VEG scenario (left panel), and TEBHB scenario (right panel) on April 24, 2010, at 15:00 UTC. The contour lines in the plots present the administrative borders of Warsaw city.

4.2.4 Turbulent kinetic energy

The dominant environmental factors that control the urban turbulence are the high roughness (buildings, trees, and other large structures) of the urban surface and the urban heat islands (Roth 2000).

Figure 50 presents the turbulent kinetic energy (TKE) over the three land covers for all four cases. TKE is a measure of turbulent intensity which can be also influenced by the heterogeneity-induced atmospheric motions.

One of the typical features of the urban surface is being warmer than the surrounding areas due to the increased heat storage and reduced evaporation from the artificial urban surfaces (Emeis et al. 2007).

The main reason for the higher turbulent kinetic energy in Fig. 50 is the higher temperature above the urban surface (shown in Fig. 39) compared to the natural surface (TEB-VEG). Thermal turbulence is caused mainly by surface heating. When the surface heats air parcels, they impose buoyancy force which accelerates the thermals. Thermals create friction and mixing between themselves and the surroundings and produce TKE. The TKE from thermal turbulence is greatest when the buoyancy is strong (Oke et al. 2017).

Because convection and buoyancy produce turbulence, the atmosphere is dynamically unstable in C2, C3, and C4. The TKE above the surface for C2, C3, and C4 is high during the day for the TEB-HB scenario and is the smallest for the TEB-VEG scenario. Figure 51 shows the generation of convective turbulence during the daytime due to high temperature and humidity,

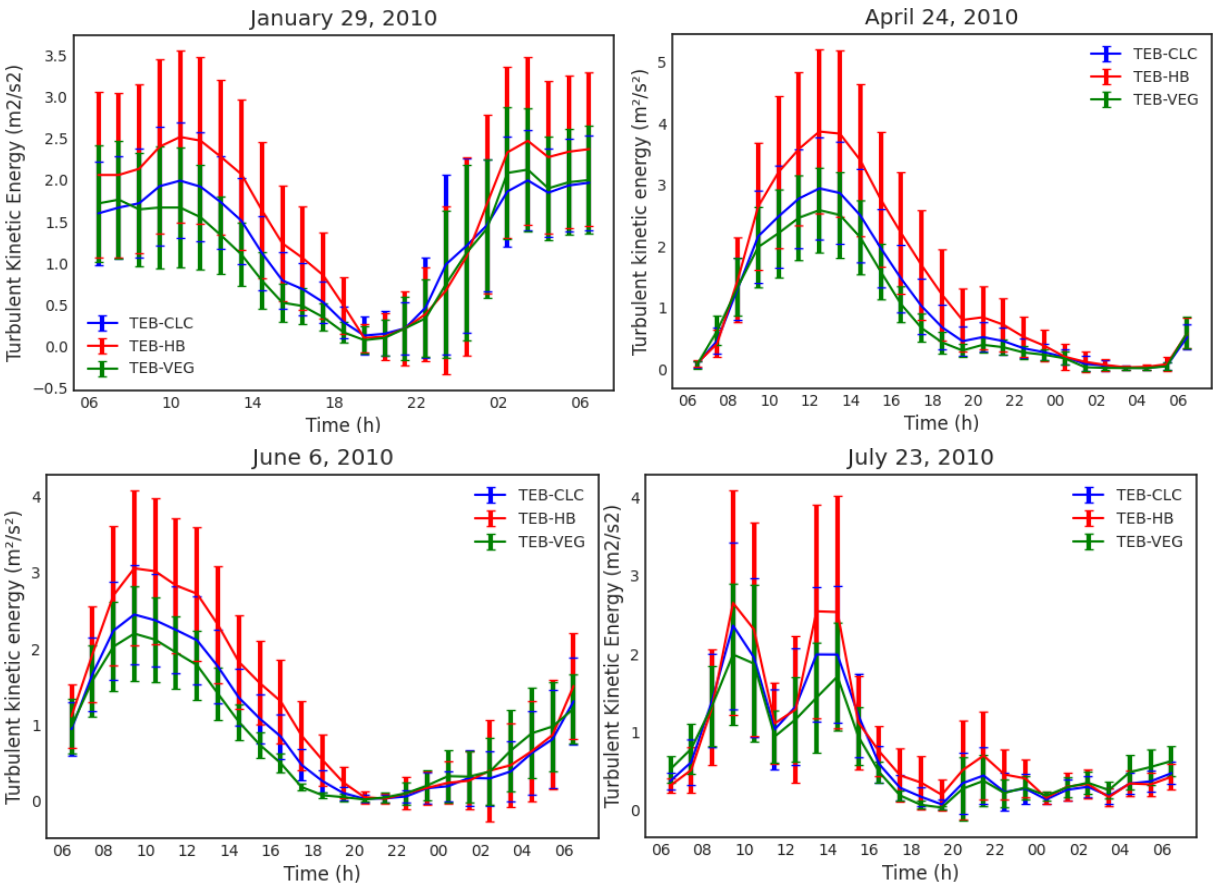

Fig. 50. Hourly average course of turbulent kinetic energy for three sensitivity scenarios (TEB-CLC, TEB-HB, TEB-VEG) for four selected days in Warsaw, 2010.

which pushes the boundary layer upward and forms a deep turbulent layer till sunset in C2, C3, and C4 cases, which is significantly higher and the mixed layer is deeper considerably in the urban scenario and especially in the TEB-HB scenario than in the TEB-VEG scenario. Indeed, thermal effects become increasingly dominant at higher altitudes.

On April 24 and July 23, with the reduction of temperature at night, the atmosphere becomes very stable at night above the surface. Therefore, TKE also decreases and reaches zero at height of almost 400 m (Fig. 50). If the surface is cooler than the atmosphere above, the coldest air stays closer to the surface, and TKE will be dissipated. The small values of TKE for TEB-HB in these cases are due to the warmer surface's thermal effect at night in the urban scenario and, especially, in the summer case, after sunset at 22:00 UTC, the surface is still warm and produces small values of TKE near the surface.

In the C1 case, there is a shallow boundary layer near the surface during the day, and TKE is high (almost 1 m^2/s^2 difference between TEB-HB and TEB-VEG scenario) near the surface for urban scenarios, TEB-HB with more mid-high buildings. However, TKE decreases with height and reaches zero eventually at a height of ~1000 m. TKE in the lower altitudes is due to the thermal effects of the surface. At night, TKE is higher in TEB-HB scenario than in the TEB-VEG scenario near the surface because of the thermal effects of the warmer surface. However, in the higher altitudes, TKE is lower for TEB-HB, which can be related to the lower atmosphere stability in TEB-HB and weaker inversion. As a result, the higher TKE in the higher altitudes can be due to the wind shear with the existence of inversion.

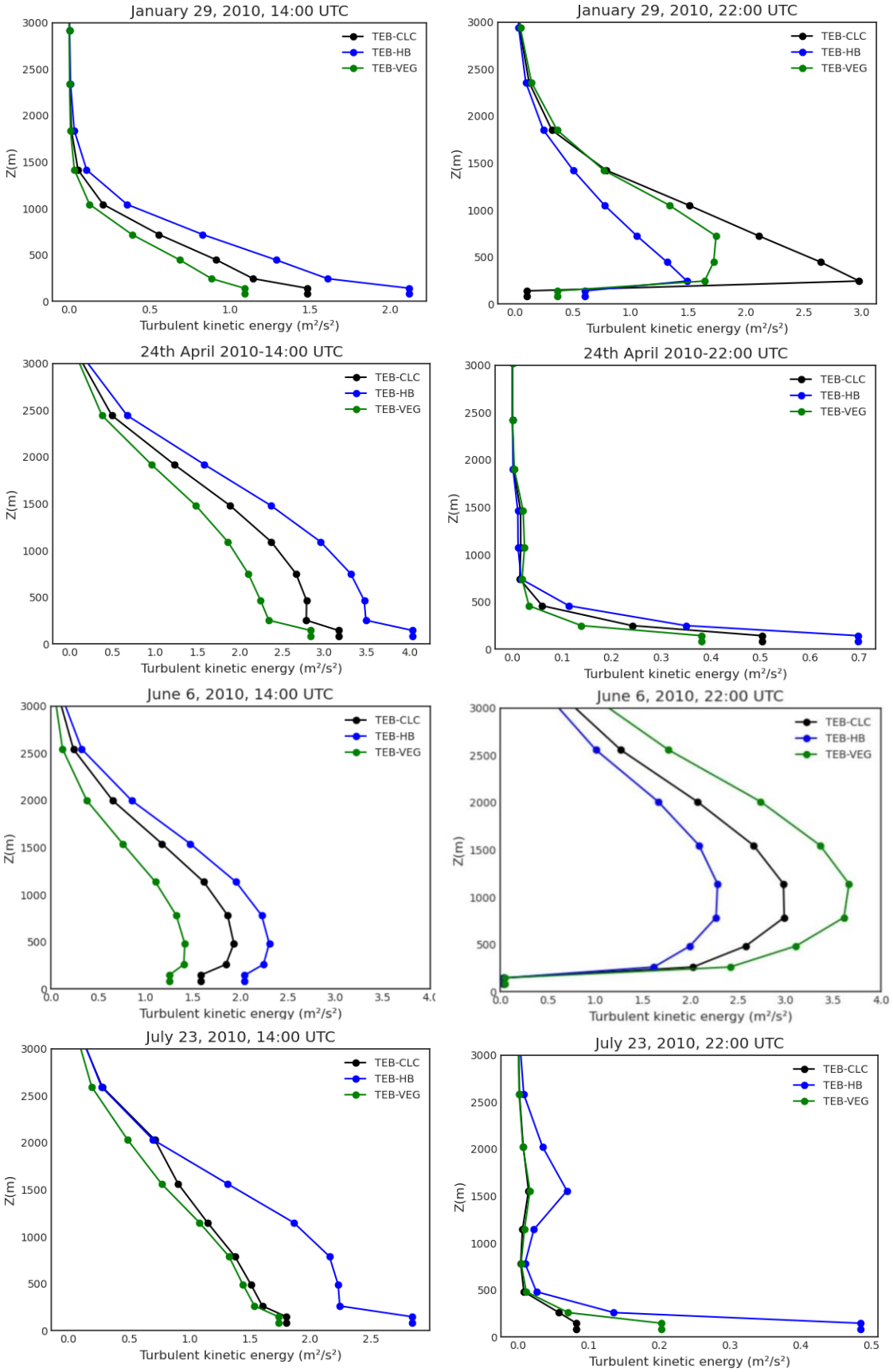

Fig. 51. Vertical profile of turbulent kinetic energy for three sensitivity scenarios (TEB-CLC, TEB-HB, TEB-VEG) for four selected cases and within the calculated averaged grid in 2010 at 14:00 UTC (left panel) and 22:00 UTC (right panel).

In general, changes in the urban surface from sporadic buildings to mid-high buildings increase the TKE considerably, according to Fig. 50, because of an increase in the surface roughness, which was explained in Section 4.1.1.

4.3 Statistical evaluation – forecast performance

Statistical evaluation allows for quantitative analysis of the model's performance over the city of Warsaw. Even though the short length of the simulations does not allow for significant error measure analysis, the intention is to compare results from two scenarios in terms of the forecast skill score.

The observational data used in this validation is the temperature from selected stations in Warsaw. Three statistical measures were calculated: the mean bias error (MBE), the absolute gross error (MAGE), Pearson correlation coefficient between the NO-TEB (non-urban model) and observed data, and the TEB (urban model) and the observed data, separately (Table 12).

Table 12

Statistical error measure over selected stations in Warsaw

		MBE		MAGE		Correlation	
Date	Stations	NO-TEB	TEB	NO-TEB	TEB	NO-TEB	TEB
January 29, 2010	Radzymińska	–1.18	–0.05	1.86	1.24	–0.17	0.10
	Jerozolimskie	–1.55	0.11	2.53	1.35	–0.01	0.16
	Bielany	–3.19	–1.52	3.35	2.01	–0.17	–0.01
	Puławska	–1.58	–0.49	2.13	1.63	–0.11	0.05
	Krakowska	–3.54	–1.88	3.65	2.17	–0.08	n/a
	Jelonki	–2.75	–0.83	2.92	1.40	–0.20	–0.10
April 24, 2010	Radzymińska	–0.44	0.26	0.89	0.45	0.98	0.99
	Jerozolimskie	–1.17	–0.27	1.45	0.60	0.98	0.99
	Puławska	2.13	3.07	2.16	3.07	0.88	0.90
	Krakowska	0.075	0.013	1.60	1.89	0.95	0.93
June 6, 2010	Radzymińska	1.49	2.44	1.77	2.44	0.87	0.90
	Jerozolimskie	2.13	3.07	2.16	3.07	0.88	0.90
	Bielany	–0.29	0.65	1.31	1.39	0.94	0.95
	Puławska	2.40	2.36	2.45	2.36	0.81	0.90
	Krakowska	1.54	2.02	1.54	2.02	0.97	0.95
July 23, 2010	Radzymińska	–1.20	–1.26	1.70	2.023	0.94	0.93
	Jerozolimskie	0.075	0.013	1.60	1.89	0.95	0.93
	Bielany	–0.95	–0.83	1.24	1.51	0.91	0.86
	Puławska	0.15	–0.28	1.24	1.43	0.958	0.955
	Krakowska	–1.005	–1.32	1.57	1.95	0.91	0.91
	Jelonki	–1.02	–1.04	1.61	1.26	0.80	0.81

Note: n/a means no correlation.

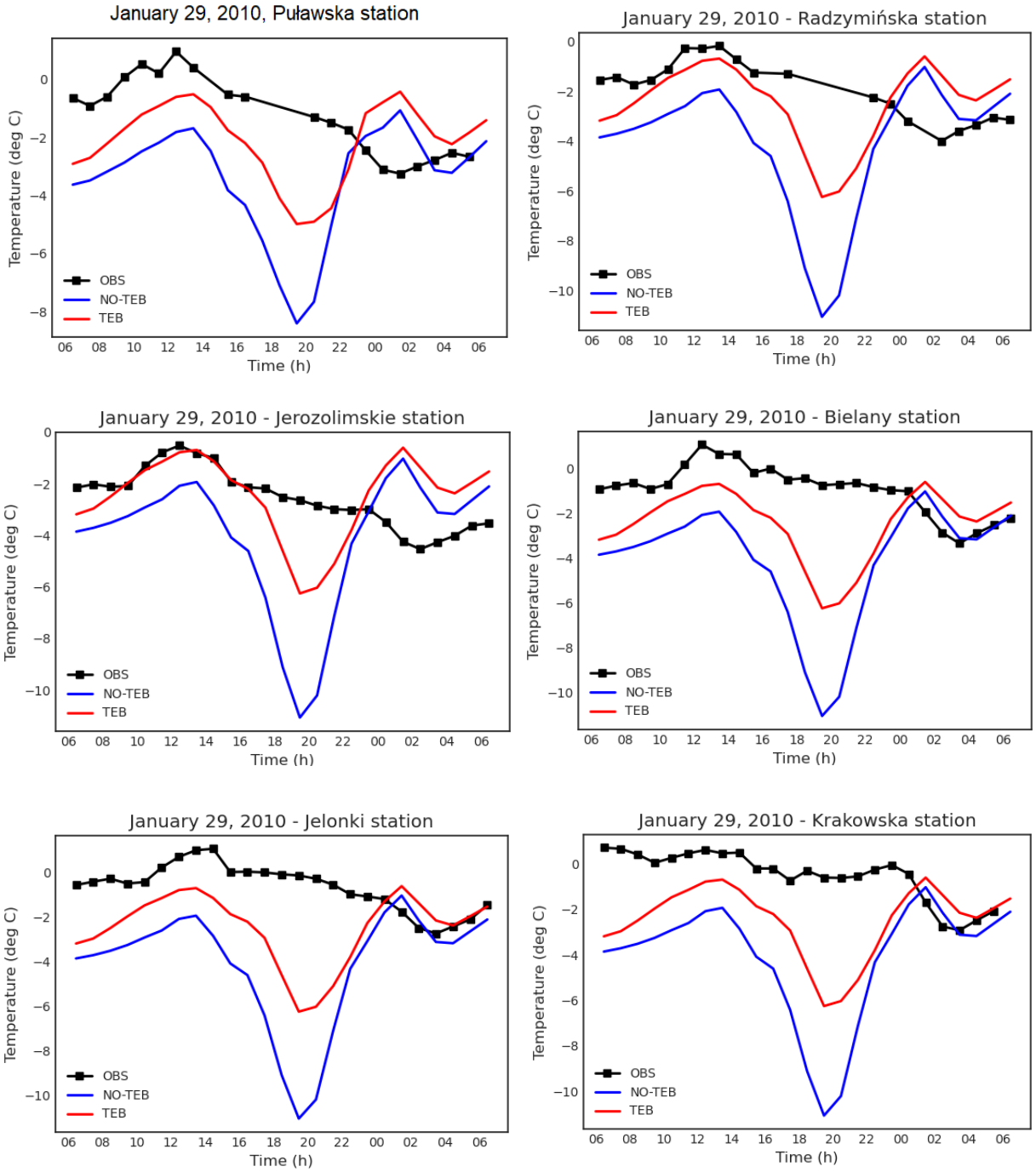

Fig. 52. Comparison of modelled temperature with observations for Puławska, Radzymińska, Jerozolimskie, Bielany, Jelonki, and Krakowska stations for January 29, 2010.

Error measures were calculated for each station and four cases. Data for April 24 from Bielany and Jelonki stations were not available.

24 observational data points (hourly average) and the corresponding model output were used. The output frequency from the model was 10 minutes, and hourly average data were calculated.

Near-surface temperature changes in the urban scenario (TEB) resulted in better model performance in C1 (January 29) (Fig. 52). The MBE was reduced by a factor of 3, and MAGE is

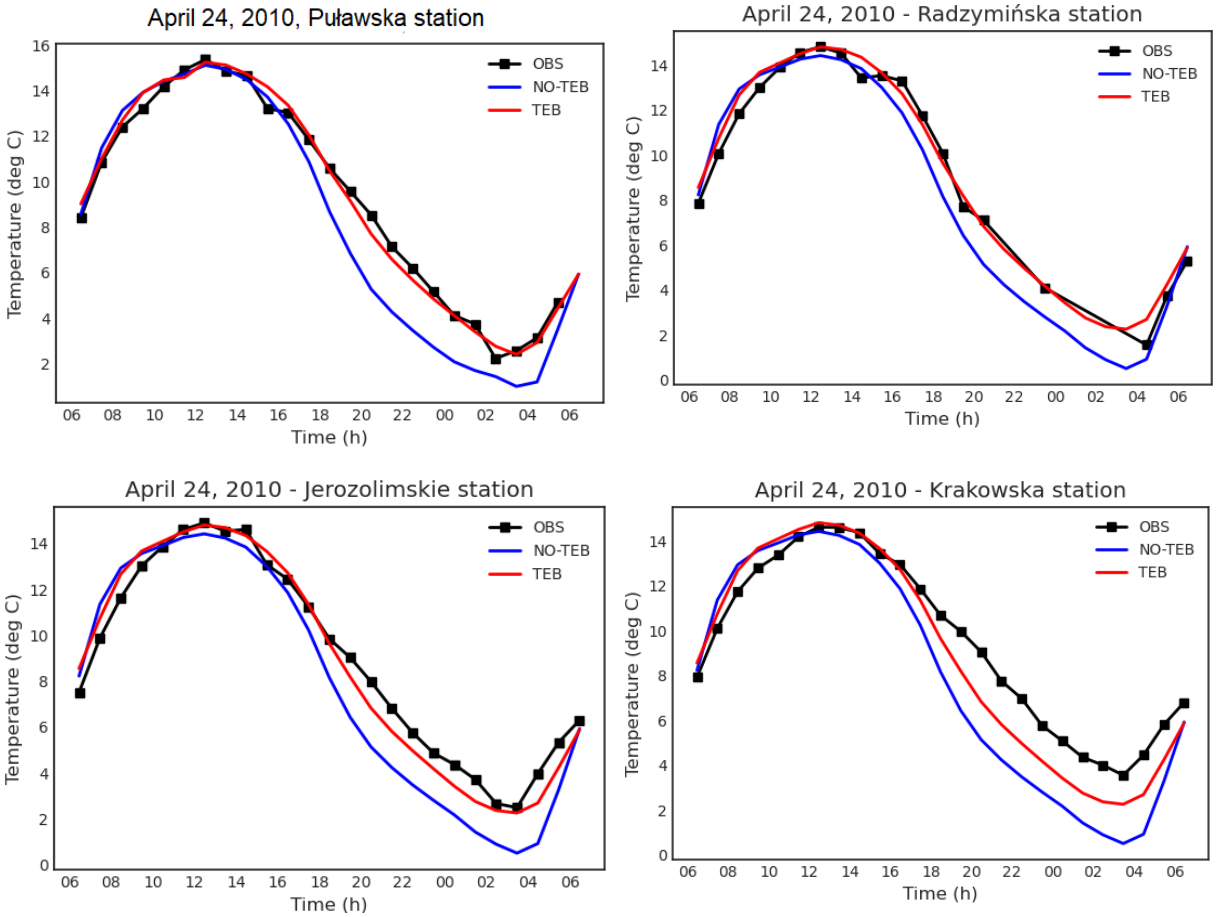

Fig. 53. Comparison of modelled temperature with observations for Puławska, Radzymińska, Jerozolimskie, and Krakowska stations for April 24, 2010.

smaller than in the non-urban scenario (NO-TEB) by half. The MBE value indicates that the model underestimates temperature for the winter case (January 29). Also, it can be seen in Fig. 56 that the model underestimates the near-surface temperature in the winter case. Results from Radzymińska and Jerozolimskie stations show a very good performance of the TEB model during the day in C1, but the model underestimated the temperature at night based on the measures from all the stations. Thereby, despite the reduction in MBE and MAGE in the urban (TEB) scenario, the correlation coefficient was not improved. There is a weak correlation and relatively high standard deviation for the NO-TEB scenario in the winter case. Cloud cover in the model is significantly lower than the real situation for C1, which causes the high surface cooling in the model and as a result underestimation of the temperature at night.

Error measures for temperature on April 24 (case C2) show that the modelled near-surface temperature is very close to the observation for the urban (TEB) scenario. MBE values for the spring case show a relative underestimation of the model in the non-urban (NO-TEB) scenario. MBE and MAGE were reduced by half in the TEB scenario, and the correlation was improved considerably. There is a strong correlation and lower standard deviation for the urban scenario than the non-urban scenario (Fig. 53). As shown in Fig. 57, the model underestimates the temperature in the spring case for the NO-TEB scenario.

The introduction of the TEB parameterisation did not result in an improvement in MAGE and MBE for C3 (June 6) except for the Puławska station (Fig. 54). Positive MBE values for

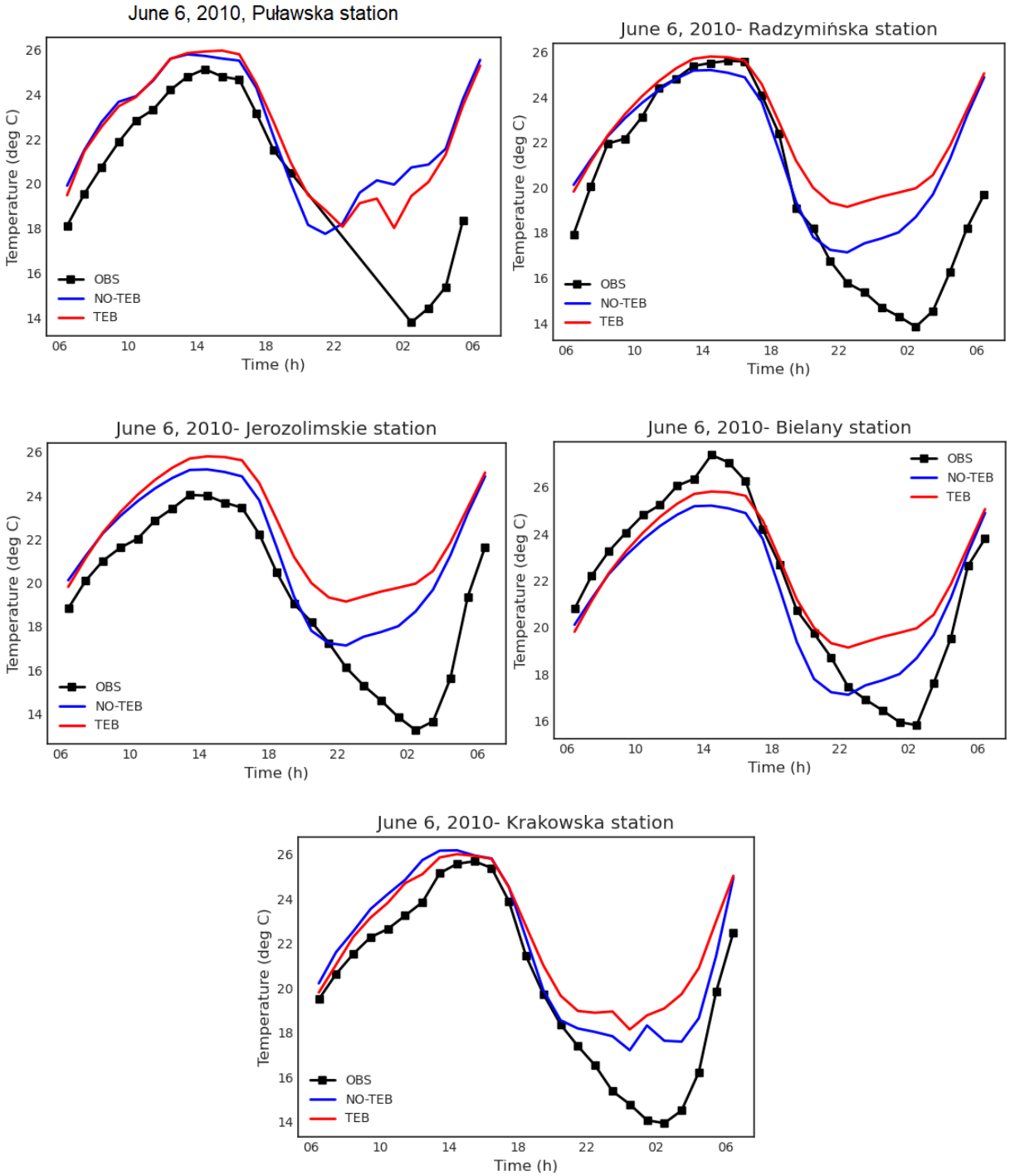

Fig. 54. Comparison of modelled temperature with observations for Puławska, Radzymińska, Jerozolimskie, Bielany, Jelonki, and Krakowska stations for June 6, 2010.

the June 6 case indicate that both scenarios tend to overestimate the near-surface temperature, especially during the night, aside from Bielany station, which underestimates the temperature for the NO-TEB scenario (Fig. 54). The correlation is slightly improved in the urban scenario for the observational data obtained from Puławska and Radzymińska stations (Fig. 54). However, high values of MBE and MAGE in Fig. 58 show that C3 did not have a good performance at night when observations showed a sudden surface cooling at night.

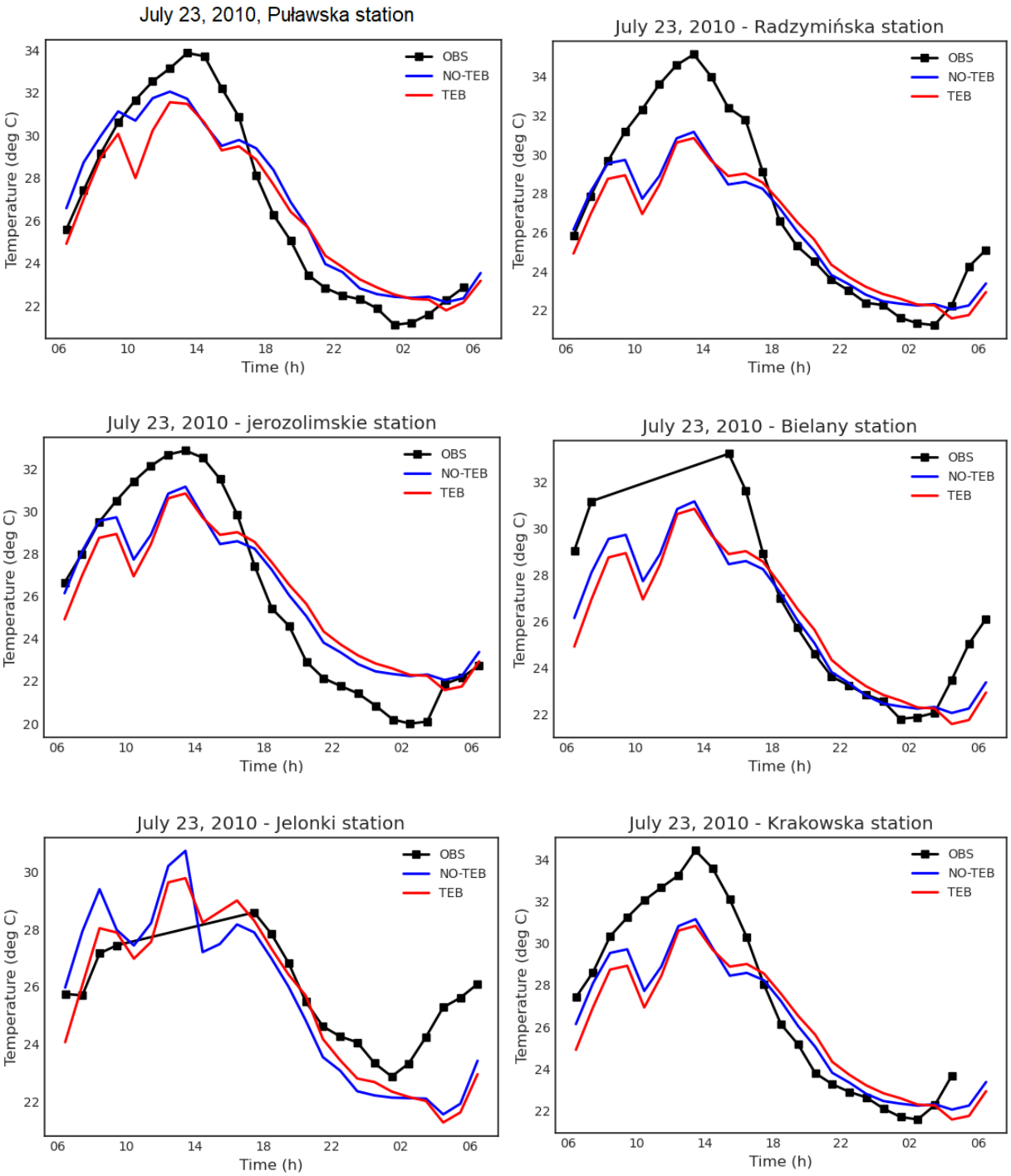

Fig. 55. Comparison of modelled temperature with observations for Puławska, Radzymińska, Jerozolimskie, Bielany, Jelonki, and Krakowska stations for July 23, 2010.

In the summer case (C4, July 23), MBE values from other stations indicate that the two scenarios underestimate the temperature. However, both scenarios overestimate the temperature at night (Fig. 59). Adding the TEB parameterisation did not improve the MAGE and the MAGE values for the TEB scenario. This shows that the model performance was not improved by TEB parameterisation (Fig. 55). Also, it indicates that urban parameterisation will not improve the

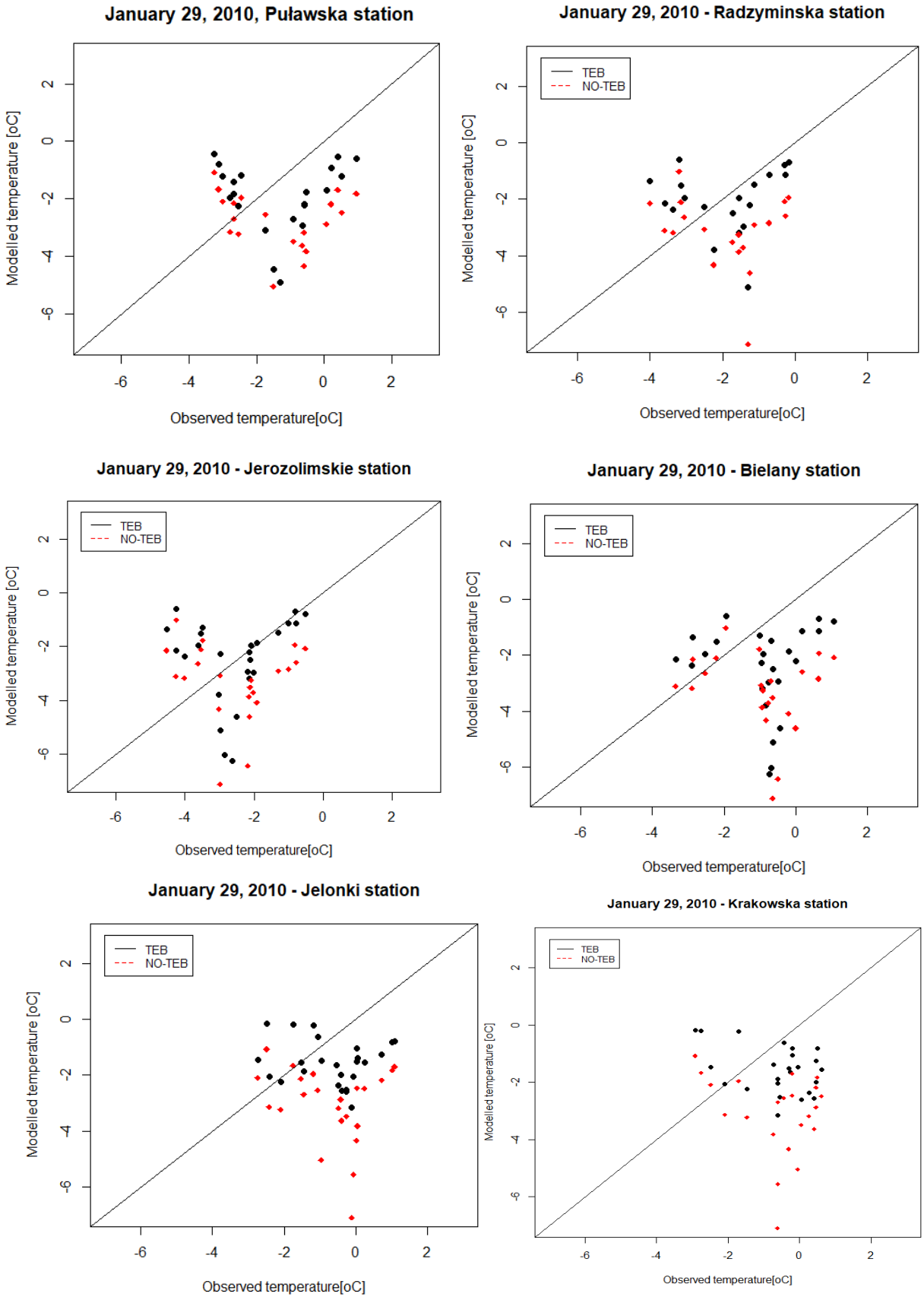

Fig. 56. Near-surface temperature measured at Puławska, Radzymińska, Jerozolimskie, Bielany, Jelonki, and Krakowska stations and calculated by the GEM model for January 29, 2010.

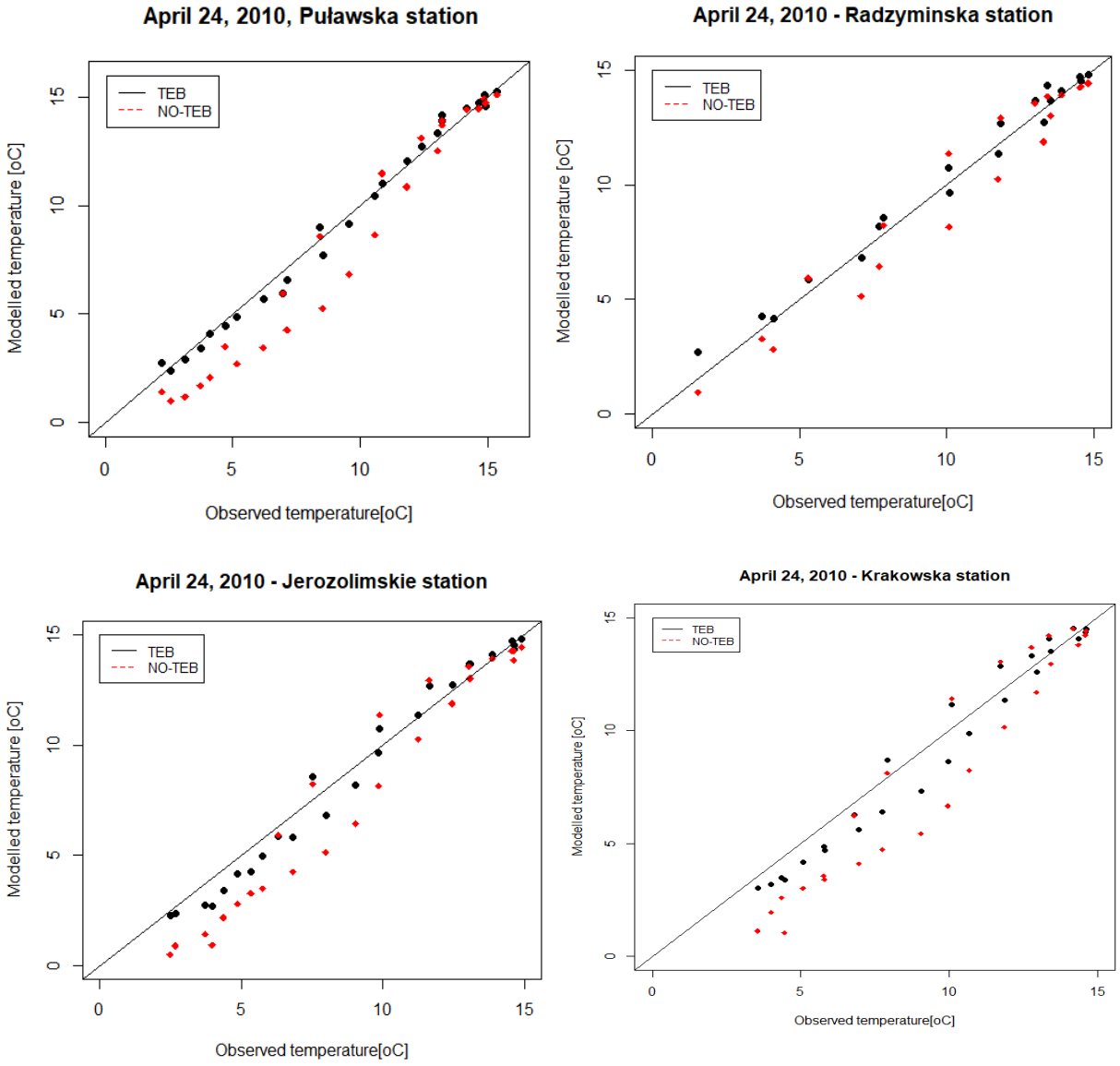

Fig. 57. Near-surface temperature measured at Puławska, Radzymińska, Jerozolimskie, and Krakowska stations and calculated by the GEM model for April 24, 2010 (case C2).

modelling results for days characterised by dynamic changes in meteorological situations. Nevertheless, the modelled data for both scenarios correlate well with the summer case observations.

4.3.1 Sounding profiles from Legionowo station

Legionowo station is out of the domain which was taken for the analysis, and it is in a rural neighbourhood. For the purpose of this comparison, the vertical profiles from the model obtained from the cell representing the Legionowo station coordinates were used.

Figures 60 and 61 present the comparison of the sounding profiles from Legionowo station with the vertical profiles obtained from the NO-TEB and TEB models.

The comparison of the vertical profiles of temperature with the soundings showed that TEB improved model performance in reproducing temperature during the day time. This improvement is prominent for C2. In C1, there is a lack of data between the altitude of 96 to ~500 m; having the current data, the TEB scenario has improved the model performance for the winter

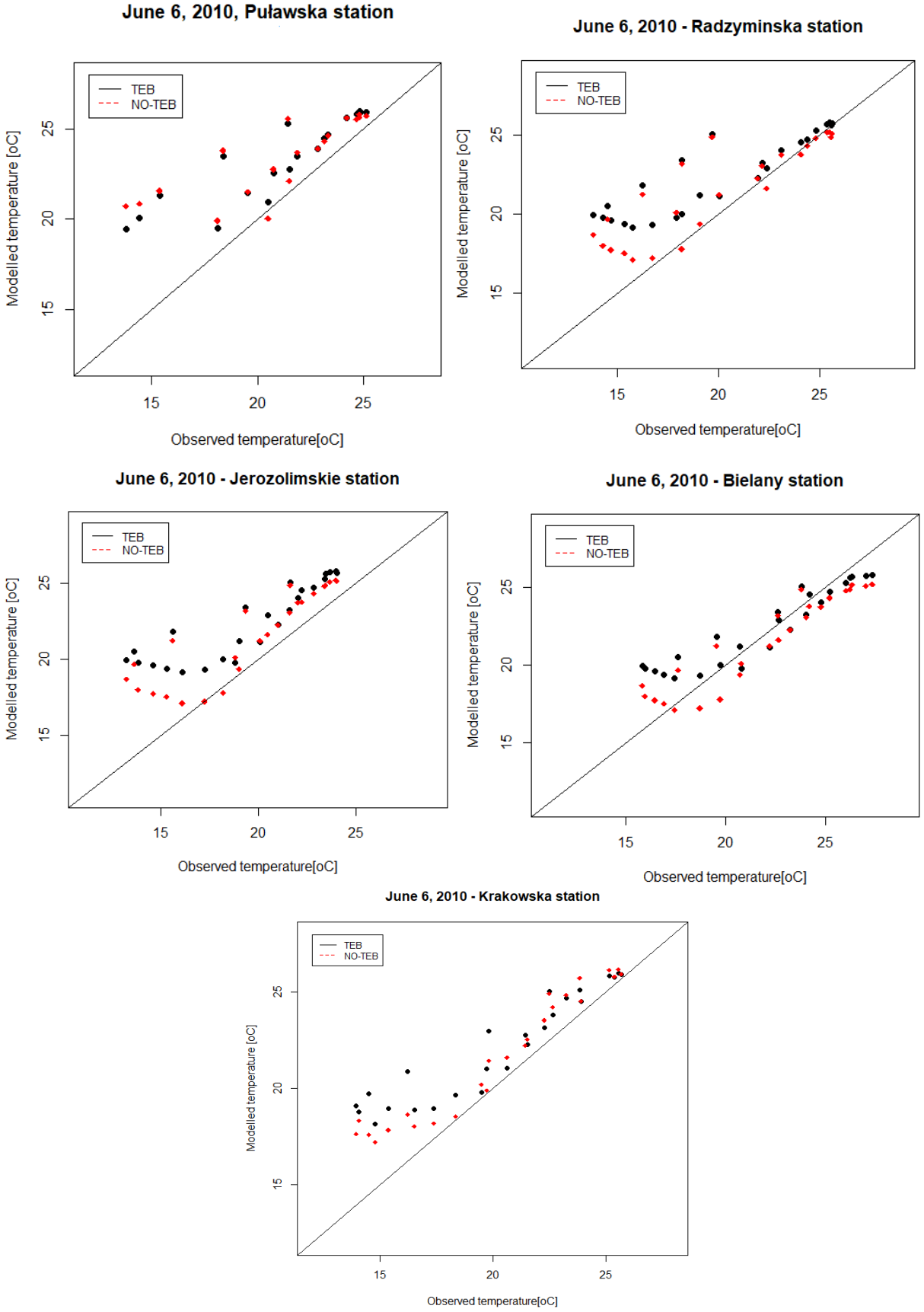

Fig. 58. Near-surface temperature measured at Puławska, Radzymińska, Jerozolimskie, Bielany, and Krakowska stations and calculated by the GEM model for June 6, 2010 (case C3).

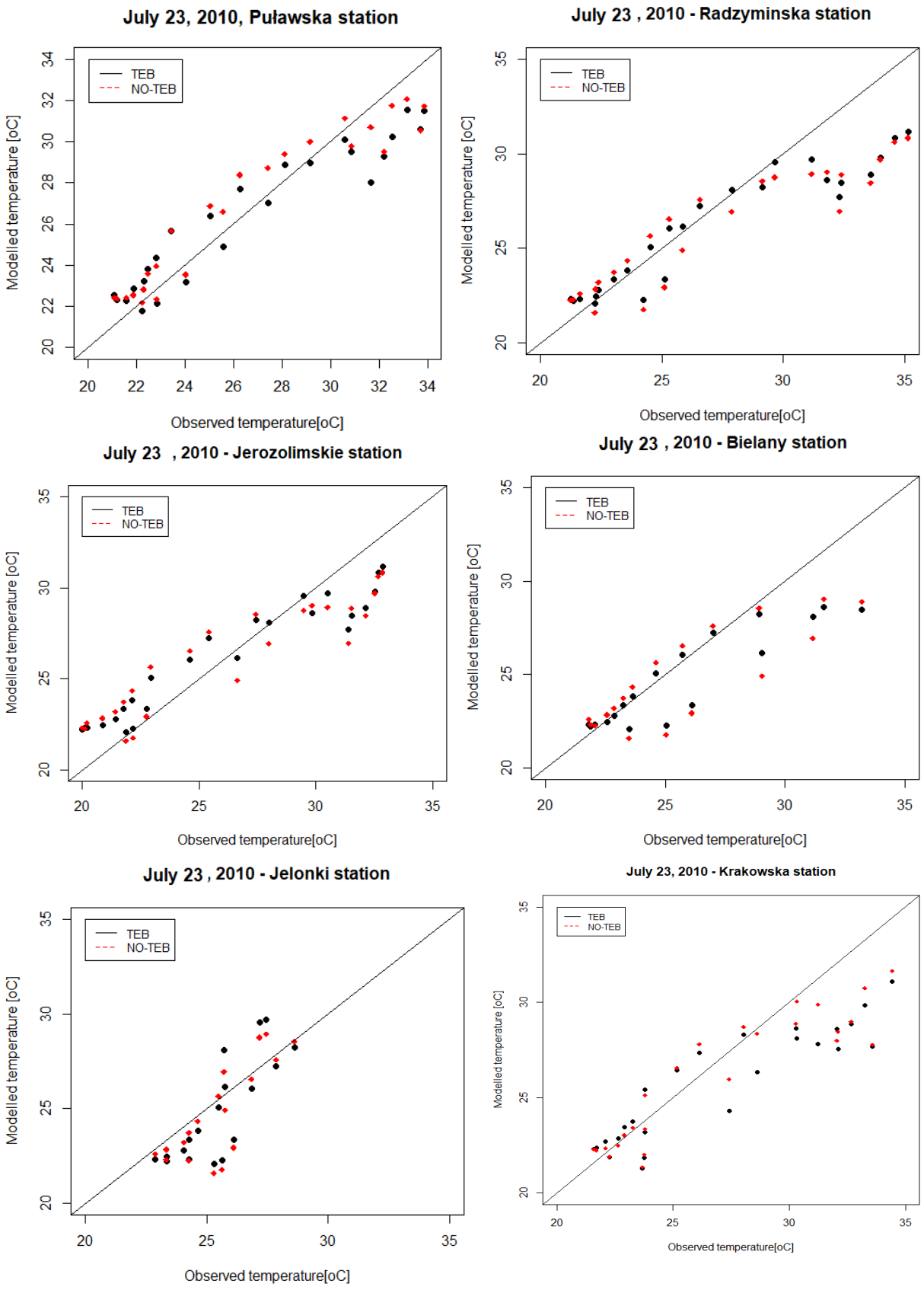

Fig. 59. Near-surface temperature measured at Puławska, Radzymińska, Jerozolimskie, Bielany, Jelonki, and Krakowska stations and calculated by the GEM model for July 23, 2010 (Case C4).

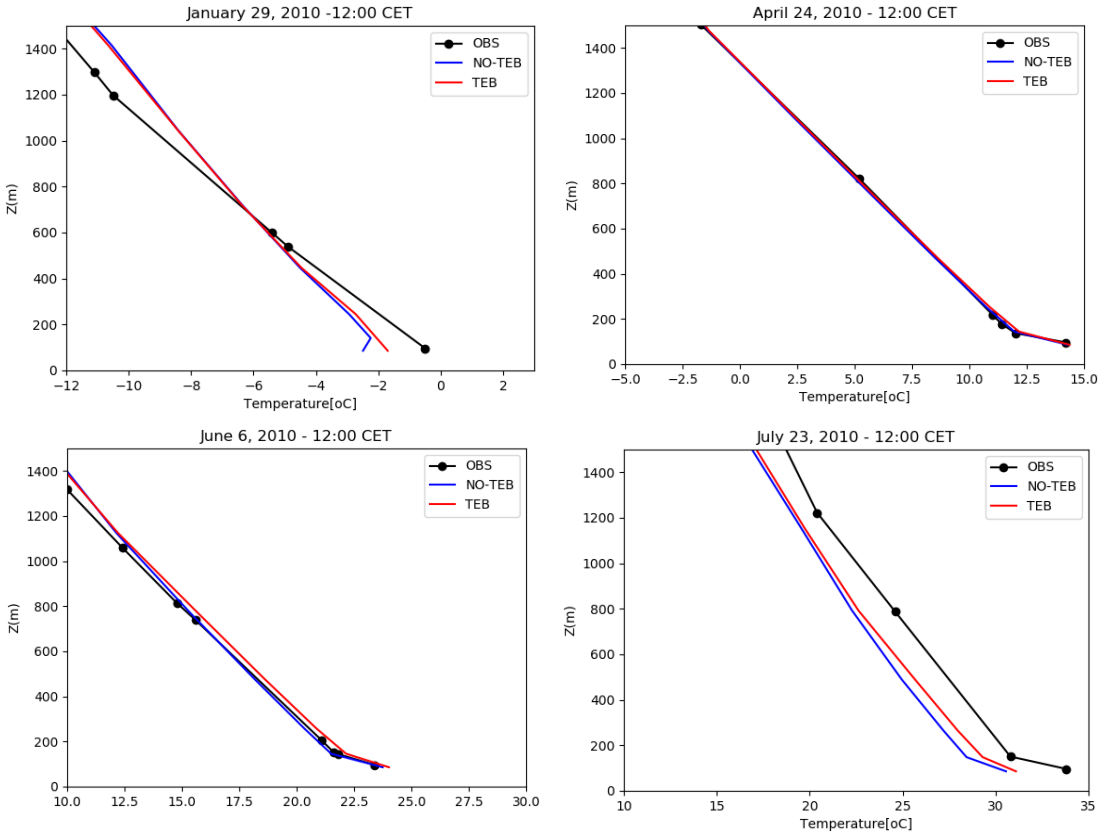

Fig. 60. Comparison of sounding profiles from Legionowo station with the vertical profiles from TEB and NO-TEB models for January 29, April 24, June 6, and July 23 at 12:00 CET.

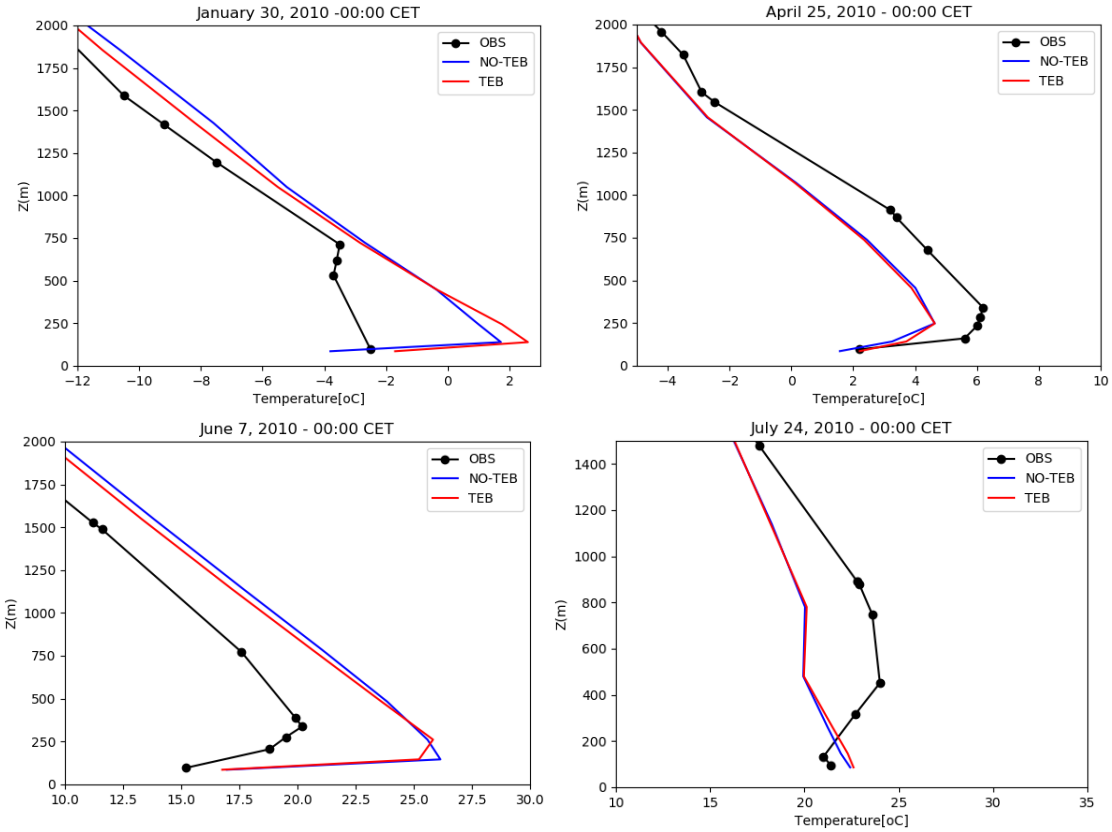

Fig. 61. Comparison of sounding profiles from Legionowo station with the vertical profiles from TEB and NO-TEB models for January 30, April 25, June 7, and July 24 at 00:00 CET.

case significantly compared to the NO-TEB scenario. In C3, the TEB model overestimates the temperature slightly. For the C4, both TEB and NO-TEB scenarios underestimate the temperature up to the top of the boundary layer.

A comparison of the sounding profiles with the vertical profiles taken from the model for the night-time shows that there is no considerable difference between two scenarios in higher alitudes. C1 and C2 improved the model performance, specifically near surface. For C1, there is a data gap up to a height of ~530 m. As a result, the existence of near surface inversion cannot be confirmed. C3 overestimates the temperature, specially for the upper altitudes. In C4, both models performed well near the surface. At the higher altitudes, soundings show upper air inversion, which is stronger and deeper than the model profiles.

5. CONCLUSIONS AND FUTURE WORK

5.1 Conclusions

The sensitivity study with the GEM model in a high-resolution configuration was undertaken to assess the impact of urban land cover on the boundary layer over Warsaw in Poland and on a short-term meteorological forecast considering two scenarios with and without town energy balance (TEB) parameterisation.

The TEB parameterisation represents urban effects on modelled meteorological parameters at the final nesting level with a horizontal resolution of 1 km over Warsaw. In this thesis, the TEB parameterisation considers the following urban cover categories: mid-high buildings, sparse buildings, industrial areas, and roads.

For sensitivity analysis, four one-day cases with different temperature variabilities, as well as different weather patterns representing winter case (C1), spring case (C2), late spring case (C3), and summer case (C4), were selected.

Studying the urban boundary layer development based on two scenarios yielded the following results:

- Temperature profiles for four cases show that the nocturnal inversion was weaker over urban land cover (with the TEB scenario). In the winter case (C1), there was a strong and deep inversion in the morning and night for the NO-TEB scenario. On the other hand, there was no inversion in the morning in the TEB scenario. The depth and strength of inversion after midnight were small. Weak inversion in the TEB scenario was due to the heat release from the building materials at night and from anthropogenic sources. The higher temperature in urban areas created a nocturnal mixed layer. As stated by Oke et al. (2017), the most densely built-up districts of cities release ΔQs from the building materials and *QF* from vehicles and buildings. This is sufficient to support an upward *QH* and a weakly convective lower layer, and a weak nocturnal version of the daytime mixed layer is formed. The temperature within the canyon is higher and warmer than a cool layer at the roof level, so the inversion at night is weaker above the built-up area;
- The temperature cross-section for the winter case showed that the impact of the warmer surface is to a height of 100 m due to lower mixing in winter. There was a higher temperature in the TEB scenario during the day and night. The influence of the warmer surface in the spring case is to the higher altitudes (~ 1000 m). The temperature was significantly higher in the TEB scenario than in the NO-TEB scenario in the whole domain at night, which shows a strong nocturnal UHI. The temperature cross-section on June 6 showed a deep convective boundary layer, UHI in the urban scenario, as well as strong nocturnal UHI in the TEB scenario. In the summer case, the UHI's temperature was higher at higher altitudes, and the UHI did not disappear

at night in the TEB scenario, mainly over the city centre with a higher density of mid-high buildings;

- Virtual potential temperature profiles indicated strong stability of the boundary layer in the winter case, in the morning and at night, for the NO-TEB scenario, while the boundary layer after the sunrise for the TEB scenario was unstable;
- The winter case showed the simultaneous occurrence of low-level humidity inversion and temperature inversion at night. There was also humidity inversion in the summer case. A summer case was very humid and hot, which caused a deep humidity inversion for the TEB scenario. In the spring and late spring scenarios, the differences of the vertical profiles of specific humidity between NO-TEB and TEB scenarios yielded positive values, which means that the boundary layer for the TEB scenario is less humid than the NO-TEB scenario;
- The warmer surface and higher surface roughness in the TEB scenario caused a higher TKE in the winter case. In the spring, late spring, and summer cases, the TKE was generated by buoyant production. During the daytime, the buoyant production was the source of TKE in all three cases. The TEB scenario yielded higher TKE during the day due to higher air and surface temperature, which produced a convective boundary layer.

The second part of the analysis was performed to study the sensitivity of different meteorological parameters to the changes in urban surface properties by comparing the following scenarios:

1. City scenario using the TEB classification (TEB-CLC);
2. High-building-only scenario, in which the city is covered with high impervious buildings (TEB-HB);
3. Vegetation-only for which the city is replaced by the surrounding natural covers (TEB-VEG).

The results were as follows:

- The urban heat island (UHI) was studied for the three scenarios in four selected cases. There was a strong nocturnal urban heat island in the spring and late spring cases. The city covered with mid-high buildings yielded the highest ΔT_{max}. The specific humidity in these cases is also smaller in the TEB-HB and TEB-CLC scenarios than in the TEB-VEG scenario. Therefore, it can be concluded that the greatest UHI occurred for dry cases. The intense nocturnal UHI in the winter case results from a cold air advection, so the UHI could be amplified due to the high thermal inertia of the town and anthropogenic heat flux, which was much stronger for the TEB-HB with higher buildings. Passing fronts impacted the UHI in the summer case with large thermal differences in the daytime and negative difference at midday. The TEB-HB showed the highest UHI in the summer case as well;
- Results of the surface temperature in the three scenarios showed that the surface temperature in the TEB-HB scenario was the highest and for the TEB-VEG scenario was the lowest in all four cases. Dry surfaces and surfaces with the lower albedo, mostly in urban areas, have a higher surface temperature than natural land covers with higher evaporation and its cooling effect;
- The specific humidity in the warmer seasons (C2, C3, and C4) was higher in the TEB-VEG scenario than in the TEB-HB and TEB-CLC scenarios due to the weaker evaporation rate and higher convective mixing during the daytime in the city area. The maximum difference of specific humidity occurs during the day. There was an excess of moisture in the city at night in the winter case.

- Regardless of the clear sky in the spring and late spring cases and no precipitation in TEB-CLC and TEB-VEG scenarios, in the city, there was a small amount of rainfall in the TEB-HB scenario. Higher UHI intensity and lower albedo in the TEB-HB scenario compared to the TEB-VEG scenario formed an upward motion downwind of the city. Urban heating causes perturbations in the wind field, which leads to the horizontal convergence around the zone of upward motion downwind of the city and eventually produces urban-induced precipitation. The precipitation rate in the winter case was higher for the TEB-VEG scenario than for the TEB-HB and TEB-CLC scenarios;
- Mechanical and thermal turbulence produced by buildings on the city surface imposes higher turbulence in the urban boundary layer than the natural land cover. In the spring, late spring, and summer cases, the atmosphere is dynamically unstable because of convection and buoyancy that produce turbulence, so city scenarios yielded higher TKE than the natural cover. TEB-HB has a considerably higher TKE in all the cases.

The sensitivity analyses were completed with evaluation against meteorological data from six urban monitoring stations (Radzymińska, Jerozolimskie, Bielany, Puławska, Krakowska, and Jelonki) in Warsaw. The comparison of observed and modelled temperature shows that the temperature predicted with the TEB parameterisation was more accurate in terms of statistical error measures on January 29 and April 24 for all the stations. On January 29, the model underestimated the temperature for both scenarios. The underestimation in temperature at night in this case was due to the significantly lower cloud cover in the model than in the real situation. On April 24, adding the TEB parameterisation to the model improved the model performance, and there was a strong correlation. However, the NO-TEB scenario underestimated the temperature. On June 6, the TEB scenario had slightly better performance and higher correlation than the NO-TEB scenario. However, the difference between the two scenarios is very small, and the model overestimated the temperature. The model for both scenarios did not perform well at night. Therefore, it requires more detailed surface flux analysis. On July 23, the TEB parameterisation did not improve the model performance, and the NO-TEB scenario performed slightly better. This case also needs further analysis of the surface fluxes, especially the anthropogenic heat flux. In June and July, the anthropogenic heat flux is less critical. The radiative characteristics of urban surfaces used in the model should probably be revised for these two cases.

The statistical error measures were not performed for the wind speed because the measurements from the observational stations are not representative of the results obtained from the model.

The vertical profiles of temperature were compared with radiosoundings obtained from the Legionowo station. The comparison of the sounding profiles with the vertial profiles for NO-TEB and TEB models showed that TEB improved model performance in reproducing temperature, especially at the day time. The winter case could not be compared in the lower altitudes up to ~500 m due to the data gap from soundings.

5.2 Future work

The research undertaken for this thesis highlighted several topics on which further research would be beneficial.

1. Examination of surface fluxes and anthropogenic heat fluxes in detail to better understand the impacts of the anthropogenic sources on the changes of the meteorological parameters.
2. Vegetation can significantly impact and moderate the urban climate, specifically, the urban heat island. Different types of greenery and their location can influence the microclimate over cities. Studying properties of different vegetation types and their impact on the urban

climate can lead to the implementation of appropriate green elements in the city by urban planners and ultimately optimize the urban climate. A modelling study could be used for guiding urban planning.

3. Carry out sensitivity studies with the GEM-AQ model (the GEM model with air quality processes) to assess the impact of different land covers on air quality in Warsaw. The knowledge how different types of land cover can impact the air quality could lead to better air quality forecasts and the development of mitigation plans.

References

Arnfield, A.J. (2003), Two decades of urban climate research: a review of turbulence, exchanges of energy and water, and the urban heat island, *Int. J. Climatol.* **23**, 1, 1–26, DOI: 10.1002/joc.859.

Auer, A.H., Jr. (1978), Correlation of land use and cover with meteorological anomalies, *J. App. Meteorol. Clim.* **17**, 5, 636–643, DOI: 10.1175/1520-0450(1978)017<0636:COLUAC>2.0.CO;2.

Auer, A.H., Jr. (1981), Urban boundary layer. **In:** S.A. Changnon (ed.), *METROMEX: A Review and Summar*y, Meteorological Monographs, Vol. 18, American Meteorological Society, Boston, 41–62, DOI: 10.1007/978-1-935704-29-4_3.

Baklanov, A., U. Korsholm, A. Mahura, C. Petersen, and A. Gross (2008), ENVIRO¬HIRLAM: on-line coupled modelling of urban meteorology and air pollution, *Adv. Sci. Res.* **2**, 1, 41–46, DOI: 10.5194/asr-2-41-2008.

Barlow, J.F. (2014), Progress in observing and modelling the urban boundary layer, *Urban Clim.* **10**, 2, 216–240, DOI: 10.1016/j.uclim.2014.03.011.

Barry, R.G., and P.D. Blanken (2016), *Microclimate and Local Climate*, Cambridge University Press, Cambridge, DOI: 10.1017/CBO9781316535981.

Brunke, M.A., S.T. Stegall, and X. Zeng (2015), A climatology of tropospheric humidity inversions in five reanalyses, *Atmos. Res.* **153**, 165–187, DOI: 10.1016/j.atmosres.2014.08.005.

Chandler, T.J. (1976), Urban climatology and its relevance to urban design, Tech. Rep. No. 149, Geneva World Meteorological Organization.

Changnon, S.A. (1981), Midwestern cloud, sunshine and temperature trends since 1901: Possible evidence of jet contrail effects, *J. App. Meteorol. Clim.* **20**, 5, 496–508, DOI: 10.1175/1520-0450(1981)020<0496:MCSATT>2.0.CO;2.

Chen, F., H. Kusaka, M. Tewari, J.-W. Bao, and H. Hirakuchi (2004), Utilizing the coupled WRF/LSM/urban modeling system with detailed urban classification to simulate the urban heat island phenomena over the Greater Houston area. **In:** *Fifth Symp. Urban Environment*, Vol. 25, 9–11, American Meteorological Society, Vancouver, BC, Canada.

Confalonieri, U., B. Menne, R. Akhtar, K.L. Ebi, M. Hauengue, R.S. Kovats, B. Revich, and A. Woodward (2007), Human health. **In:** *Climate Change 2007: Impacts, Adaptation and Vulnerability. Contribution of Working Group II to the Fourth Assessment Report of the Intergovernmental Panel on Climate Change*, 391–431, Cambridge University Press, Cambridge.

Côté, J., S. Gravel, A. Méthot, A. Patoine, M. Roch, and A. Staniforth (1998), The operational CMC–MRB Global Environmental Multiscale (GEM) model. Part I: Design considerations and formulation, *Mon. Weather Rev.* **126**, 6, 1373–1395, DOI: 10.1175/1520-0493(1998)126<1373:TOCMGE>2.0.CO;2.

Daniel, M., A. Lemonsu, M. Déqué, S. Somot, A. Alias, and V. Masson (2019), Benefits of explicit urban parameterization in regional climate modeling to study climate and city interactions, *Clim. Dynam.* **52**, 5-6, 2745–2764, DOI: 10.1007/s00382-018-4289-x.

Darcy, H. (1857), *Recherches Experimentales Relatives au Mouvement de L'Eau deans les Tuyaux* (Experimental research relating to the movement of water in pipes), Impr. Impériale, Paris (in French).

Dirksen, M., R.J. Ronda, N.E. Theeuwes, and G.A. Pagani (2019), Sky view factor calculations and its application in urban heat island studies, *Urban Clim.* **30**, 100498, DOI: 10.1016/j.uclim.2019.100498..

Ellefsen, R. (1991), Mapping and measuring buildings in the canopy boundary layer in ten U.S. cities, *Energ. Buildings* **16**, 3-4, 1025–1049, DOI: 10.1016/0378-7788(91)90097-M..

Emeis, S., K. Baumann-Stanzer, M. Piringer, M. Kallistratova, R. Kouznetsov, and V. Yushkov (2007), Wind and turbulence in the urban boundary layer-analysis from acoustic remote sensing data and fit to analytical relations, *Meteorol. Z.* **16**, 4, 393–406, DOI: 10.1127/0941-2948/2007/0217.

Erell, E. (2008), The application of urban climate research in the design of cities, *Adv. Building Energ. Res.* **2**, 1, 95–121, DOI: 10.3763/aber.2008.0204.

Erell, E., D. Pearlmutter, and T. Williamson (2012), *Urban Microclimate: Designing the Spaces between Buildings*, Routledge, Abingdon, DOI: 10.4324/9781849775397.

Fortuniak, K., K. Kłysik, and J. Wibig (2006), Urban–rural contrasts of meteorological parameters in Łódź, *Theor. Appl. Climatol.* **84**, 1, 91–101, DOI: 10.1007/s00704-005-0147-y.

Garuma, G.F. (2018), Review of urban surface parameterizations for numerical climate models, *Urban Clim.* **24**, 830–851, DOI: 10.1016/j.uclim.2017.10.006.

Gauthier, P., C. Charette, L. Fillion, P. Koclas, and S. Laroche (1999), Implementation of a 3D variational data assimilation system at the Canadian Meteorological Centre. Part I: The global analysis, *Atmos. Ocean* **37**, 2, 103–156, DOI: 10.1080/07055900.1999.9649623.

Gauthier, P., M. Tanguay, S. Laroche, S. Pellerin, and J. Morneau (2007), Extension of 3DVAR to 4DVAR: Implementation of 4DVAR at the Meteorological Service of Canada, *Mon. Weather Rev.* **135**, 6, 2339–2354, DOI: 10.1175/MWR3394.1.

Gawuc, L., L. Łobocki, and J. Strużewska (2022), Application of the profile method for the estimation of urban sensible heat flux using roadside weather monitoring data and satellite imagery, *Urban Climate* **42**, 101098, DOI: 10.1016/j.uclim.2022.101098.

Georgiadis, T. (2017), Urban climate and risk. **In:** *Oxford Handbook Topics in Physical Sciences*, Oxford University Press, DOI: 10.1093/oxfordhb/9780190699420.013.11.

Godowitch, J.M., J.K.S. Ching, and J.F. Clarke (1985), Evolution of the nocturnal inversion layer at an urban and nonurban location, *J. App. Meteorol. Clim.* **24**, 8, 791–804, DOI: 10.1175/1520-0450(1985)024<0791:EOTNIL>2.0.CO;2.

Grimmond, C.S.B., M. Blackett, M.J. Best, J. Barlow, J.-J. Baik, S.E. Belcher, S.I. Bohnenstengel, I. Calmet, F. Chen, A. Dandou, K. Fortuniak, M.L. Gouvea, R. Hamdi, M. Hendry, T. Kawai, Y. Kawamoto, H. Kondo, E.S. Krayenhoff, S.-H. Lee, T. Loridan, A. Martilli, V. Masson, S. Miao, K. Oleson, G. Pigeon, A. Porson, Y.-H. Ryu, F. Salamanca, L. Shashua-Bar, G.J. Steeneveld, M. Tombrou, J. Voogt, D. Young, and N. Zhang (2010), The international urban energy balance models comparison project: first results from phase 1, *J. App. Meteorol. Clim.* **49**, 6, 1268–1292, DOI: 10.1175/2010JAMC2354.1.

Grimmond, S. (2007), Urbanization and global environmental change: local effects of urban warming, *Geogr. J.* **173**, 1, 83–88, DOI: 10.1111/j.1475-4959.2007.232_3.x.

Hagen, G.H.L. (1854), *Über den Einfluss der Temperatur auf die Bewegung des Wassers in Röhren*, Druckerei der Königl. Akademie der Wissenschaften.

Harlan, S.L., and D.M. Ruddell (2011), Climate change and health in cities: impacts of heat and air pollution and potential co-benefits from mitigation and adaptation, *Curr. Opin. Env. Sust.* **3**, 3, 126–134, DOI: 10.1016/j.cosust.2011.01.001.

Hartmann, D.L. (2015), *Global Physical Climatology*, International Geophysics Ser., Vol. 103. Elsevier, Amsterdam.

Hidalgo, J., V. Masson, A. Baklanov, G. Pigeon, and L. Gimeno (2008), Advances in urban climate modeling, *Trends and Directions in Climate Research: Ann. N. Y. Acad. Sci.* **1146**, 1, 354–374, DOI: 10.1196/annals.1446.015.

Holt, T., and J. Pullen (2007), Urban canopy modeling of the New York City metropolitan area: A comparison and validation of single- and multilayer parameterizations, *Mon. Weather Rev.* **135**, 5, 1906–1930, DOI: 10.1175/MWR3372.1.

Hościło, A., and M. Tomaszewska (2014), CORINE Land Cover 2012 – 4th CLC inventory completed in Poland, *Geoinform. Iss.* **6**, 1(6), 49–58, DOI: 10.34867/gi.2014.4.

Howard, L. (1833), *The Climate of London, Deduced from Meteorological Observations Made in the Metropolis, and at Various Places Around It*, Vol. 3, Harvey and Darton, J. and A. Arch, Longman, Hatchard, S. Highley, R. Hunter.

Jandaghian, Z., and U. Berardi (2020), Comparing urban canopy models for microclimate simulations in Weather Research and Forecasting Models, *Sustain. Cities Soc.* **55**, 102025, DOI: 10.1016/j.scs.2020.102025.

Jandaghian, Z., A.G. Touchaei, and H. Akbari (2018), Sensitivity analysis of physical parameterizations in WRF for urban climate simulations and heat island mitigation in Montreal, *Urban Clim.* **24**, 577–599, DOI: 10.1016/j.uclim.2017.10.004.

Jiang, X., C. Wiedinmyer, F. Chen, Z.-L. Yang, and J.C.-F. Lo (2008), Predicted impacts of climate and land use change on surface ozone in the Houston, Texas, area, *J. Geophys. Res. – Atmos.* **113**, D20, DOI: 10.1029/2008JD009820.

Jihad, A.S., and M. Tahiri (2016), Analysis of canyon aspect ratio impact on urban heat island and buildings energy consumption in Fez climatic zone, Morocco, *ARPN J. Eng. Appl. Sci*. **11**, 5, 3059–3073.

Johnson, G.T., and I.D. Watson (1984), The determination of view-factors in urban canyons, *J. App. Meteorol. Clim.* **23**, 2, 329–335, DOI: 10.1175/1520-0450(1984)023<0329:TDOVFI>2.0.CO;2.

Kim, J.-P. (2009), Land-use Planning and the Urban Heat Island Effect, Ph.D. Thesis, The Ohio State University.

Kim, Y.-H., and J.-J. Baik (2002), Maximum urban heat island intensity in Seoul, *J. Appl. Meteorol. Clim.* **41**, 6, 651–659, DOI: 10.1175/1520-0450(2002)041<0651:MUHIII>2.0.CO;2.

Kłysik, K., and K. Fortuniak (1999), Temporal and spatial characteristics of the urban heat island of Łódź, Poland, *Atmos. Environ.* **33**, 24-25, 3885–3895, DOI: 10.1016/S1352-2310(99)00131-4.

Kusaka, H., and F. Kimura (2004), Coupling a single-layer urban canopy model with a simple atmospheric model: Impact on urban heat island simulation for an idealized case, *J. Meteorol Soc. Japan Ser. II*, **82**, 1, 67–80, DOI: 0.2151/jmsj.82.67.

Kusaka, H., H. Kondo, Y. Kikegawa, and F. Kimura (2001), A simple single-layer urban canopy model for atmospheric models: Comparison with multi-layer and slab models, *Bound-Lay. Meteorol.* **101**, 3, 329–358, DOI: 10.1023/A:1019207923078.

Laroche, S., P. Gauthier, M. Tanguay, S. Pellerin, and J. Morneau (2007), Impact of the different components of 4DVAR on the global forecast system of the Meteorological Service of Canada, *Mon. Weather Rev.* **135**, 6, 2355–2364, DOI: 10.1175/MWR3408.1.

Lee, S.-H., and S.-U. Park (2008), A vegetated urban canopy model for meteorological and environmental modelling, *Bound-Lay. Meteorol.* **126**, 1, 73–102, DOI: 10.1007/s10546-007-9221-6.

Lemonsu, A., S. Belair, and J. Mailhot (2009), The new Canadian urban modelling system: Evaluation for two cases from the Joint Urban 2003 Oklahoma City experiment, *Bound-Lay. Meteorol.* **133**, 1, 47–70, DOI: 10.1007/s10546-009-9414-2.

Lemonsu, A., S. Bélair, J. Mailhot, and S. Leroyer (2010), Evaluation of the Town Energy Balance model in cold and snowy conditions during the Montreal Urban Snow Experiment 2005, *J. App. Meteorol. Clim.* **49**, 3, 346–362, DOI: 10.1175/2009JAMC2131.1.

Li, J., X. Zheng, C. Zhang, and Y. Chen (2018), Impact of land-use and land-cover change on meteorology in the Beijing–Tianjin–Hebei Region from 1990 to 2010, *Sustainability* **10**, 1, 176, DOI: 10.3390/su10010176.

Lin, C.-Y., F. Chen, J.C. Huang, W.-C. Chen, Y.-A. Liou, W.-N. Chen, and S.-C. Liu (2008), Urban heat island effect and its impact on boundary layer development and land–sea circulation over northern Taiwan, *Atmos. Environ.* **42**, 22, 5635–5649, DOI: 10.1016/j.atmosenv.2008.03.015.

Liu, J., and D. Niyogi (2019), Meta-analysis of urbanization impact on rainfall modification, *Sci. Rep.* **9**, 1, 7301, DOI: 10.1038/s41598-019-42494-2.

Loveland, T.R., B.C. Reed, J.F. Brown, D.O. Ohlen, Z. Zhu, L. Yang, and J.W. Merchant (2000), Development of a global land cover characteristics database and IGBP DISCover from 1 km AVHRR data, *Int. J. Remote Sens*. **21**, 6-7, 1303–1330, DOI: 10.1080/014311600210191.

Majewska, A., M. Denis, and W. Krupowicz (2020), Urbanization chaos of suburban small cities in Poland: 'Tetris development', *Land* **9**, 11, 461, DOI: 10.3390/land9110461.

Martilli, A., A. Clappier, and M.W. Rotach (2002), An urban surface exchange parameterisation for mesoscale models, *Bound-Lay. Meteorol.* **104**, 2, 261–304, DOI: 10.1023/A:1016099921195.

Masson, V. (2000), A physically-based scheme for the urban energy budget in atmospheric models, *Bound-Lay. Meteorol.* **94**, 3, 357–397, DOI: 10.1023/A:1002463829265.

Masson, V., C.S.B. Grimmond, and T.R. Oke (2002), Evaluation of the town energy balance (TEB) scheme with direct measurements from dry districts in two cities, *J. Appl. Meteorol. Clim.* **41**, 10, 1011–1026, DOI: 10.1175/1520-0450(2002)041<1011:EOTTEB>2.0.CO;2.

Miao, S., and F. Chen (2008), Formation of horizontal convective rolls in urban areas, *Atmos. Res.* **89**, 3, 298–304, DOI: 10.1016/j.atmosres.2008.02.013.

Miao, S., F. Chen, M.A. LeMone, M. Tewari, Q. Li, and Y. Wang (2009), An observational and modeling study of characteristics of urban heat island and boundary layer structures in Beijing, *J. App. Meteorol. Clim.* **48**, 3, 484–501, DOI: 10.1175/2008JAMC1909.1.

Mills, G. (1997), An urban canopy-layer climate model, *Theor. Appl. Climatol*. **57**, 3, 229–244, DOI: 10.1007/BF00863615.

Mills, G. (2008), Luke Howard and 'The Climate of London', *Weather* **63**, 6, 153–157, DOI: 10.1002/wea.195.

Mills, G. (2014), Urban climatology: History, status and prospects, *Urban Clim.* **10**, 3, 479–489, DOI: 10.1016/j.uclim.2014.06.004.

Niyogi, D., P. Pyle, M. Lei, S.P. Arya, C.M. Kishtawal, M. Shepherd, F. Chen, and B. Wolfe (2011), Urban modification of thunderstorms: An observational storm climatology and model case study for the Indianapolis urban region, *J. App. Meteorol. Clim.* **50**, 5, 1129–1144, DOI: 10.1175/2010JAMC1836.1.

Nygård, T., T. Valkonen, and T. Vihma (2013), Antarctic low-tropospheric humidity inversions: 10-yr climatology, *J. Climate* **26**, 14, 5205–5219, DOI: 10.1175/JCLI-D-12-00446.1.

Oke, T.R. (1973), City size and the urban heat island, *Atmos. Environ. (1967)* **7**, 8, 769–779, DOI: 10.1016/0004-6981(73)90140-6.

Oke, T.R. (1976), The distinction between canopy and boundary-layer urban heat islands, *Atmosphere* **14**, 4, 268–277, DOI: 10.1080/00046973.1976.9648422.

Oke, T.R. (1982), The energetic basis of the urban heat island, *Q. J. Roy. Meteor. Soc*. **108**, 455, 1–24, DOI: 10.1002/qj.49710845502.

Oke, T.R. (1988), The urban energy balance, *Prog. Phys. Geogr*. **12**, 4, 471–508, DOI: 10.1177/030913338801200401.

Oke, T.R. (1997), Urban environments. **In:** W.G. Bailey, T.R. Oke, and W.R. Rouse (eds.), *The Surface Climates of Canada*, McGill-Queen's University Press, Montreal, 303–327.

Oke, T.R. (2002), *Boundary Layer Climates*, Routledge, Abingdon, DOI: 10.4324/9780203407219.

Oke, T. (2004), Urban observations, World Meteorological Organization, IOM Report, 81.

Oke, T.R. (2009), Chandler, T.J. 1965: The climate of London. London: Hutchinson, 292 pp., *Prog. Phys. Geog*. **33**, 3, 437–442, DOI: 10.1177/0309133309339794.

Oke, T.R., and H.A. Cleugh (1987), Urban heat storage derived as energy balance residuals, *Bound-Lay. Meteorol.* **39**, 3, 233–245, DOI: 10.1007/BF00116120.

Oke, T.R., G. Mills, A. Christen, and J.A. Voogt (2017), *Urban Climates*, Cambridge University Press, DOI: 10.1017/9781139016476.

Oleson, K.W., G.B. Bonan, J. Feddema, and M. Vertenstein (2008), An urban parameterization for a global climate model. Part II: Sensitivity to input parameters and the simulated urban heat island in offline simulations, *J. App. Meteorol. Clim.* **47**, 4, 1061–1076, DOI: 10.1175/2007JAMC1598.1.

Palarz, A., and D. Celiński-Mysław (2020), Low-tropospheric humidity inversions over Europe: spatio-temporal variability and relations to temperature inversions' occurrence, *Theor. Appl. Climatol*. **141**, 967–978, DOI: 10.1007/s00704-020-03250-z.

Rimal, B., L. Zhang, H. Keshtkar, B.N. Haack, S. Rijal, and P. Zhang (2018), Land use/land cover dynamics and modeling of urban land expansion by the integration of Cellular Automata and Markov Chain, *ISPRS Int. J. Geo-Inf.* **7**, 4, 154, DOI: 10.3390/ijgi7040154.

Rontu, L., E. Gleeson, D. Martin Perez, K. Pagh Nielsen, and V. Toll (2020), Sensitivity of radiative fluxes to aerosols in the ALADIN-HIRLAM numerical weather prediction system, *Atmosphere* **11**, 2, 205, DOI: 10.3390/atmos11020205.

Roth, M. (2000), Review of atmospheric turbulence over cities, *Q. J. Roy. Meteor. Soc*. **126**, 564, 941–990, DOI: 10.1002/qj.49712656409.

Salamanca, F., A. Martilli, M. Tewari, and F. Chen (2011), A study of the urban boundary layer using different urban parameterizations and high-resolution urban canopy parameters with WRF, *J. App. Meteorol. Clim.* **50**, 5, 1107–1128, DOI: 10.1175/2010JAMC2538.1.

Salim, M.H., S. Schubert, J. Resler, P. Krč, B. Maronga, F. Kanani-Sühring, M. Sühring, and C. Schneider (2022), Importance of radiative transfer processes in urban climate models: a study based on the PALM 6.0 model system, *Geosci. Model Dev.* **15**, 145–171, DOI: 10.5194/gmd-15-145-2022.

Sharma, A., H.J.S. Fernando, J. Hellmann, and F. Chen (2014), Sensitivity of WRF model to urban parameterizations, with applications to Chicago metropolitan urban heat island. **In:** *Conf. Proc. Fluids Engineering Division Summer Meeting, 3–7 August, 2014, Chicago, IL, USA*, V01DT28A002, American Society of Mechanical Engineers, DOI: 10.1115/FEDSM2014-21292.

Sharma, A., H.J.S. Fernando, A.F. Hamlet, J.J. Hellmann, M. Barlage, and F. Chen (2017), Urban meteorological modeling using WRF: a sensitivity study, *Int. J. Climatol.* **37**, 4, 1885–1900, DOI: 10.1002/joc.4819.

Shem, W., and M. Shepherd (2009), On the impact of urbanization on summertime thunderstorms in Atlanta: Two numerical model case studies, *Atmos. Res.* **92**, 2, 172–189, DOI: 10.1016/j.atmosres.2008.09.013.

Stala-Szlugaj, K. (2016), Trends in the consumption of hard coal in Polish households compared to EU households, *Gospod. Surowcami Min*. **32**, 3, 5–22, DOI: 10.1515/gospo-2016-0024.

Stewart, I.D., and T.R. Oke (2012), Local climate zones for urban temperature studies, *Bull. Am. Meteorol. Soc.* **93**, 12, 1879–1900, DOI: 10.1175/BAMS-D-11-00019.1.

Stull, R.B. (1988), *An Introduction to Boundary Layer Meteorology*, Atmospheric and Oceanographic Sciences Ser., Vol. 13, Springer, Dordrecht, DOI: 10.1007/978-94-009-3027-8.

Szymańska, D., and A. Matczak (2002), Urbanization in Poland: tendencies and transformation, *Eur. Urban Reg. Stud*. **9**, 1, 39–46, DOI: 10.1177/096977640200900104.

Taha, H., and R. Bornstein (1999), Urbanization of meteorological models and implications on simulated heat islands and air quality. **In:** *International Congress of Biometeorology and International Conference on Urban Climatology (ICB-ICUC), 8–12 November 1999, Sydney, Australia*.

Tewari, M., H. Kusaka, F. Chen, W.J. Coirier, S. Kim, A.A. Wyszogrodzki, and T.T. Warner (2010), Impact of coupling a microscale computational fluid dynamics model with a mesoscale model on urban scale contaminant transport and dispersion, *Atmos. Res.* **96**, 4, 656–664, DOI: 10.1016/j.atmosres.2010.01.006.

UN (2018), World urbanization prospects, United Nations Department of Economic and Social Affairs, New York.

Wang, X., F. Chen, Z. Wu, M. Zhang, M. Tewari, A. Guenther, and C. Wiedinmyer (2009), Impacts of weather conditions modified by urban expansion on surface ozone: Comparison between the Pearl River Delta and Yangtze River Delta regions, *Adv. Atmos. Sci*. **26**, 5, 962–972, DOI: 10.1007/s00376-009-8001-2.

Wang, Z. (2011), Surface exchange of energy and water budgets in urban canopies, Ph.D. Thesis, Princeton University, Princeton.

Wei, R., D. Song, N.H. Wong, and M. Martin (2016), Impact of urban morphology parameters on microclimate, *Procedia Eng*. **169**, 142–149, DOI: 10.1016/j.proeng.2016.10.017.

Wypych, A., and B. Bochenek (2018), Vertical structure of moisture content over Europe, *Adv. Meteorol*. **2018**, 3940503, DOI: 10.1155/2018/3940503.

Yang, L., F. Qian, D.-X. Song, and K.-J. Zheng (2016), Research on urban heat-island effect, *Procedia Eng*. **169**, 11–18, DOI: 10.1016/j.proeng.2016.10.002.

Zhao, W., N. Zhang, J. Sun, and J. Zou (2014), Evaluation and parameter-sensitivity study of a single-layer urban canopy model (SLUCM) with measurements in Nanjing, China, *J. Hydrometeorol*. **15**, 3, 1078–1090, DOI: 10.1175/JHM-D-13-0129.1.

Received 13 January 2023
Received in revised form 6 April 2023
Accepted 10 May 2023

"Publications of the Institute of Geophysics, Polish Academy of Sciences: Geophysical Data Bases, Processing and Instrumentation" appears in the following series:

A – Physics of the Earth's Interior

B – Seismology

C – Geomagnetism

D – Physics of the Atmosphere

E – Hydrology (formerly Water Resources)

P – Polar Research

M – Miscellanea

Every volume has two numbers: the first one is the consecutive number of the journal and the second one (in brackets) is the current number in the series.